TAMPEREEN TEKNILLINEN YLIOPISTO
TAMPERE UNIVERSITY OF TECHNOLOGY

Ville Räisänen

Air Gap Fields in Electrical Machines: Harmonics and Modeling of Movement

Julkaisu 1281 • Publication 1281

Tampere 2015

Tampereen teknillinen yliopisto. Julkaisu 1281
Tampere University of Technology. Publication 1281

Ville Räisänen

Air Gap Fields in Electrical Machines: Harmonics and Modeling of Movement

Thesis for the degree of Doctor of Science in Technology to be presented with due permission for public examination and criticism in Sähkötalo Building, Auditorium S2, at Tampere University of Technology, on the 13th of February 2015, at 12 noon.

Tampereen teknillinen yliopisto - Tampere University of Technology
Tampere 2015

ISBN 978-952-15-3455-3 (printed)
ISBN 978-952-15-3460-7 (PDF)
ISSN 1459-2045

Contents

Abstract

The aim of this thesis is to develop mathematical tools for the efficient electromagnetic analysis of electromechanical devices. In the analysis of rotating electrical machines, the air gap fields play an important role. It is particularly useful to write the magnetic flux density in the air gap as a Fourier series expansion with respect to mechanical angle and/or time. Different terms in the series expansions are then called space and time harmonics and almost all relevant phenomena can be understood from the behaviour of the harmonics.

The main topic of this thesis is the application of spectral Dirichlet-to-Neumann mappings to model rotating electrical machines in terms of air gap harmonics. A spectral Dirichlet-to-Neumann mapping for a rotor or stator subproblem in a time or frequency domain boundary value problem (BVP) completely characterizes the electromagnetic behaviour of the subproblem from the viewpoint of the remaining problem and can be used to replace the subproblem with an implicit Neumann boundary condition. This allows the developement of new efficient numerical and analytical methods for analysis of electrical machines. We discuss several analytical and numerical methods, where reformulation of one or both subproblems with Dirichlet-to-Neumann maps is used to speed up the solution or to obtain more accurate solutions. Moreover, properties of the spectral Dirichlet-to-Neumann maps yield information, which can be used to predict and understand the air gap field harmonics.

The second topic of the thesis is the application of Riemannian geometry to construct BVPs for electromechanical devices in coordinate systems fixed to the moving bodies. Then, change of distances of the material points corresponds to change in the coordinate expression of the metric tensor in the air gap. In FE implementations, this allows modeling of movement without changes to the finite element mesh. We discuss the application of the approach to linear and rotating movement.

Preface

The research work discussed in this thesis was carried out in the Electromagnetics group at the Department of Electrical Engineering between July 2010 and September 2014.

I am grateful to Prof. Lauri Kettunen, Lasse Söderlund and Maija-Liisa Paasonen for organizing an environment, where I have been remarkably free to develop my ideas with very few distractions of any kind.

I would like to especially thank Dr. Saku Suuriniemi and Prof. Stefan Kurz for significant collaboration in my research work. There were several situations in my research, where I was ready to discard an idea, but you helped me to find the source of technical difficulties and encouraged me to develop the ideas further. I want to thank Lauri Kettunen also for very honest and insightful remarks about scientific writing and exact use of language.

Of course, my colleagues at the Electromagnetics group have been essential for a pleasant work environment. I would like to especially thank Veikko Puumala and Dr. Matti Pellikka for interesting discussions.

I'm also grateful to my family and friends for emotional support. Finally, I would like to thank my beloved Dr. Mika Rantanen for unconditional support, company and keeping me sane.

List of publications

This thesis consists of the following four publications:

P1: V. Räisänen, S. Kurz, S. Suuriniemi, T. Tarhasaari, L. Kettunen, "How can we deal with moving objects on a fixed mesh?", *Journal of Computational and Applied Mathematics*, vol. 246, pp.260-268, Jul. 2013.

P2: V. Räisänen, S.Suuriniemi, S. Kurz, L. Kettunen, "Rapid Computation of Harmonic Eddy-Current Losses in High-Speed Solid-Rotor Induction Machines" *IEEE Transactions on Energy Conversion*, vol. 28, no. 3, pp. 782-790, Sep. 2013.

P3: L. Kettunen, T. Tarhasaari, S. Kurz, V. Räisänen, A. Stenvall, S. Suuriniemi, "Modelling Rotation in Electrical Machines", *IEEE Transactions on Magnetics*, vol. 50, no. 4, pp. 1-10, Apr. 2014.

P4: V. Räisänen, S.Suuriniemi, S. Kurz, L. Kettunen, "Subdomain Reduction by Dirichlet-to-Neumann Mappings in Time-Domain Electrical Machine Modeling", *IEEE Transactions on Energy Conversion*, Accepted for Publication.

List of symbols

To avoid clutter, this list doesn't contain the symbols related to FE matrices, DoFs and their partitions used in subsections 3.3.2 and 5.3.4. Also symbols introduced in the section 3.5 discussing an example of an analytical solution are not included. The excluded symbols are only used in their respective sections.

Chapters 3-4

A_r, A_s	The magnetic stream function in the stator and rotor subdomains, respectively in their own coordinate systems.
A_i^k	Cross-sectional surface area of the slot i of the subproblem k.
A_{ik}^l	Solution of the BVP (3.20) – (3.22) with a unit current in the independent current l of the subproblem k.
$\widetilde{A}_{dk}^{\nu}$	Solution of the BVP (3.23) – (3.25) with the boundary condition $\widetilde{A}_{dk}^{\nu}\vert_{\Gamma_{sr}} = e^{-j\nu\theta_k}$
$\boldsymbol{B}, B_n, B_r,$ B_t	The magnetic flux density vector and its normal, radial and tangential components, respectively.
$[B^k]$	Matrix of the spectral Dirichlet-to-Neumann mapping for the subproblem k relating the Dirichlet data to the Neumann data in the absense of winding currents.
$[\mathcal{B}^k]$	Matrix of the frequency-domain spectral Dirichlet-to-Neumann mapping for the subproblem k relating the Dirichlet data to the Neumann data in the absense of winding currents.
$[\mathcal{B}^k_{\eta'_m\nu'_n}]$	The block of the matrix $[\mathcal{B}^k]$, which couples the time-harmonic ν'_n in the Dirichlet data to the time-harmonic η'_m in the Neumann data.
C^k	The circuit matrix relating the slots to the independent currents.
D_ν^k, N_η^k	The harmonic coefficients of the space harmonics ν and η in the Dirichlet and Neumann data of the subproblem k, respectively.
$\mathcal{D}_{\nu'\nu}, \mathcal{N}_{\eta'\eta}$	The harmonic coefficients of the harmonics (ν', ν) and (η', η) in the Dirichlet and Neumann data, respectively.
$\boldsymbol{E}, E_z$	The electric field vector and its axial component.
$\boldsymbol{F}$	The total net force per unit length on the rotor.
$[F^k]$	Matrix of the spectral Dirichlet-to-Neumann mapping for the subproblem k relating the independent currents to the Neumann data with zero Dirichlet data.

$[\mathcal{F}^k]$	Matrix of the frequency-domain spectral Dirichlet-to-Neumann mapping for the subproblem k relating the independent currents to the Neumann data with zero Dirichlet data.
$[\mathcal{F}^k_{\eta'_m\nu'_n}]$	The block of the matrix $[\mathcal{F}^k]$, which couples the time-harmonic ν'_n in the independent currents to the time-harmonic η'_m in the Neumann data.
$\boldsymbol{H}, H_n$	The magnetic field strength vector.
I^k_l	Total current corresponding to the independent current l in the subproblem k.
$I^k_{l\eta'}$	The time-harmonic coefficient for the time harmonic η' in I^k_l.
J^k_l	Current density corresponding to a unit current in the independent current l in the subproblem k.
J^k	Current density in the subproblem k.
L	Length of the active area of the motor.
m_k	Number of independent currents in the subproblem k.
O^k_γ	The harmonic coefficient of the space harmonic γ in the slot winding currents of the subproblem k.
$O^k_{\eta'\gamma}$	The harmonic coefficient of the harmonic (η', γ) in the slot winding currents of the subproblem k.
p	The number of pole pairs.
Q_k	The number of slots in the subproblem k.
$[Q^{Dk}]$, $[Q^{Ik}]$	Matrices relating the Dirichlet data and independent currents, respectively to the fluxes in the subproblem k.
r_δ	Radius of the circle Γ_{sr}.
$\mathcal{R}$	The equivalence relation for the space harmonics in the slot winding currents.
$[R_{\Delta\theta}]$	Rotation matrix for the rotation of $\Delta\theta$.
$[R^k]$	Resistance matrix for the independent currents of the subproblem k.
s	The rotor slip.
$s^p_{\nu'\nu}$	The generalized slip for the harmonic (ν', ν) for a machine with p pole pairs.
S^k_i	Cross-sectional surface of the slot i of the subproblem k.
$\boldsymbol{S}$	The Poynting vector.
t	Time.
T	The electromagetic torque on the rotor.
$\boldsymbol{u}$	The change of coordinates mapping from the stator to the rotor coordinate system.
V^k_l	Voltage corresponding to the independent current l of the subproblem k.
z^k_i	The number of slots in the slot i of the subproblem k.
γ	Space harmonic index in the slot winding currents.
$[\gamma]$	The equivalence class of γ with respect to the equivalence relation $\mathcal{R}$.
$[(\eta', \gamma)]$	The equivalence class of (η', γ) with respect to the equivalence relation $\mathcal{R}$.
Γ_{sr}	The rotor-stator interface at the center of the air gap.
Γ_{dr}, Γ_{ds}	Inner and outer boundaries of the problem domain.
$\Delta\theta$	The rotation angle of the rotor with respect to the stator.
$[\zeta^k]$	The matrix relating the harmonic coefficients of the space harmonics in the slot winding currents to the slot currents in the subproblem k.

θ_r, θ_s	Mechanical angle coordinate in the rotor and stator coordinate systems, respectively.
μ	The magnetic permeability.
ν, η	Space harmonic indices for harmonics in the Dirichlet and Neumann data.
$\Lambda_\theta, \lvert\Lambda_\theta\rvert$	The set of space harmonics included in the truncated model and their number.
$\Lambda_t, \lvert\Lambda_t\rvert$	The set of time harmonics included in the truncated model and their number.
$\nu_i = \eta_i$	The space harmonic number i in Λ_θ.
σ	The electric conductivity.
Φ_l^k	Flux corresponding to the independent current l of the subproblem k.
ω_f, ω_s	The fundamental and the synchronous time-frequencies, respectively.
$\Omega, \Omega_r, \Omega_s$	Problem domain and its rotor and stator subdomains, respectively.
$\langle f, g \rangle_\theta$	L_2 inner product of the functions f and g on $[0, 2\pi]$.
$\langle f, g \rangle_t$	L_2 inner product of the functions f and g on $[0, 2\pi/\omega_f]$.
x^*	Complex conjugate of x.

Chapter 5

a	The magnetic stream function defined in Ω.
a_α	The expression of a in the chart $(U_\alpha, \varphi_\alpha)$.
B, b	The magnetic flux 2- and 1-forms defined in E_3 and E_2, respectively.
d_E	The distance metric of the Euclidean space E^n.
$d\omega$	The exterior derivative of the differential form ω.
$dx^1_\alpha, ..., dx^n_\alpha$	The basis of the cotangent space induced by the chart $(U_\alpha, \varphi_\alpha)$.
$\mathcal{D}^n$	An n-dimensional vector space of displacements of a n-dimensional affine space.
$\boldsymbol{e}_1, ..., \boldsymbol{e}_n$	The standard basis for $\mathbb{R}^n$.
e, E	The electric field 0- and 1-forms in Ω and E^3, respectively.
$\mathcal{F}^k(M)$	The space of k-forms for the manifold M.
$\mathcal{F}^k_0(M)$	The space of k-forms for the manifold M with zero trace on the boundary of M.
E^n	An n-dimensional Euclidean space.
g_E	The Euclidean inner product for the displacement vectors of the space E^n
g_p	The metric tensor of E^n or Ω at the point p.
$[G^\alpha](p)$	The matrix for the metric tensor expressed in the chart $(U_\alpha, \varphi_\alpha)$ at the point p.
h, H	The magnetic field strength 1-forms in Ω and E^3, respectively.
$i_V B$	The contraction of the differential form B with the vector field V.
j, J	The current density 2-forms in Ω and E^3, respectively.
$[J]$	The Jacobian for a transition map between two charts.
$T_pE^n, T^*_pE^n$	The tangent and cotangent spaces of the manifold E^n at the point p.
U_α	The domain of the chart $(U_\alpha, \varphi_\alpha)$.
$\boldsymbol{v}^T_\alpha$	The time-derivative of $\boldsymbol{x}^\alpha_t$.
vol_n	The volume n-form.
$\boldsymbol{x}^\alpha_t$	The coordinate representation of X_t in terms of the chart $(U_\alpha, \varphi_\alpha)$.
X_t	One-parameter family of diffeomorphisms mapping points at some initial time to their positions at time t.
Γ	An inclusion map from E_2 to E_3.
δ_{ij}	The Kronecker delta function.
μ, μ_α	The magnetic permeability and its expression in the chart $(U_\alpha, \varphi_\alpha)$.
σ	The electric conductivity.
τ	The displacement mapping for the affine space (M^n, D^n, τ).
φ_α	The mapping of the chart $(U_\alpha, \varphi_\alpha)$.
$\Omega, \Omega_c, \Omega_s,$	The problem domain and its subregions with conductive materials and source currents, respectively.
$\partial^\alpha_1, ..., \partial^\alpha_n$	The basis of tangent space induced by the chart $(U_\alpha, \varphi_\alpha)$.
$\star, [\star^\alpha]$	Hodge star operator and its representation in the chart $(U_\alpha, \varphi_\alpha)$.
∇a_α	The gradient of a as expressed in the chart $(U_\alpha, \varphi_\alpha)$.

Chapter 1

Introduction

> A field of inquiry, no matter what it is, is established by some array of questions that we pose and as any researcher knows, asking the right questions is often the hardest part of the task. If you can do it, you may have won more than half the battle. The right questions are those that open up a program of inquiry that leads to insight and to problems that are worth understanding. .. Often the right questions are very simple. They invite us to become surprised about perfectly ordinary things - Things that we have taken for granted.
>
> — N.Chomsky, Asking the Right Questions
> Talk at University of North Carolina at Chapel Hill, 1992

It has been estimated that in 2006 approximately 82% of the electrical energy spent by the Finnish industry was used by electrical motors [1]. The energy used by electric motors can be expected to further increase, as conventional vehicles powered by internal combustion engines alone are becoming replaced by hybrid electric and fully battery-powered vehicles. Thus, even small improvements in the efficiency of electrical machines and drives may result in significant savings and reduction in emissions.

Technical innovations often arise from improved understanding of the underlying phenomena. This creates also a need for more accurate models of electromagnetic phenomenon in electrical machines. Accurate models also allow designers to quickly test new designs in arbitrary operating conditions without expensive and time-consuming prototyping.

During the last century, there has been significant developement in the analytical and numerical methods used in the analysis of electrical machines. The developement in numerical methods has coincided with the exponential growth in the computing power available from digital computers. The increasing computing power enables the use of more accurate models. Accuracy relies on the flexibility and efficiency of the used models and is crucial in order to obtain answers to practical questions.

However, there still are several types of machines and modeling scenarios, where application of standard numerical techniques is impractical due to long solution times. This results in the need for faster reliable numerical methods and necessitates a trade-off between generality and efficiency. This is the main motivation for the techniques

discussed in this thesis. The main objective of this study is to develop efficient and accurate methods for electromagnetic analysis of rotating electrical machines.

1.1 Air gap fields in electrical machines

Significant insight into the operation of rotating electrical machines is gained by the inspection of the air gap fields. In such analysis, it is especially useful to express the air gap fields as Fourier series expansions with respect to mechanical angle[1] and/or time. Different terms in the expansions are then called space and time harmonics and a wide array of different models for electrical machines can be constructed depending on which harmonic effects need to be modeled.

Simplest models used in elementary text books and two-axis theory typically build on models for rotating electrical machines in terms of the fundamental space harmonic alone [2, 3]. Even though approximate models for most types of rotating electrical machinery can be obtained this way, such models are usually unable to account for the harmonic effects due to slotting, finite permeability and saturation of the materials, multiple armature reaction, non-sinusoidal power supply and the non-sinusoidal distribution of the winding currents [4, 5].

Numerical solution methods based on the approximate solution of time-domain boundary value problems (BVP) with Finite Element Methods (FEM) have been widely adopted and provide a very general and accurate solution in most cases [6, 7]. However, such methods do not directly yield much useful information about the harmonic effects. There are also several situations, where accurate modeling of certain harmonic effects with standard time-domain FE methods requires extremely fine discretization, which is impractical for most design purposes due to required solution time. For example, stator slot harmonics in high-speed solid-rotor induction machines correspond to high-frequency currents on the rotor surface with very small skin depths (see publication 2).

On the other hand, analytical models and methods tend to be either limited to very simple geometries and material relations requiring often to make several crude approximations. Moreover, incorporation of effects such as multiple armature reaction and variation of air gap permeance into such models leads to extremely complex methods, which are difficult to use and understand [5].

This suggests a need for new methods taking advantage of the available computing power, which are relatively general, fast, straightforward and provide understanding of the behaviour of the various harmonic phenomena. However, in order to obtain faster methods, it is necessary to make a trade-off between generality and efficiency. By "fast" we mean in this context that the key figures of merit of a design are ascertained in no more than two hours. While a reasonable estimate for the torque of a high-speed induction machine is computable in two hours by standard FE methods, a tailored method is necessary for good eddy-current loss estimate.

[1] We do not use the concept of *electrical angle* in this work.

In particular, if mild saturation can be ignored in some parts of problem, the numerical method tailored for the problem should exploit linearity in the subproblem as much as possible. Moreover, a method tailored for rotating electrical machines should take advantage of the rotational symmetry in the material parameters of the rotor and stator subproblems with respect to rotations of single slots.

In chapters 2-4 and publication 4, we present a new technique to analyse electromagnetic fields in two-dimensional boundary value problems modeling rotating electrical machines. The domain of the BVP under consideration is first divided into rotor and stator subproblems at the interface Γ_{sr} at the center of the air gap. Then, subproblems with linear material relations and currents limited to the windings can be reduced into implicit boundary conditions on Γ_{sr}. The implicit boundary conditions are produced by so-called *Dirichlet-to-Neumann (D-to-N) mappings* for the magnetic stream function.

A D-to-N mapping for a subproblem at the interface Γ_{sr} is, intuitively speaking, a mapping, which maps the radial component to the tangential component of the flux density. Such a mapping completely characterizes the electromagnetic behaviour of the corresponding subproblem from the viewpoint of the remaining problem. For rotating electrical machines, D-to-N mappings in the time-domain can often be economically approximated to high accuracy in terms of truncated Fourier series expansions with respect to mechanical angle. We call such approximations *spectral Dirichlet-to-Neumann mappings* and they describe the corresponding subproblems in terms of space harmonics in the magnetic flux density. In frequency-domain, spectral D-to-N mappings characterize the behaviour of subproblems in terms of both space and time harmonics.

Once a D-to-N map for a subproblem has been constructed, solution of Finite Element (FE) equations for the subproblem in the time steps of subsequent analysis is no longer necessary and a very fast solution can often be achieved.

1.2 Coordinate systems, metric and motion

In formulation of BVPs arising from electrodynamics of electromechanical devices with rigid components, Cartesian or polar coordinates are almost always used. Typically, either a global Cartesian coordinate system is fixed to some ambient space or several Cartesian coordinate systems are fixed to the moving bodies and the corresponding subproblems are coupled on some interface in the air gap. Transformations between coordinate systems then reflect simple rotations and translations.

However, application of more complex coordinate system transformations is often beneficial in computational electromagnetism. Such transformations can be used, for example, when dealing with open boundaries [8, 9], different length scales [10, 8], cloaking [11], and exploitation of symmetries [12, 13]. The framework of Riemannian geometry forms a general framework for such transformations, allows coordinate-independent formulation of BVPs and provides tools in their representation in arbitrary coordinate systems [8, 14, 15]. The coordinate systems used for the problem can be chosen freely as long as the representation for the metric tensor of the manifold is transformed appropriately.

In chapter 5 and publications 1 and 3, we discuss how coordinate system transformations on a Euclidean space that is a Riemannian manifold can be used to model movement. A time-parametrized family of coordinate systems is used so that the coordinates of the material points of the moving objects are held fixed. Then, movement corresponds to a change in the representation of the metric tensor in the air gap. In FE implementations, these changes can be incorporated into the material relations in the air gap without any change to the mesh between time steps.

1.3 Author's contributions

Publications 2 and 4 are almost completely based on author's own work whereas author's contribution to publications 1 and 3 is more limited to the implementation and testing of the discussed methods. Thus, the bulk of this text is a discussion related to publications 2 and 4.

1.3.1 Publication 2

The publication presents a frequency-domain technique to model high-speed solid-rotor induction machines by analytical solutions for the rotor subproblem coupled to FE model of the stator. Since analytical solutions are used for the rotor subproblem and no time stepping is required, challenges with discretization are avoided and very fast and accurate solution is achieved. Compared to prior methods based on the use of analytical solutions, the main benefit of the proposed method is the ability to accurately predict the influence of the stator slots to the rotor fields. The paper also generalizes the multilayer method for analytical solutions presented in [16] to take the rotor curvature into account.

Analytical solution of the rotor fields in solid rotors in terms of invidual space harmonics forms also the basis of so-called Multi-Layer Transfer-Matrix (MLTM) methods[17]. However, since higher space harmonics in MLTM models are due to space harmonics in the current sheet expansion of the stator winding currents, stator models used in MLTM methods are unable to account for the influence of the stator slotting [18].

This technique should allow designers of high-speed solid-rotor induction machines rapid estimation of the eddy-current losses. As a practical example of a design application, the method was applied in the selection of the copper coating thickness for a solid rotor.

The technique was invented by the author. The author also implemented and tested all of the MATLAB code and GetDP scripts used for the simulations. Almost all of the text was written by the author, in collaboration with S. Suuriniemi.

1.3.2 Publication 4

The publication proposes the use of Fourier series representations of Dirichlet-to-Neumann mappings for the magnetic stream function to model the response of the rotor and stator

subproblems in time-domain BVPs for rotating electrical machines. When applied to time-domain BVPs, the method allows reformulation of the subproblems with implicit Neumann boundary conditions on the interface at the center of the air gap. This yields a significant reduction in the solution time compared to the full time-domain solution since the solution of the FE equations for the reformulated subproblem is no longer necessary every time step.

In the context of electrical machines, spectral Dirichlet-to-Neumann mappings have been previously applied to interpret an analytical model for the air gap [19].

The framework discussed in this publication should allow designers of electrical machines to use tailored models for more rapid testing of designs. The additional results discussed in chapter 3 should also help designers to develop intuition on the behaviour of harmonics and on their relation to different post-processing quantities.

The author invented and developed the application of spectral Dirichlet-to-Neumann mappings to reformulation of rotor and stator subproblems in BVPs for rotating electrical machines, implemented and tested all of the MATLAB code, GetDP scripts and Vector Fields Opera-2d models used for the simulations. Almost all of the text was written by the author, in collaboration with S. Suuriniemi.

1.3.3 Publication 1

The publication introduces a time-parametrized family of coordinate systems to keep the coordinates of material points fixed during motion. Then, movement corresponds to a change with time in the coordinate representation of the metric tensor. In FE implementations, the change in the metric tensor can be equivalently incorporated into the material relations.

In the context of electromechanics, a similar approach has been previously suggested in [20]. This publication provides designers of electromechanical devices an alternative method to model movement in BVPs arising from electromechanics. For a large class of such problems, this allows construction of efficient FE models without the need for remeshing between time steps.

The main contribution of the publication is the application to a realistic test case. The author implemented and tested all of the simulations with GetDP and MATLAB. The author also contributed originally to the portion of the paper on the mesh quality and condition numbers.

1.3.4 Publication 3

The publication combines the transformation techniques discussed in the publication 1 together with the lock step method to model rotation in electrical machines. This avoids some of the limitations of the lock step method by allowing decoupling of the time step size from the meshing of the air gap. Thus, this publication provides designers of rotating electrical machines an efficient alternative method to model rotation in FE models.

The author implemented and tested the test case simulations with GetDP and Vector Fields Opera-2d. The author also drew Figures 9-14 and contributed to the derivation of the post-processing formulas.

1.3.5 Frequency-domain spectral Dirichlet-to-Neumann mappings

Chapter 4 introduces a new framework for the frequency-domain analysis of rotating electrical machines based on frequency-domain spectral Dirichlet-to-Neumann mappings. Such mappings allow the construction of frequency-domain models, which correctly model the relevant harmonic effects. The method presented in publication 2 can be interpreted as a special case of this more general method.

The results discussed in chapter 4 should allow developement of more accurate frequency-domain models for rotating electrical machines. Moreover, the results related to generalized slip transformations and interpretation of sparsity patterns should help in the developement of intuition on the behaviour of harmonics.

We also show how the harmonic content of the air gap fields can be predicted from the sparsity patterns of the matrices for the D-to-N mappings. Since the sparsity patterns follow from the rotational symmetry in slotted geometries, this result applies to arbitrary rotationally symmetric slotted geometries and doesn't rely on such rather vague concepts as air gap permeance widely used in such analysis [4].

Chapter 2

Technical motivation

An *electromechanical system* typically involves coupling of an electric circuit to a mechanical system by an electromechanical converter, such as a rotary or a linear motor. Thus, models for electromechanical systems often couple at least three different models of subsystems together. Accuracy required for models of each subsystem depends on the application of the model. For example, designers of large automation processes with several motors do not usually require very accurate models for the electromagnetic behaviour of the electromechanical converters. In a similar way, designers of motor drives put most emphasis on the design of the electronic circuit controlling the motor, whereas the motor model is reduced to a few circuit parameters [21].

Accuracy of the electromagnetic model is, however, often critical to designers of electrical machines. Quite general and accurate model for classical electrodynamics is provided by Maxwell's equations together with material relations and the Lorentz law. However, in most applications in electrical engineering, it is impractical or impossible to predict the behaviour of the system by solving the exact fields from the full set of Maxwell's equations. Thus, different assumptions, approximations and approximation techniques are employed.

First, we limit our attention to *magnetoquasistatics*, where charge accumulation and corresponding displacement currents are ignored. This allows us to work with eddy-current problems in rotating and accelerating frames without significant complications in the model required [22, 23] but limits our ability to model capacitive effects and wave phenomena.

Next, we partition the space into region Ω containing the energy conversion subsystem under investigation and the surrounding space. Within Ω, the electromagnetic fields are described locally by partial differential equations (PDE) and material relations for the fields. Assumptions about the interaction between the fields in Ω and its exterior are reduced to some boundary conditions on the boundary $\partial\Omega$ of Ω. When time-independent, such a problem is called a *boundary value problem* (BVP). When time-dependent and started from some initial condition, such a problem is called *initial-boundary value problem* (IBVP). For brevity, we will call problems of both types boundary value problems.

2.1 Common solution strategies for boundary value problems

For any boundary value problem arising from electrical machines, there is a great variety of solution strategies, which can be roughly divided according to how they handle space and time.

The most useful solution for a BVP is an exact analytical one, which can be expressed in terms of small number of some known and easily handled mathematical functions. Such analytical solutions can be only found for problems or subproblems with simple geometries and with simple material relations. Often, the original boundary value problem has to be simplified in some way so that an exact analytical solution to the modified problem can be found [24].

In machine design, analytical solutions of simplified models are often useful for obtaining first design parameters and in design optimization. They can be also pedagogically useful in developing intuition since they often contain adjustable parameters.

During the recent decades, rapid increase in computer power has made the use of numerical field solution methods more practical. As the available computer power has increased, more accurate approximations can be made and some assumptions relaxed by the use of more accurate models.

The most general, accurate and widely applied solution methods are usually based on *Finite Element Methods* (FEM). The approximate geometry of the problem domain is partitioned into a *mesh* consisting of a finite number of geometrically simple *elements* such as lines, triangles or tetrahedra depending on the dimension of the problem domain. The solution field or fields for the BVP are approximated by a linear combination of locally supported basis functions associated to geometric primitives of the mesh such as nodes, edges and triangles. Application of the Galerkin procedure to a weak formulation corresponding to the BVP then yields a system of algebraic, differential or differential-algebraic equations [25].

With respect to time, the most general and accurate methods are usually based on time stepping. The solution is computed at a finite sequence of time steps by numerical integration. This usually amounts to solving a system of linear or non-linear equations every time step. With time-domain solvers, non-linear material relations without hysteresis can be accurately taken into account. Also transient effects, such as those present at the starting of the machine, can be modeled [6].

When time-domain FE methods are applied to BVPs arising from rotating electrical machines, the relative movement between the rotor and the stator requires special care. Traditionally, the mesh in the air gap is deformed gradually to conform to the movement of the rotor. Once the deformation exceeds some limit, the air gap is remeshed [26]. Changes in the mesh topology can lead to undesired *remeshing noise* in the post-processing quantities [27]. Special techniques have been developed, which avoid remeshing of the air gap [28].

In chapter 5 and publication 1, we present an approach based on Riemannian geometry, where movement is implemented by the use of a time-parametrized family of

coordinate systems fixed to the material bodies. In the corresponding FE implementation, the coordinates associated to the mesh nodes then remain fixed and the movement corresponds to change in the coordinate representation of the metric tensor. However, change in the representation of the metric tensor is equivalent to deformation of the mesh and significant changes can create the need to remesh the air gap. In publication 3, the approach is coupled with the lock-step method in order to model rotation in the air gap.

Unlike general-purpose FE methods, *tailored methods* aim to make as much use as possible of known properties of a more specific class of problems in order to achieve faster and/or more accurate solution. For example, this might involve the use of special basis functions [29], time stepping techniques or coupling of different types of models (see publication 2). In publications 2 and 4, we present tailored models for rotating electrical machines.

2.2 Space harmonics in electrical machines

To understand the types and varying degree of complexity of different models, consider the three two-dimensional cross-sectional models depicted in Figure 2.1. These models will be later placed into a more systematic context.

Let A be the magnetic stream function corresponding to the axial component of the magnetic vector potential. At the center Γ_{sr} of the air gap, we expand the magnetic stream function and its radial derivative as Fourier series expansions

$$A|_{\Gamma_{sr}}(\theta) = \sum_{\nu\in\mathbb{Z}} D_\nu e^{-j\nu\theta}, \tag{2.1}$$

$$\left.\frac{\partial A}{\partial r}\right|_{\Gamma_{sr}}(\theta) = \sum_{\eta\in\mathbb{Z}} N_\eta e^{-j\eta\theta}, \tag{2.2}$$

where θ is the mechanical angle and $D_\nu, N_\eta \in \mathbb{C}$ holds for each $\nu, \eta \in \mathbb{Z}$. The restrictions of the magnetic stream function and its radial derivative to Γ_{sr} are called the *Dirichlet and Neumann data*, respectively. The terms in the series expansion of the Dirichlet and Neumann data are called *space harmonics*. The coefficients D_ν and N_η the *Dirichlet and Neumann coefficients*, respectively.

Simplest models used with analytical methods typically ignore the space harmonics caused by the slotting of the rotor and stator and assume the winding currents to be sinusoidally distributed [2]. Such models are often closely related to the model depicted in Figure 2.1a. The air gap is assumed to be surrounded by infinitely permeable round rotor and stator regions with their sinusoidally distributed surface current sheets K_r and K_s. Due to continuous axisymmetry of the geometry and the surface current density, the resulting magnetic flux is also sinusoidally distributed. That is, the Fourier series expansions (2.1) – (2.2) contain only the non-zero space harmonics $\nu = \pm p$, where p is the number of pole pairs.

Crude understanding of many types of electrical machines can be obtained with such simple models, which are widely used in elementary textbooks [2, 3]. Non-sinusoidally

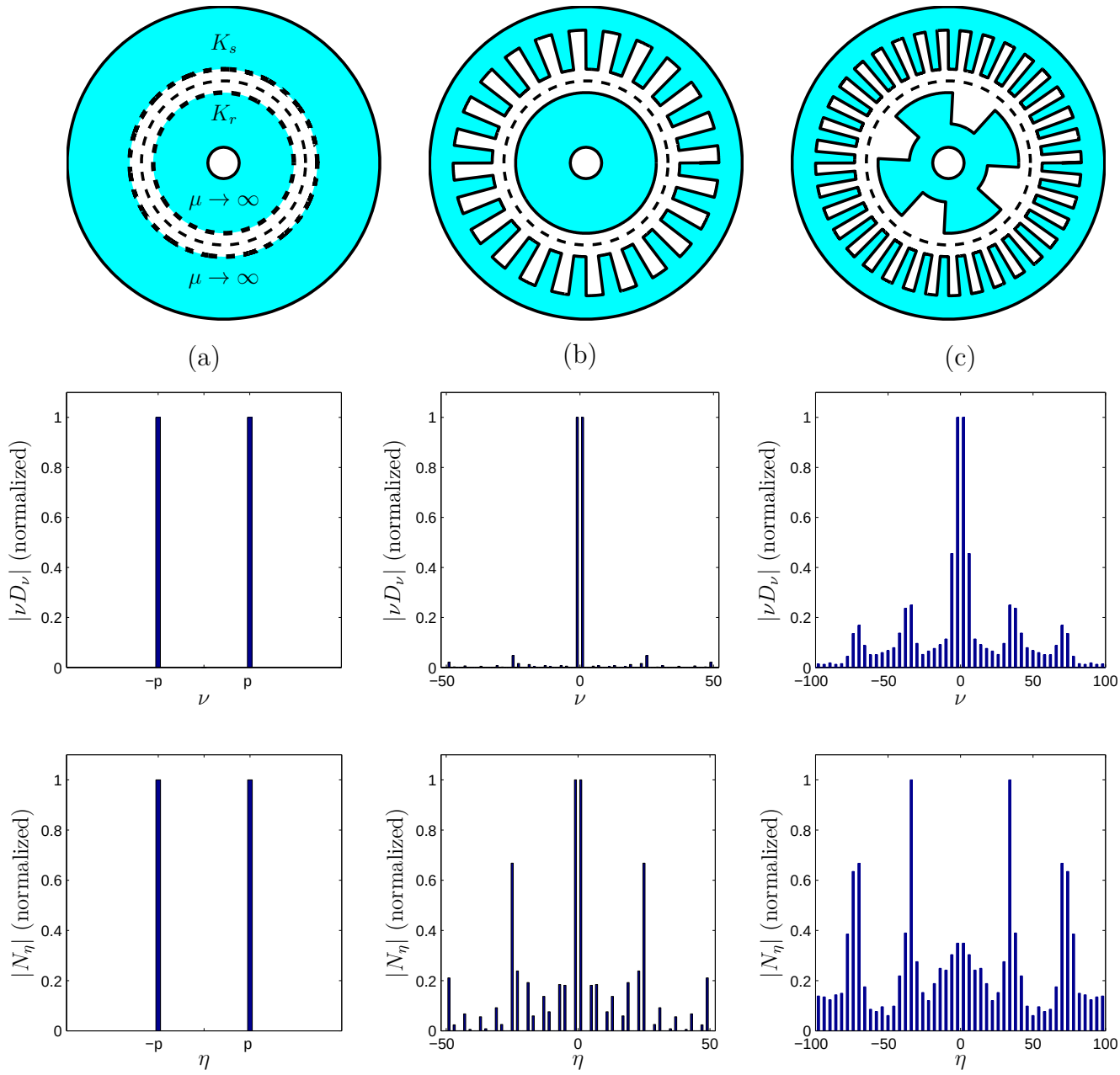

Figure 2.1: Three geometries and the Dirichlet and Neumann coefficients solved from BVPs with equal number of slots. The thickness of the air gap is exaggerated.

distributed winding currents can be modeled by expressing the current sheets as Fourier series with respect to the mechanical angle. Then the solution fields contain exactly the same non-zero space harmonics as the current sheets. For example, a balanced m-phase stator windings produce space harmonics of order $\nu = p(2mk \pm 1)$, where $k \in \mathbb{Z}$ [30].

Modeling the slotting effects significantly complicates the analysis of the machine. The slotting effects are often modeled and understood with so-called *permeance wave theory* [4], where the radial flux density and the magnetomotive force (MMF) over the air gap as function of spatial angle are related by a permeance function. The permeance functions are often obtained for simple slotted geometries with the help of conformal mappings [31].

Slotting of the rotor and/or stator introduces variation to the permeance of the air gap with respect to angle, leading to additional space harmonics in the air gap flux. In Figure 2.1*b*, the slotting of the stator with 24 slots influences the space harmonics $\nu = 24k \pm \nu_M$, where ν_M is a harmonic in the magnetomotive force over the air gap. Figure 2.1*c* shows a geometry, where both rotor and the stator are slotted. In such cases slotting effects are complex and the application of permeance wave theory involves further approximations [4]. However, in the suggested setting, the slotting of the rotor especially influences space harmonics $\nu = 4k \pm p$.

In chapter 3 and publication 4, we introduce a new approach for modeling harmonic effects in electrical machines. We will show that elliptic rotor and stator subproblems in time-domain BVPs for electrical machines can be efficiently replaced with implicit Neumann boundary conditions on the rotor-stator interface Γ_{sr}. The implicit boundary conditions for each replaced subproblem is determined by a *Dirichlet-to-Neumann (D-to-N) mapping* for the magnetic stream function. We call the subproblems replaced with spectral D-to-N mappings *reformulated subproblems*.

Dirichlet-to-Neumann mapping for a scalar field on a boundary or an interface is a map, which maps a scalar field to its normal derivative. The application of D-to-N mappings to BVPs arising from electrical engineering is not a new idea.Implicit Neumann boundary conditions determined by D-to-N mappings are often used for replacing infinite subdomains [32]. Dirichlet-to-Neumann mappings are also related to so-called Steklov-Poincaré operators, which have been widely used in the analysis of domain decomposition algorithms for the iterative numerical solution of boundary-value problems.[33]

In FE models for electrical machines, the relative movement between the rotor and the stator subproblems can be taken into account by coupling the FE models for the rotor and the stator subproblems to a model of the air gap solved analytically in terms of space harmonics[34],[35]. Such an air gap model can be interpreted as a D-to-N mapping from the viewpoint of the rotor and the stator subproblems[19].

In this work, we focus on representations of D-to-N mappings in terms of space and time harmonics.When the Fourier series expansions $(2.1) - (2.2)$ exist, D-to-N mapping maps Dirichlet coefficients to Neumann coefficients. In BVPs arising from rotating electrical machines, the D-to-N mappings can be often efficiently approximated by truncation of the Fourier series expansions $(2.1) - (2.2)$ to some finite set $\Lambda_\theta \subset \mathbb{Z}$ of space harmonics. This leads to a matrix representation of the mapping for each reformulated

subproblem in terms of the Dirichlet coefficients $\boldsymbol{D}$, Neumann coefficients $\boldsymbol{N}$ and the winding currents $\boldsymbol{I}$

$$\boldsymbol{N} \;=\; \Big[B\Big]\,\boldsymbol{D} + \Big[F\Big]\,\boldsymbol{I}. \tag{2.3}$$

We call these mappings *spectral Dirichlet-to-Neumann mappings*.

The matrix B completely characterizes the electromagnetic phenomenon in the subproblem in the absence of winding currents. The influence of the slots corresponds to the lines outside the diagonal as seen in the sparsity patterns in Figure 2.2.

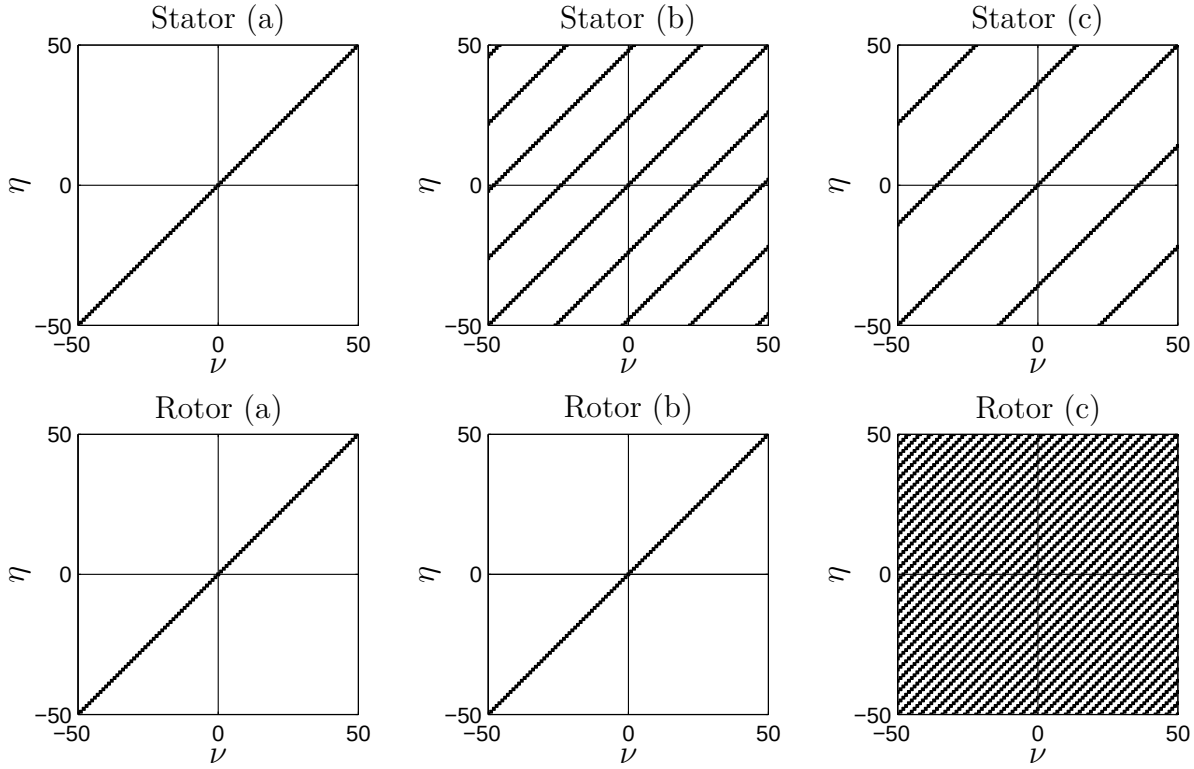

Figure 2.2: Sparsity graphs for the matrix B in (2.3) for the subproblems suggested in Figure 2.1.

Spectral D-to-N mappings can be used to speed up time-domain FE simulations when saturation can be ignored in at least one elliptic subproblem.When an elliptic subproblem is replaced, the solution of the FE equations for the reformulated subproblem is no longer necessary every time step. If both subproblems are elliptic and have negligible saturation, they can be both replaced with implicit Neumann boundary conditions on Γ_{sr}. Once the spectral D-to-N mappings have been constructed for both subproblems, no FE equations need to be solved for in the subsequent time-domain simulation. Both application scenarios and example test cases are discussed in the publication 4.

Reformulated subproblems can be coupled to electrical circuits and induction currents limited to windings in the reformulated subproblems can be taken into account this way.

2.3 Time harmonics in electrical machines

Consider a typical time-domain BVP for a rotating electrical machine excited with time-periodic currents or voltages and with the rotor rotating at a constant slip. The solution to such a problem typically contains transients, which fade gradually until the fields can be approximated to be time-periodic. Then, the solution is considered to be in *steady state* and can be expanded as a linear combination of sinusoidal functions of time.

To first approximation, the stator fields in most AC machines contain only the same time-frequencies as the stator winding currents. When the rotor is locked, passive and the material relations linear, this assumption strictly holds. Thus, a time-harmonic approximation at the synchronous frequency ω_s is often used for modeling the stator fields [36]. More generally, the effect of time harmonics in the stator winding currents can be taken into account by expansion of the stator fields as a Fourier series with respect to time with the synchronous frequency as the fundamental frequency [37]. However, rotation of a slotted rotor at a non-integer slip can lead to time-frequencies in the stator fields, that are not integer-multiples of the synchronous frequency [5]. We will show that for arbitrary rational-valued rotor slip, there exists a fundamental frequency ω_f so that the non-zero time-frequencies in the rotor and stator fields are always integer-multiples of ω_f.

Thus, we expand the magnetic stream function and its radial derivative on Γ_{sr} as a Fourier series of two variables: time t and mechanical angle θ. That is, we write

$$A|_{\Gamma_{sr}} = \sum_{\nu' \in \mathbb{Z}} \sum_{\nu \in \mathbb{Z}} \mathcal{D}_{\nu'\nu} e^{j(\nu' \omega_f t - \nu\theta)}, \tag{2.4}$$

$$\left.\frac{\partial A}{\partial r}\right|_{\Gamma_{sr}} = \sum_{\eta' \in \mathbb{Z}} \sum_{\eta \in \mathbb{Z}} \mathcal{N}_{\eta'\eta} e^{j(\eta' \omega_f t - \eta\theta)}, \tag{2.5}$$

where θ is the mechanical angle and $\mathcal{D}_{\nu'\nu}, \mathcal{N}_{\eta'\eta} \in \mathbb{C}$ holds for each $\eta', \eta, \nu', \nu \in \mathbb{Z}$. We call again the coefficients $\mathcal{D}_{\nu'\nu}$ and $\mathcal{N}_{\eta'\eta}$ the Dirichlet and Neumann coefficients, respectively.

Coupling of the rotor and stator subproblems requires continuity of the Dirichlet and Neumann data on the rotor-stator interface Γ_{sr}. For each subproblem in their own coordinate system, the non-zero time-frequencies in the Dirichlet data are equal to the non-zero time-frequencies in the magnetic stream function. However, when expressed in the rotor and stator coordinate systems, the non-zero time-frequencies in the Dirichlet and Neumann data are equal only when the rotor is locked. The relationships between time-frequencies of different subproblems are known as *slip transformations* and derived in chapter 4.

As in time-domain, spectral Dirichlet-to-Neumann mappings in frequency-domain map Dirichlet coefficients to Neumann coefficients and can be approximated by truncation to a finite set of harmonics $\Lambda \subset \mathbb{Z}^2$. This again leads to a matrix representation of the mapping for each subproblem in terms of the Dirichlet coefficients $\boldsymbol{\mathcal{D}}$, Neumann coefficients $\boldsymbol{\mathcal{N}}$ and the winding currents $\boldsymbol{\mathcal{I}}$

$$\boldsymbol{\mathcal{N}} = \left[\mathcal{B}\right] \boldsymbol{\mathcal{D}} + \left[\mathcal{F}\right] \boldsymbol{\mathcal{I}}. \tag{2.6}$$

In frequency-domain, spectral Dirichlet-to-Neumann mappings can be used to implement efficient numerical solution methods by replacing one or both subproblems with implicit Neumann boundary conditions. Unlike in time-domain, eddy-currents in massive conductors can be taken into account.

We will show how the sparsity patterns of the matrices in (2.6) can be used to accurately predict the non-zero harmonics in the Dirichlet and Neumann data. The sparsity patterns can be derived from the rotational symmetry of material parameters in slotted geometries.

Chapter 3

Time-Domain Spectral Dirichlet-to-Neumann mappings

In this chapter, we discuss the properties, applications, interpretation and the solution of time-domain spectral Dirichlet-to-Neumann mappings in more depth in the context of boundary value problems for rotating electrical machines. Further test cases and coupling of different types of models are discussed in the publication 4.

3.1 Rotor and stator subproblems

The cross-sectional domain Ω of the machine is divided into stator and rotor regions Ω_s and Ω_r, whose 1-dimensional common interface $\Gamma_{sr} = \partial\Omega_s \cap \partial\Omega_r$ is at the center of the air gap (see Fig. 3.1). The outer boundary of the stator is denoted by Γ_{ds} and the inner boundary of the rotor region by Γ_{dr}. The inner boundary Γ_{dr} may be empty[1]. We assume that the magnetic flux density has no component in the axial direction and that the current density is purely axial. An A_z-formulation with the magnetic stream function A corresponding to the magnetic vector potential is used.

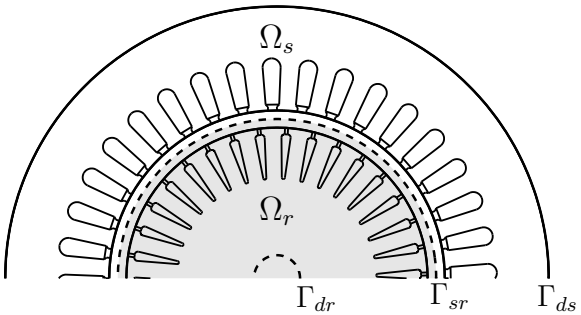

Figure 3.1: Half of the problem geometry. The air gap width is exaggerated.

[1]Note that when a reformulated stator subproblem is coupled to a FE model of the rotor, Γ_{dr} must be non-empty in order to quarantee uniqueness of the solution (see publication 4).

We use a pair of polar coordinate descriptions: one attached to the stator and the other attached to the rotor. The magnetic stream function is denoted by A_r and A_s for the rotor and the stator subproblems, respectively in their own coordinate systems. The two coordinate systems are related by the coordinate system transformation from the stator to the rotor system

$$\theta_r = \theta_s - \Delta\theta, \tag{3.1}$$

where $\Delta\theta$ is the mechanical rotation angle of the rotor with respect to the stator. Then, in order to satisfy the interface conditions for the magnetic flux density and the magnetic field strength on Γ_{sr}, we impose

$$A_r|_{\Gamma_{sr}}(\theta_r) = A_s|_{\Gamma_{sr}}(\theta_r + \Delta\theta), \tag{3.2}$$

$$\left.\frac{\partial A_r}{\partial r}\right|_{\Gamma_{sr}}(\theta_r) = \left.\frac{\partial A_s}{\partial r}\right|_{\Gamma_{sr}}(\theta_r + \Delta\theta). \tag{3.3}$$

Note that we have assumed in (3.3) that the interface Γ_{sr} is surrounded from both sides with a non-magnetic material. Thus, the factor $1/\mu_0$ is not included in (3.3).

3.2 Dirichlet and Neumann coefficients

The magnetic stream functions and their radial derivatives on Γ_{sr} are expanded in both coordinate systems as a Fourier expansion with respect to the mechanical angle. In order to facilitate numerical computation, the series expansions are truncated to a combination over a finite set of space harmonics

$$\Lambda_\theta = \left\{\nu_1, \nu_2, \ \ldots\ , \nu_{|\Lambda_\theta|}\right\} \subset \mathbb{Z}. \tag{3.4}$$

Thus, we expand

$$A_k|_{\Gamma_{sr}} = \sum_{\nu\in\Lambda_\theta} D_\nu^k e^{-j\nu\theta_k}, \tag{3.5}$$

$$\left.\frac{\partial A_k}{\partial r}\right|_{\Gamma_{sr}} = \sum_{\eta\in\Lambda_\theta} N_\nu^k e^{-j\eta\theta_k}, \tag{3.6}$$

where lower and upper indices $k \in \{s, r\}$ denote the stator or the rotor fields in their own coordinate systems. The Fourier series coefficients are stored in the vectors $\boldsymbol{D}^k, \boldsymbol{N}^k \in \mathbb{C}^{|\Lambda_\theta|}$, which are called the *Dirichlet and Neumann coefficients in coordinate system* k, respectively. Since A_k and its radial derivative must be real, conjugate symmetry $D_{-\nu}^k = D_\nu^{k*}$ and $N_{-\eta}^k = N_\eta^{k*}$ must hold for all $\nu, \eta \in \Lambda_\theta$, where $*$ denotes the complex conjugate.

Note that the truncation to finite number of harmonics Λ_θ makes the expansions (3.5) − (3.6) for the Dirichlet and Neumann data approximations. However, to avoid introduction of too many symbols, we write A_k also for the approximation resulting from the truncation.

3.2.1 Coordinate system transformations

Dirichlet and Neumann coefficients are assigned to rotor and stator fields in their own coordinate systems. Then substitution of $(3.5)-(3.6)$ into $(3.2)-(3.3)$ and the orthogonality of the complex exponential functions yield

$$\begin{aligned} D_\nu^r &= D_\nu^s e^{-j\nu\Delta\theta}, && (3.7)\\ N_\eta^r &= N_\eta^s e^{-j\nu\Delta\theta}. && (3.8) \end{aligned}$$

That is, we can write

$$\begin{aligned} \boldsymbol{D}^r &= \left[R_{\Delta\theta}\right]\boldsymbol{D}^s, && (3.9)\\ \boldsymbol{N}^r &= \left[R_{\Delta\theta}\right]\boldsymbol{N}^s, && (3.10) \end{aligned}$$

where $R_{\Delta\theta}$ is the diagonal *rotation matrix*

$$\left[R_{\Delta\theta}\right] := \text{diag}\left[e^{-j\nu_1\Delta\theta}, \quad ... \quad , e^{-j\nu_{|\Lambda_\theta|}\Delta\theta}\right]. \qquad (3.11)$$

3.3 Dirichlet-to-Neumann mappings for subproblems

Consider a stream function formulation for the subproblem $k \in \{s, r\}$. The boundary value problem can be written for each moment in time t: Find A_k defined in Ω_k such that

$$\begin{aligned} -\nabla\cdot\mu^{-1}\nabla A_k &= J^k(\boldsymbol{r},t), && (3.12)\\ A_k|_{\Gamma_{sr}} &= \sum_{\nu\in\Lambda_\theta} D_\nu^k(t)e^{-j\nu\theta}, && (3.13)\\ A_k|_{\Gamma_{dk}} &= 0 && (3.14) \end{aligned}$$

hold. In order to make application of the superposition principle possible, the subproblems to be reformulated with spectral Dirichlet-to-Neumann mappings are assumed to have linear material relations. Then, at every instant of time t, the solution to the BVP $(3.12)-(3.14)$ is linear with respect to both the current density J^k and the Dirichlet coefficients. Thus, when the current density J^k and the Dirichlet data are expanded as a linear combination of some known functions, the solution is linear combination of solutions to the BVP excited by invidual terms of these expansions. We assume that the current density can be written as a linear combination

$$J^k(\boldsymbol{r},t) = \sum_{l=1}^{m_k} I_l^k(t)J_l^k(\boldsymbol{r}), \qquad (3.15)$$

where J_l^k for each $l = 1, ..., m_k$ is a known current density corresponding to the unit current. Thus, we obtain the BVP for each moment in time t: Find A_k defined in Ω_k

such that

$$
\begin{aligned}
-\nabla \cdot \mu^{-1} \nabla A_k &= \sum_{l=1}^{m_k} I_l^k(t) J_l^k(\boldsymbol{r}), && (3.16)\\
A_k|_{\Gamma_{sr}} &= \sum_{\nu \in \Lambda_\theta} D_\nu^k(t) e^{-j\nu\theta}, && (3.17)\\
A_k|_{\Gamma_d} &= 0 && (3.18)
\end{aligned}
$$

hold. Then, by linearity, the solution to $(3.16) - (3.18)$ can be expanded as the combination

$$
A_k(\boldsymbol{r}, t) = \sum_{l=1}^{m_k} I_l^k(t) A_{ik}^l(\boldsymbol{r}) + \sum_{\nu \in \Lambda_\theta} D_\nu^k(t) \widetilde{A}_{dk}^\nu(\boldsymbol{r}), \tag{3.19}
$$

where A_{ik}^l for each independent current $l = 1, 2, ..., m$ is the solution to the boundary value problem

$$
\begin{aligned}
-\nabla \cdot \mu^{-1} \nabla A_{ik}^l &= J_l^k && (3.20)\\
A_{ik}^l\Big|_{\Gamma_{sr}} &= 0 && (3.21)\\
A_{ik}^l\Big|_{\Gamma_d} &= 0 && (3.22)
\end{aligned}
$$

and $\widetilde{A}_{dk}^\nu$ for each $\nu \in \Lambda_\theta$ is the solution to the boundary value problem

$$
\begin{aligned}
-\nabla \cdot \mu^{-1} \nabla \widetilde{A}_{dk}^\nu &= 0 && (3.23)\\
\widetilde{A}_{dk}^\nu\Big|_{\Gamma_{sr}} &= e^{-j\nu\theta} && (3.24)\\
\widetilde{A}_{dk}^\nu\Big|_{\Gamma_d} &= 0. && (3.25)
\end{aligned}
$$

The symbol $\sim$ denotes complex functions, whereas scalars are written without the symbol $\sim$. We call the BVP $(3.20) - (3.22)$ *the current problem for the current* l and $(3.23) - (3.25)$ *the Dirichlet problem for the space harmonic* ν.

Once the solutions to the boundary value problems $(3.20) - (3.22)$ and $(3.23) - (3.25)$ are found, the radial derivative of the magnetic stream function at Γ_{sr} can be expanded as follows

$$
\begin{aligned}
\left.\frac{\partial A_k}{\partial r}\right|_{\Gamma_{sr}}(\theta, t) &= \sum_{l=1}^{m_k} I_l^k(t) \left.\frac{\partial A_{ik}^l}{\partial r}\right|_{\Gamma_{sr}}(\theta) + \sum_{\nu \in \Lambda_\theta} D_\nu^k(t) \left.\frac{\partial \widetilde{A}_{dk}^\nu}{\partial r}\right|_{\Gamma_{sr}}(\theta) && (3.26)\\
&= \sum_{\eta' \in \Lambda_\theta} N_{\eta'}^k e^{-j\eta'\theta}.
\end{aligned}
$$

In order to solve for the Neumann coefficients N_η^k, let us define an inner product on $\theta \in [0, 2\pi]$

$$
\langle f, g \rangle_\theta := \frac{1}{2\pi} \int_0^{2\pi} f(\theta) g(\theta)^* \, d\theta. \tag{3.27}
$$

Application of (3.27) to (3.26) with $g = e^{-j\eta\theta}$ for each $\eta \in \Lambda_\theta$ yields

$$N_\eta^k = \sum_{l=1}^{m_k} I_l^k \left\langle \left.\frac{\partial A_{ik}^l}{\partial r}\right|_{\Gamma_{sr}}, e^{-j\eta\theta} \right\rangle_\theta + \sum_{\nu\in\Lambda_\theta} D_\nu^k \left\langle \left.\frac{\partial \widetilde{A}_{dk}^\nu}{\partial r}\right|_{\Gamma_{sr}}, e^{-j\eta\theta} \right\rangle_\theta . \tag{3.28}$$

We define the matrices $F^k \in \mathbb{C}^{|\Lambda_\theta|\times m_k}$ and $B^k \in \mathbb{C}^{|\Lambda_\theta|\times|\Lambda_\theta|}$ so that

$$F_{\eta l}^k = \left\langle \left.\frac{\partial A_{ik}^l}{\partial r}\right|_{\Gamma_{sr}}, e^{-j\eta\theta} \right\rangle_\theta , \tag{3.29}$$

$$B_{\eta\nu}^k = \left\langle \left.\frac{\partial \widetilde{A}_{dk}^\nu}{\partial r}\right|_{\Gamma_{sr}}, e^{-j\eta\theta} \right\rangle_\theta \tag{3.30}$$

hold. Thereafter, we obtain the truncated spectral Dirichlet-to-Neumann mapping for the subproblem k

$$\boxed{\boldsymbol{N}^k = \left[B^k\right]\boldsymbol{D}^k + \left[F^k\right]\boldsymbol{I}^k.} \tag{3.31}$$

Open Question 3.1 *If the exact solution to the full BVP was first obtained and then truncated to extract the Dirichlet and Neumann coefficients for the space harmonics in Λ_θ, the result would usually differ from the result of the approximate problem* (3.9) − (3.10), (3.16) − (3.18) *posed with data already truncated to Λ_θ. Upper limits for this error would be useful in the selection of Λ_θ and involve the theory of L^p-spaces on the interval* $[0, 2\pi]$ *[38].*

In the remainder of this chapter, we assume that the current density J^k is non-zero only on the winding cross sections in Ω_k. On each cross-sectional winding region, the current density is assumed to be constant. Typically, each independent current density corresponds to a phase in the windings.

Open Question 3.2 *Is there an efficient approach for coupling more general induction currents such as the induction currents in massive conductors with the discussed time-domain method? For example, approximation by a system of a very long period and impulse response techniques appear unpromising.*

Since the construction of the spectral Dirichlet-to-Neumann mapping relies on superposition, the mappings can be easily constructed only for subproblems with linear material parameters. The assumption of linear material parameters in the reformulated subproblems is the main limitation of the discussed method. However, if saturation can be neglected in only one subproblem, a non-linear FE model for the remaining subproblem can be coupled with the reformulated problem (see publication 4).

Generalization to subproblems with significant saturation by linearization might be feasible when the permeability distribution can be approximated to be independent of time. In more general situations, reconstruction of the linearized Dirichlet-to-Neumann map between time steps as the saturation state changes with time would make the approach unfeasible in terms of solution time compared to standard FE solution.

Open Question 3.3 *Can the approach be generalized to some specific class of subproblems with non-negligible saturation?*

Generalization to subproblems that contain permanent magnets is straightforward when the BH curves for the permanent magnet materials can be approximated to be affine. The remanent magnetization of the material then corresponds to an additional source term in (3.12)[7].Application of (3.27) then leads to an additional source term in (3.28) and (3.31).

3.3.1 Circuit coupling

In reformulated subproblems, circuit coupling is used for both voltage control and to model induction currents in windings. In order to couple the reformulated subproblem to external circuits, a relation between voltages, currents and Dirichlet coefficients is required.

Let $S_1^k, S_2^k, ..., S_{Q_k}^k$ be the cross sectional coil regions within the subproblem k with areas $A_1^k, A_2^k, ..., A_{Q_k}^k$ and the number of conductors $z_1^k, z_2^k, ..., z_{Q_k}^k$. Let us define a matrix $C^k \in \mathbb{R}^{m_k \times Q_k}$ so that

$$C_{cq}^k := \begin{cases} 1, & S_q^k \text{ is in winding } c \text{ with direction } +z \\ -1, & S_q^k \text{ is in winding } c \text{ with direction } -z \\ 0, & S_q^k \text{ is not in winding } c \end{cases} \tag{3.32}$$

holds. Then the magnetic flux through the winding c can be estimated

$$\Phi_c^k = L \sum_{q=1}^{Q_k} C_{cq}^k \frac{z_q^k}{A_q^k} \int_{S_q^k} A_k \, da, \tag{3.33}$$

where L is the length of the active area of the rotor (see Figure 3.2).

Substitution of (3.19) into (3.33) yields

$$\Phi_c^k = L \sum_{q=1}^{Q_k} C_{cq}^k \frac{z_q^k}{A_q^k} \left(\sum_{l=1}^{m_k} I_l^k \int_{S_q^k} A_{ik}^l \, da + \sum_{\nu \in \Lambda_\theta} D_\nu^k \int_{S_q^k} \tilde{A}_{dk}^\nu \, da \right). \tag{3.34}$$

Definition of the matrices $Q^{Dk} \in \mathbb{C}^{m_k \times |\Lambda_\theta|}$ and $Q^{Ik} \in \mathbb{C}^{m_k \times m_k}$ as

$$Q_{c\nu}^{Dk} = L \sum_{q=1}^{Q_k} C_{cq}^k \frac{z_q^k}{A_q^k} \int_{S_q^k} \tilde{A}_{dk}^\nu \, da \tag{3.35}$$

$$Q_{cl}^{Ik} = L \sum_{q=1}^{Q_k} C_{cq}^k \frac{z_q^k}{A_q^k} \int_{S_q^k} A_{ik}^l \, da \tag{3.36}$$

leads to the magnetic flux expression

$$\boldsymbol{\Phi}^k = \left[Q^{Dk} \right] \boldsymbol{D}^k + \left[Q^{Ik} \right] \boldsymbol{I}^k. \tag{3.37}$$

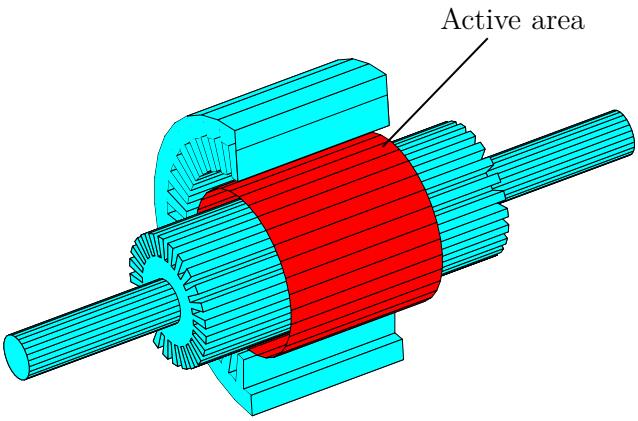

Figure 3.2: Active area of the rotor. The air gap width is exaggerated.

We call Q^{Dk} and Q^{Ik} the *circuit coupling matrices of subproblem k*. Let us write the resistances of the windings into a diagonal matrix $R^k \in \mathbb{C}^{m_k \times m_k}$. Thereafter, the voltages over the windings can be written

$$\begin{aligned} \boldsymbol{V}_p^k &= \left[R^k\right] \boldsymbol{I}^k + \frac{d}{dt}\boldsymbol{\Phi}^k \\ &= \left[R^k\right] \boldsymbol{I}^k + \left[Q^{Ik}\right] \frac{d}{dt}\boldsymbol{I}^k + \left[Q^{Dk}\right] \frac{d}{dt}\boldsymbol{D}^k. \end{aligned} \tag{3.38}$$

Note that the voltages in $\boldsymbol{V}_p^k$ are the voltages over m_k series-connected windings. For example, the relationship between phase source voltages in AC machines and the voltages in V_p^k are specified by additional circuit equations (see publication 4).

3.3.2 Numerical solution

We will now derive the equations for the numerical solution of (3.20) – (3.22) and (3.23) – (3.25) by the finite element method. The solutions are then used to construct approximations for the matrices B^k and F^k.

Let us call by Ψ_n^k the standard nodal element basis functions corresponding to the finite element discretization of the region Ω_k [25]. Then A_{ik}^l and A_{dk}^ν for each $l = 1, ..., m_k$ and $\nu \in \Lambda_\theta$ are approximated by

$$\mathcal{A}_{ik}^l := \sum_{n=1}^{N_k} a_{nl}^{ik} \Psi_n^k \approx A_{ik}^l, \tag{3.39}$$

$$\widetilde{\mathcal{A}}_{dk}^\nu := \sum_{n=1}^{N_k} a_{n\nu}^{dk} \Psi_n^k \approx \widetilde{A}_{dk}^\nu, \tag{3.40}$$

where N_k is the number of nodes in the mesh for Ω_k and $a_{nl}^{ik}, a_{n\nu}^{dk} \in \mathbb{C}$ hold for each n. As usual with Galerkin methods, we select the test functions to span the approximation

space. Application to (3.20) – (3.22) and (3.23) – (3.25) for each $l = 1, \ldots, m_k$ and $\nu \in \Lambda_\theta$, respectively yields

$$\left[S^k\right] \boldsymbol{a}_l^{ik} + \boldsymbol{g}_i^{kl} = \boldsymbol{f}_l^{ik}, \tag{3.41}$$

$$\left[S^k\right] \boldsymbol{a}_\nu^{dk} + \boldsymbol{g}_d^{k\nu} = \boldsymbol{0}, \tag{3.42}$$

where $S^k \in \mathbb{C}^{N_k \times N_k}$ is the complete stiffness matrix and $\boldsymbol{f}_l^{ik} \in \mathbb{C}^{N_k}$ the excitation vector, i.e.

$$S_{mn}^k = \int_{\Omega_k} \mu^{-1} \nabla \Psi_m \cdot \nabla \Psi_n \, da, \tag{3.43}$$

$$f_{lm}^{ik} = \int_{\Omega_k} \Psi_m J_l^k \, da, \tag{3.44}$$

$$g_{im}^{kl} = \int_{\partial\Omega_k} \Psi_m \frac{\partial \mathcal{A}_{ik}^l}{\partial n} \, dl, \tag{3.45}$$

$$g_{dm}^{k\nu} = \int_{\partial\Omega_k} \Psi_m \frac{\partial \widetilde{\mathcal{A}}_{dk}^\nu}{\partial n} \, dl \tag{3.46}$$

hold. Suppose the coefficients in vectors $\boldsymbol{a}_l^{ik}$ and $\boldsymbol{a}_\nu^{dk}$ appear in the order

$$\boldsymbol{a}_l^{ikT} = \begin{bmatrix} \boldsymbol{a}_{Fl}^{ikT} & \boldsymbol{a}_{Il}^{ikT} & \boldsymbol{a}_{Bl}^{ikT} \end{bmatrix}, \tag{3.47}$$

$$\boldsymbol{a}_l^{dkT} = \begin{bmatrix} \boldsymbol{a}_{F\nu}^{dkT} & \boldsymbol{a}_{I\nu}^{dkT} & \boldsymbol{a}_{B\nu}^{dkT} \end{bmatrix}, \tag{3.48}$$

where

- $\boldsymbol{a}_I$ correspond to the N_I^k nodes on the interface Γ_{sr}, ordered according to the mechanical angle.
- $\boldsymbol{a}_B$ correspond to the N_B^k nodes on the outer boundary Γ_d.
- $\boldsymbol{a}_F$ correspond to the N_F^k remaining nodes.

The boundary conditions (3.24) and (3.21) are weakly enforced by weighting their both sides with the FE basis functions. Substitution of (3.40) and (3.39) to (3.24) and (3.21), respectively and application of the L_2 inner product (3.27) with each basis function, yields systems of linear equations

$$\left[E^k\right] \boldsymbol{a}_{I\nu}^{dk} = \boldsymbol{d}_\nu^k, \tag{3.49}$$

$$\left[E^k\right] \boldsymbol{a}_{Il}^{ik} = \boldsymbol{0}, \tag{3.50}$$

where $E^k \in \mathbb{R}^{|\Lambda_\theta| \times |\Lambda_\theta|}$ and $\boldsymbol{d}_\nu^k \in \mathbb{C}^{N_I^k}$ are defined such that

$$E_{mn}^k := \left\langle \Psi_{In}^k\big|_{\Gamma_{sr}}, \Psi_{Im}^k\big|_{\Gamma_{sr}} \right\rangle_\theta, \tag{3.51}$$

$$d_{\nu m}^k := \left\langle e^{-j\nu\theta}, \Psi_{Im}^k\big|_{\Gamma_{sr}} \right\rangle_\theta, \tag{3.52}$$

hold. Thereafter, BVPs (3.20) – (3.22) and (3.23) – (3.25) for each $\nu \in \Lambda_\theta$ and $l = 1, \ldots, m_k$ can be written as

$$\begin{bmatrix} S_{FF}^k & S_{FI}^k \\ 0 & E^k \end{bmatrix} \begin{bmatrix} \boldsymbol{a}_{Fl}^{ik} \\ \boldsymbol{a}_{Il}^{ik} \end{bmatrix} = \begin{bmatrix} \boldsymbol{f}_l^k \\ \boldsymbol{0} \end{bmatrix}, \tag{3.53}$$

$$\begin{bmatrix} S_{FF}^k & S_{FI}^k \\ 0 & E^k \end{bmatrix} \begin{bmatrix} \boldsymbol{a}_{F\nu}^{dk} \\ \boldsymbol{a}_{I\nu}^{dk} \end{bmatrix} = \begin{bmatrix} \boldsymbol{0} \\ \boldsymbol{d}_\nu^k \end{bmatrix}. \tag{3.54}$$

Note that the system matrix is the same for all space harmonics (3.24) and source currents (3.21). All differences appear in the excitation vector. Thus, with a direct solver, factorization of the system matrix can be computed once and for all. Addition of harmonics into Λ_θ then only calls for more forward and back substitutions. However, the memory required to store the results may become large, especially if a dense mesh is used.

Once the equations (3.53) and (3.54) have been solved for each $\nu \in \Lambda_\theta$ and $l = 1, \ldots, m_k$, approximations for the matrices B^k and F^k can be constructed from the Fourier series expansions of the radial component of the stream function on Γ_{sr} by (3.29) – (3.30). Thus, we define matrices $G^I \in \mathbb{C}^{|\Lambda_\theta| \times N_I^k}$ and $G^F \in \mathbb{C}^{|\Lambda_\theta| \times N_F^k}$ such that

$$G_{\eta n}^I = \left\langle \left. \frac{\partial \Psi_{In}^k}{\partial r} \right|_{\Gamma_{sr}}, e^{-j\eta\theta} \right\rangle_\theta, \tag{3.55}$$

$$G_{\eta n}^F = \left\langle \left. \frac{\partial \Psi_{Fn}^k}{\partial r} \right|_{\Gamma_{sr}}, e^{-j\eta\theta} \right\rangle_\theta \tag{3.56}$$

hold. Thereafter, the matrices B^k and F^k of (3.31) can be computed

$$\left[B^k\right] = \left[G^I\right] \left[\boldsymbol{a}_{I\nu_1}^{dk}, \ \ldots \ , \boldsymbol{a}_{I\nu_{|\Lambda_\theta|}}^{dk}\right] + \left[G^F\right] \left[\boldsymbol{a}_{F\nu_1}^{dk}, \ \ldots \ , \boldsymbol{a}_{F\nu_{|\Lambda_\theta|}}^{dk}\right], \tag{3.57}$$

$$\left[F^k\right] = \left[G^I\right] \left[\boldsymbol{a}_{I1}^{ik}, \ \ldots \ , \boldsymbol{a}_{Im_k}^{ik}\right] + \left[G^F\right] \left[\boldsymbol{a}_{F1}^{ik}, \ \ldots \ , \boldsymbol{a}_{Fm_k}^{ik}\right]. \tag{3.58}$$

3.3.3 Green's reciprocity theorem

The matrices F^k and Q^{Dk} turn out to be related by the Green's reciprocity theorem [39]. The reciprocity theorem for the fields $\widetilde{A}_{dk}^\nu$ and A_{ik}^l can be expressed as

$$\begin{aligned} &\int_{\Omega_k} \left[\widetilde{A}_{dk}^\nu \nabla \cdot \left(\mu^{-1} \nabla A_{ik}^l \right) - A_{ik}^l \nabla \cdot \left(\mu^{-1} \nabla \widetilde{A}_{dk}^\nu \right) \right] da \\ = &\oint_{\partial\Omega_k} \mu^{-1} \left(\widetilde{A}_{dk}^\nu \frac{\partial A_{ik}^l}{\partial r} - A_{ik}^l \frac{\partial \widetilde{A}_{dk}^\nu}{\partial r} \right) dl. \end{aligned} \tag{3.59}$$

Application to (3.20) – (3.22) and (3.23) – (3.25), yields

$$\int_{\Omega_k} \widetilde{A}_{dk}^\nu J_l^k \, da = \oint_{\Gamma_{sr}} \frac{1}{\mu_0} e^{-j\nu\theta} \frac{\partial A_{ik}^l}{\partial r} \, dl = \frac{2\pi r_\delta}{\mu_0} F_{\nu l}^{k*}, \tag{3.60}$$

where r_δ is the radius of the circle Γ_{sr}. Expansion of the unit current density in phase l J_l^k on left-hand side of (3.60) with (3.32) and the substitution (3.35) for Q^{Dk}, yields

$$\int_{\Omega_k} \widetilde{A}_{dk}^{\nu} J_l^k \, da \;=\; \sum_{q=1}^{Q_k} C_{lq}^k \frac{z_q^k}{A_q^k} \int_{S_q^k} \widetilde{A}_{dk}^{\nu} \, da = \frac{1}{L} Q_{l\nu}^{Dk}. \tag{3.61}$$

Combination of (3.60) − (3.61) for each $\nu \in \Lambda_\theta$ and $l = 1, ..., m_k$ leads to the relation

$$F^k \;=\; \frac{\mu_0}{2\pi r_\delta L} Q^{DkH}, \tag{3.62}$$

where H denotes the conjugate transpose of the matrix. Thus, the matrix F^k can be computed out of Q^{Dk} without the solution of the BVP (3.20) − (3.22). On the other hand, when the subproblem k is coupled to electrical circuits, computation of the matrix Q^{Ik} seems to require solution of the current problem (3.20)−(3.22). Note that when the matrices F^k and Q^{Dk} have been constructed from the numerical solution of (3.20)−(3.22) and (3.23) − (3.25), the equation (3.62) holds only approximately.

Open Question 3.4 *Is there a way to compute the matrix Q^{Ik} without the solution of* (3.20) − (3.22)*?*

3.4 Post-Processing

Since radial and tangential components of the magnetic flux density are readily available from the Fourier series representations (3.2) − (3.3), the computation of many post-processing quantities such as forces and torques is simple and efficient [40]. Thus, in the numerical solution of any BVP with a reformulated subproblem, it is useful to include the Dirichlet coefficient vector to the degrees of freedom. Once a solution has been obtained, the Neumann coefficient vector can be easily computed by the spectral D-to-N mapping (3.31).

The radial component of the magnetic flux density and the tangential component of the magnetic field strength can be expanded as

$$B_r^k(\theta_k, t) \;=\; \frac{1}{r_\delta} \left. \frac{\partial A_k}{\partial \theta_k} \right|_{\Gamma_{sr}} = -\frac{j}{r_\delta} \sum_{\nu \in \Lambda_\theta} \nu D_\nu^k e^{-j\nu\theta_k}, \tag{3.63}$$

$$H_t^k(\theta_k, t) \;=\; -\frac{1}{\mu_0} \left. \frac{\partial A_k}{\partial r} \right|_{\Gamma_{sr}} = -\frac{1}{\mu_0} \sum_{\eta \in \Lambda_\theta} N_\eta^k e^{-j\nu\theta_k}, \tag{3.64}$$

where r_δ is the radius of the circle Γ_{sr} and μ_0 is the permeability of the vacuum.

3.4.1 Poynting vector and power flow

The radial component of the Poynting vector can be expressed as

$$\begin{aligned} \boldsymbol{S}^k \cdot \hat{\mathbf{r}} &= \boldsymbol{E}^k \times \boldsymbol{H}^k \cdot \hat{\mathbf{r}} && (3.65)\\ &= -E_z^k H_t^k && (3.66)\\ &= -\left(\frac{\partial}{\partial t}\sum_{\nu\in\Lambda_\theta} D_\nu^k e^{-j\nu\theta}\right)\frac{1}{\mu_0}\sum_{\eta\in\Lambda_\theta} N_\eta^k e^{-j\eta\theta} && (3.67)\\ &= -\frac{1}{\mu_0}\sum_{\eta\in\Lambda_\theta}\sum_{\nu\in\Lambda_\theta} N_\eta^k \frac{dD_\nu^k}{dt} e^{-j(\nu+\eta)\theta}, && (3.68) \end{aligned}$$

where $\hat{\mathbf{r}}$ is the unit vector in the radial direction. Integrating over Γ_{sr} gives the power flux per unit length into the rotor region

$$\begin{aligned} -\int_{\Gamma_{sr}} \boldsymbol{E}\times\boldsymbol{H}\cdot\hat{\mathbf{r}}\, dl &= \frac{r_\delta}{\mu_0}\sum_{\eta\in\Lambda_\theta}\sum_{\nu\in\Lambda_\theta} N_\eta^k \frac{dD_\nu^k}{dt}\int_0^{2\pi} e^{-j(\eta+\nu)\theta} && (3.69)\\ &= \frac{2\pi r_\delta}{\mu_0}\sum_{\nu\in\Lambda_\theta}\frac{dD_\nu^k}{dt}N_\nu^{k*}. && (3.70) \end{aligned}$$

3.4.2 Torque

The torque can be calculated by means of the Maxwell Stress Tensor [40]

$$T = \frac{Lr_\delta}{\mu_0}\int_{\Gamma_{sr}} B_n B_t\, dl \qquad (3.71)$$

where B_n and B_t are the normal and tangential components of the magnetic flux density, respectively. Substitution of (3.63) – (3.64) for B_n and B_t, yields

$$\begin{aligned} T &= \frac{Lr_\delta}{\mu_0}\sum_{\nu\in\Lambda_\theta}\sum_{\eta\in\Lambda_\theta} j\nu N_\eta D_\nu \int_0^{2\pi} e^{-j(\eta+\nu)}\, d\theta\\ &= \frac{2\pi L r_\delta}{\mu_0}\sum_{\nu\in\Lambda_\theta} j\nu D_\nu N_\nu^*. && (3.72) \end{aligned}$$

3.4.3 Force

The total force per unit length on the rotor can be written as [40]

$$\begin{aligned} \boldsymbol{F} &= \frac{1}{2\mu_0}\int_{\Gamma_{sr}} (B_n^2 - B_t^2)\,\hat{\mathbf{r}}\, dl\\ &= \frac{r_\delta}{2\mu_0}\mathrm{Re}\left\{\int_0^{2\pi}(B_n^2 - B_t^2)e^{j\theta}\begin{bmatrix}1\\-j\end{bmatrix} d\theta\right\}. && (3.73) \end{aligned}$$

With (3.63) – (3.64), the squared components of the magnetic flux can be written as

$$B_t^2 = \sum_{\nu\in\Lambda_\theta}\sum_{\nu'\in\Lambda_\theta} N_\nu N_{\nu'} e^{-j\theta(\nu+\nu')} \tag{3.74}$$

$$B_n^2 = \frac{1}{r_\delta^2}\sum_{\nu\in\Lambda_\theta}\sum_{\nu'\in\Lambda_\theta} \nu\nu' D_\nu D_{\nu'} e^{-j\theta(\nu+\nu')}. \tag{3.75}$$

When substituted for B_t^2 and B_n^2 in (3.73), the integral is zero for the terms with $\nu' \neq 1-\nu$. Thus, we get

$$\boldsymbol{F} = \begin{bmatrix} \mathrm{Re}\,\mathcal{F} \\ \mathrm{Im}\,\mathcal{F} \end{bmatrix} \tag{3.76}$$

for $\mathcal{F}$ defined as

$$\mathcal{F} := \frac{r_\delta \pi}{\mu_0}\sum_{\nu\in\Lambda_\theta}\left(\frac{\nu(1-\nu)}{r_\delta^2} D_\nu D_{1-\nu} - N_\nu N_{1-\nu}\right). \tag{3.77}$$

The relationship between space harmonics with adjacent indices and the unbalanced magnetic pull is well known in the literature [41].

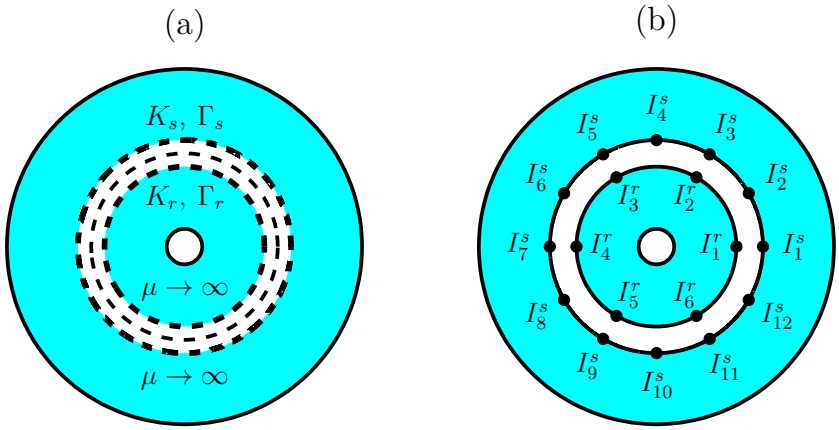

Figure 3.3: (a) Geometry of the simple model. (b) Concentrated windings with $Q_r = 6$ and $Q_s = 12$. Each dot corresponds to z_q^k turns.

3.5 Example of an analytical solution

As an example of an analytical solution, we will derive exact solutions for the model suggested in Figure 2.1*a* and repeated for convenience in Figure 3.3a. Air gap is surrounded by infinitely permeable round rotor and stator regions with surface current sheets K_r and K_s.

We start by derivation of the analytical solutions to the BVPs (3.20) – (3.22) and (3.23) – (3.25). The winding currents for both subproblems are expanded as a Fourier

series of sinusoidal current sheets with respect to the mechanical angle. The spectral Dirichlet-to-Neumann mapping (3.31) can be then expressed in terms of diagonal matrices. Then, different space harmonics are independent and the problem can be solved one space harmonic at a time. This enables pen-and-paper analysis and should be useful in development of intuition.

As discussed in chapter 2, this type of models are very closely related to the simple models used in elementary textbooks [2, 3]. The solutions derived in this section help understand the properties and limitations of such models.

3.5.1 Dirichlet problem

Let Γ_k be the circular interface of radius $r_k = r_\delta + s_k g$ between the air gap and the core material in subproblem k, where g is half of the air gap width and $s_s = 1, s_r = -1$ hold. The general solution to the Dirichlet problem (3.23) – (3.25) for the harmonic $\nu \in \mathbb{Z}$ in the air gap can be written as (see publication 2)

$$\widetilde{A}^{\nu}_{dk}(r,\theta) \;=\; \left(a_{k\nu} r^{\nu} + b_{k\nu} r^{-\nu}\right) e^{-j\nu\theta}. \tag{3.78}$$

The infinite permeability of the core material implies the boundary condition

$$\left.\frac{\partial A^{\nu}_{dk}}{\partial r}\right|_{\Gamma_k}(\theta) \;=\; \nu\left(a_{k\nu} r_k^{\nu-1} - b_{k\nu} r_k^{-(\nu+1)}\right) = 0, \tag{3.79}$$

which implies $b_{k\nu} = r_k^{2\nu} a_{k\nu}$. Then, the boundary condition (3.24) can be written as

$$\left.\widetilde{A}^{\nu}_{dk}\right|_{\Gamma_{sr}}(\theta) \;=\; a_{k\nu}\left(r_\delta^{\nu} + r_k^{2\nu} r_\delta^{-\nu}\right) e^{-j\nu\theta} = e^{-j\nu\theta}. \tag{3.80}$$

The constant $a_{k\nu}$ can be thus solved for

$$a_{k\nu} \;=\; \frac{1}{r_\delta^{\nu} + r_k^{2\nu} r_\delta^{-\nu}} \tag{3.81}$$

and the solution can be expanded

$$\widetilde{A}^{\nu}_{dk}(r,\theta) \;=\; \frac{r^{\nu} + r_k^{2\nu} r^{-\nu}}{r_\delta^{\nu} + r_k^{2\nu} r_\delta^{-\nu}} e^{-j\nu\theta}. \tag{3.82}$$

Thereafter, differentation of (3.82) with respect to r, yields

$$\left.\frac{\partial \widetilde{A}^{\nu}_{dk}}{\partial r}\right|_{\Gamma_{sr}}(\theta) \;=\; \nu\,\frac{r_\delta^{\nu-1} - r_k^{2\nu} r_\delta^{-(\nu+1)}}{r_\delta^{\nu} + r_k^{2\nu} r_\delta^{-\nu}} e^{-j\nu\theta}. \tag{3.83}$$

After truncation to a finite set of space harmonics Λ_θ, elements of the diagonal matrix B^k can be solved for:

$$B^k_{\nu\nu} \;=\; \frac{\nu}{r_\delta}\frac{r_\delta^{2\nu} - r_k^{2\nu}}{r_\delta^{2\nu} + r_k^{2\nu}}. \tag{3.84}$$

3.5.2 Current sheet approximation

In order to solve the BVP (3.20) – (3.22) for the subproblem k, we expand the current sheet K_k as a Fourier series with respect to the mechanical angle

$$K_k(\theta) = \sum_{\gamma\in\mathbb{Z}} \kappa_\gamma^k e^{-j\gamma\theta}, \tag{3.85}$$

where for each $\gamma \in \mathbb{Z}$, $\kappa_\gamma^k \in \mathbb{C}$ and $\kappa_{-\gamma}^k = \kappa_\gamma^{k*}$ hold. If concentrated windings with z_q turns and currents I_q are located on Γ_k at mechanical angles $\theta = 2\pi q/Q_k$ (see Figure 3.3b), the current sheet can be expanded as

$$K_k(\theta) = \sum_{q=1}^{Q_k} \frac{z_q^k I_q^k}{r_k} \delta\left(\theta - 2\pi\frac{q}{Q_k}\right), \tag{3.86}$$

where δ is the Dirac delta function. Thereafter, we can solve for

$$\begin{aligned}
\kappa_\gamma^k &= \frac{1}{2\pi}\int_0^{2\pi} K_k(\theta) e^{j\gamma\theta}\, d\theta \qquad (3.87)\\
&= \frac{1}{2\pi r_k}\sum_{q=1}^{Q_k} z_q^k I_q^k \int_0^{2\pi} e^{j\gamma\theta}\delta\left(\theta - \frac{2\pi q}{Q_k}\right) d\theta\\
&= \frac{1}{2\pi r_k}\sum_{q=1}^{Q_k} z_q^k I_q^k \exp j\frac{2\pi q\gamma}{Q_k}.
\end{aligned}$$

After truncation to a finite set of space harmonics Λ_θ, (3.87) can be expressed in the matrix form

$$\boldsymbol{\kappa}^k = \left[W^k\right]\boldsymbol{I}^k. \tag{3.88}$$

3.5.3 Current problem

The general solution to the BVP (3.20) – (3.22) in the air gap is first derived for each Fourier series term $\gamma \in \Lambda_\theta$. We will show that for each $\gamma \in \Lambda_\theta$, the solution $\widetilde{A}_{ik}^\gamma$ will contain only the space harmonic γ, which implies that the matrix $\mathcal{F}^k \in \mathbb{C}^{|\Lambda_\theta|\times|\Lambda_\theta|}$ is diagonal. Then the matrix $F^k := \mathcal{F}^k W^k \in \mathbb{C}^{|\Lambda_\theta|\times Q_k}$ maps the slot winding currents to their contribution in the Neumann coefficients.

Solution to the BVP (3.20) – (3.22) for each $\gamma \in \Lambda_\theta$ can be written as

$$\widetilde{A}_{ik}^\gamma(r,\theta) = \left(a_{k\gamma} r^\gamma + b_{k\gamma} r^{-\gamma}\right) e^{-j\gamma\theta}. \tag{3.89}$$

The boundary condition (3.21) can be written

$$\widetilde{A}_{ik}^\gamma\Big|_{\Gamma_{sr}}(\theta) = \left(a_{k\gamma} r_\delta^\gamma + b_{k\gamma} r_\delta^{-\gamma}\right) e^{-j\gamma\theta} = 0, \tag{3.90}$$

which implies $b_{k\gamma} = -r_\delta^{2\gamma} a_{k\gamma}$. On Γ_k, the interface condition for magnetic field strength can be written [42]

$$H_{o\theta} - H_{i\theta} = s_k K_k, \tag{3.91}$$

where $H_{i\theta}$ and $H_{o\theta}$ are the tangential components of the magnetic field strength inside and outside the core material of the subproblem k. Since the core material is infinitely permeable, $H_{i\theta} = 0$ holds. Thus, the current sheet $K_k(\theta) := e^{-j\gamma\theta}$ on Γ_k corresponds to the boundary condition

$$\left.\frac{\partial \widetilde{A}^{\gamma}_{ik}}{\partial r}\right|_{\Gamma_k}(\theta) = \gamma a_{k\gamma}\left(r_k^{\gamma-1} + r_\delta^{2\gamma} r_k^{-(\gamma+1)}\right) e^{-j\gamma\theta} = s_k \mu_0 e^{-j\gamma\theta}. \tag{3.92}$$

The constant $a_{k\gamma}$ can be thus solved for:

$$a_{k\gamma} = \frac{1}{\gamma}\frac{s_k\mu_0}{r_k^{\gamma-1} + r_\delta^{2\gamma} r_k^{-(\gamma+1)}} \tag{3.93}$$

and the solution can be expanded

$$\widetilde{A}^{\gamma}_{ik}(r,\theta) = \frac{s_k\mu_0}{\gamma}\frac{r^\gamma - r_\delta^{2\gamma} r^{-\gamma}}{r_k^{\gamma-1} + r_\delta^{2\gamma} r_k^{-(\gamma+1)}} e^{-j\gamma\theta}. \tag{3.94}$$

Thereafter, we obtain the expression

$$\begin{aligned}\mathcal{F}^k_{\gamma\gamma} &= s_k\mu_0 \frac{r_\delta^{\gamma-1} + r_\delta^{2\gamma} r_k^{-(\gamma+1)}}{r_k^{\gamma-1} + r_\delta^{2\gamma} r_k^{-(\gamma+1)}} \\ &= 2 s_k \mu_0 \frac{r_\delta^{\gamma-1} r_k^{\gamma+1}}{r_\delta^{2\gamma} + r_k^{2\gamma}}.\end{aligned} \tag{3.95}$$

3.5.4 Circuit coupling

Substitution of the solutions (3.82) and (3.94) to (3.33), yields the flux through the concentrated winding c

$$\begin{aligned}\Phi^k_c &= L\sum_{q=1}^{Q_k} C^k_{cq} z^k_q A_k\left(r_k, \frac{2\pi q}{Q_k}\right) \\ &= L\sum_{q=1}^{Q_k} C^k_{cq} z^k_q \sum_{\nu\in\Lambda_\theta} D_\nu \frac{2 r_k^\nu r_\delta^\nu}{r_\delta^{2\gamma} + r_k^{2\gamma}} \exp\left(-j\frac{2\pi q\nu}{Q_k}\right) \\ &+ s_k\mu_0 L\sum_{q=1}^{Q_k} C^k_{cq} z^k_q \sum_{\gamma\in\Lambda_\theta} \kappa^k_\gamma \frac{1}{\gamma r_k}\frac{r_k^{2\gamma} - r_\delta^{2\gamma}}{r_k^{2\gamma} + r_\delta^{2\gamma}} \exp\left(-j\frac{2\pi q\gamma}{Q_k}\right).\end{aligned} \tag{3.96}$$

Thus, the circuit coupling matrices (3.35) – (3.36) can be solved for

$$Q^D_{c\nu} = L\sum_{q=1}^{Q_k} C_{cq} z^k_q \frac{2 r_k^\nu r_\delta^\nu}{r_\delta^{2\gamma} + r_k^{2\gamma}} \exp\left(-j\frac{2\pi q\nu}{Q_k}\right), \tag{3.97}$$

$$Q^I_{cl} = \sum_{\gamma\in\Lambda_\theta} \mathcal{Q}^k_{c\gamma} W^k_{\gamma l}, \tag{3.98}$$

where $\mathcal{Q}^I_{c\gamma}$ is defined by

$$\mathcal{Q}^I_{c\gamma} = s_k\mu_0 L\sum_{q=1}^{Q_k} C^k_{cq} z^k_q \frac{1}{\gamma r_k}\frac{r_k^{2\gamma} - r_\delta^{2\gamma}}{r_k^{2\gamma} + r_\delta^{2\gamma}} \exp\left(-j\frac{2\pi q\gamma}{Q_k}\right). \tag{3.99}$$

3.5.5 Solution

The spectral Dirichlet-to-Neumann mappings for both subproblems can now be written as

$$\boldsymbol{N}^s = \left[\mathcal{F}^s\right]\boldsymbol{\kappa}^s + \left[B^s\right]\boldsymbol{D}^s, \tag{3.100}$$

$$\boldsymbol{N}^r = \left[\mathcal{F}^r\right]\boldsymbol{\kappa}^r + \left[B^r\right]\boldsymbol{D}^r. \tag{3.101}$$

Since the matrices $B^s, B^r, \mathcal{F}^s$ and $\mathcal{F}^r$ constructed according to (3.84) and (3.95) are diagonal, we obtain for each $\nu \in \Lambda_\theta$

$$N^s_\nu = \mathcal{F}^s_{\nu\nu}\kappa^s_\nu + B^s_{\nu\nu}D^s_\nu, \tag{3.102}$$

$$N^r_\nu = \mathcal{F}^r_{\nu\nu}\kappa^r_\nu + B^r_{\nu\nu}D^r_\nu. \tag{3.103}$$

Application of (3.9) − (3.10) to (3.102) − (3.103) yields the Dirichlet coefficients

$$\begin{aligned} D^s_\nu &= \frac{e^{-j\nu\Delta\theta}\mathcal{F}^s_{\nu\nu}\kappa^s_\nu - \mathcal{F}^r_{\nu\nu}\kappa^r_\nu}{B^r_{\nu\nu}e^{-j\nu\Delta\theta} - e^{-j\nu\Delta\theta}B^s_{\nu\nu}} \\ &= \frac{\mathcal{F}^s_{\nu\nu}\kappa^s_\nu - e^{j\nu\Delta\theta}\mathcal{F}^r_{\nu\nu}\kappa^r_\nu}{B^r_{\nu\nu} - B^s_{\nu\nu}}. \end{aligned} \tag{3.104}$$

3.5.6 Small air gap approximation

When the air gap is small, by the Binomial theorem: we can approximate

$$r_k^{2\nu} = (r_\delta + s_k g)^{2\nu} = \sum_{n=0}^{2\nu}\binom{2\nu}{n} r_\delta^{2\nu-n}(s_k g)^n \approx r_\delta^{2\nu} + 2\nu s_k g r_\delta^{2\nu-1}. \tag{3.105}$$

Application of (3.105) to the numerator of (3.84) can be used to obtain the approximations

$$B^k_{\nu\nu} = \frac{\nu}{r_\delta}\frac{r_\delta^{2\nu} - r_k^{2\nu}}{r_\delta^{2\nu} + r_k^{2\nu}} \approx -\frac{s_k\nu}{r_\delta}\frac{2\nu g r_\delta^{2\nu-1}}{2r_\delta^{2\nu}} = -\frac{s_k\nu^2 g}{r_\delta^2}, \tag{3.106}$$

$$\mathcal{F}^k_{\nu\nu} = 2s_k\mu_0\frac{r_\delta^{\gamma-1}r_k^{\gamma+1}}{r_\delta^{2\gamma} + r_k^{2\gamma}} \approx s_k\mu_0. \tag{3.107}$$

Substitution of (3.106) and (3.107) back to (3.104) and application of (3.102) yields

$$D^s_\nu = \mu_0\frac{r_\delta^2}{2g\nu^2}\left(\kappa^s_\nu + e^{j\nu\Delta\theta}\kappa^r_\nu\right), \tag{3.108}$$

$$N^s_\nu = \frac{\mu_0}{2}\left(\kappa^s_\nu - e^{j\nu\Delta\theta}\kappa^r_\nu\right). \tag{3.109}$$

The post-processing quantities can be computed with the methods presented in the section 3.4. Thus, the radial flux density and the tangential component of the magnetic

field strength can be written at the center of the air gap

$$B_r^s|_{\Gamma_{sr}}(\theta) = -\frac{j}{r_\delta}\sum_{\nu\in\Lambda_\theta}\nu D_\nu^s e^{-j\nu\theta} \tag{3.110}$$
$$= -j\mu_0\sum_{\nu\in\Lambda_\theta}\frac{r_\delta}{2g\nu}\left(\kappa_\nu^s + e^{j\nu\Delta\theta}\kappa_\nu^r\right)e^{-j\nu\theta},$$
$$H_\theta^s|_{\Gamma_{sr}}(\theta) = -\frac{1}{\mu_0}\sum_{\eta\in\Lambda_\theta}N_\eta^s e^{-j\eta\theta} \tag{3.111}$$
$$= -\sum_{\eta\in\Lambda_\theta}\frac{1}{2}\left(\kappa_\eta^s - e^{j\eta\Delta\theta}\kappa_\eta^r\right)e^{-j\eta\theta}$$

For example, the electromagnetic torque can be then computed using (3.72)

$$T = \frac{2\pi L r_\delta}{\mu_0}\sum_{\nu\in\Lambda_\theta} j\nu D_\nu N_\nu^* \tag{3.112}$$
$$= \frac{\mu_0\pi L r_\delta^3}{2g}\sum_{\nu\in\Lambda_\theta}\frac{j}{\nu}\left(\kappa_\nu^s + e^{j\nu\Delta\theta}\kappa_\nu^r\right)\left(\kappa_\nu^{s*} - e^{-j\nu\Delta\theta}\kappa_\nu^{r*}\right)$$
$$= \frac{\mu_0\pi L r_\delta^3}{2g}\sum_{\nu\in\Lambda_\theta}\frac{j}{\nu}\left(|\kappa_\nu^s|^2 - |\kappa_\nu^r|^2 + 2\mathrm{Im}\left\{e^{-j\nu\Delta\theta}\kappa_\nu^s\kappa_\nu^{r*}\right\}\right)$$
$$= -\frac{\mu_0\pi L r_\delta^3}{2g}\sum_{\nu\in\Lambda_\theta}\frac{2}{\nu}|\kappa_\nu^s||\kappa_\nu^r|\sin\left(\arg\kappa_\nu^s - \arg\kappa_\nu^r - \nu\Delta\theta\right).$$

The torque formula (3.112) is equivalent to expressions obtained in literature [2].

3.6 Interpretation of the matrices

The sparsity patterns of the matrices B^k and F^k of the spectral D-to-N mapping explain which space harmonics arise. This information can be then used in the selection of the truncated set Λ_θ of space harmonics to be included in the model. In this section, we derive the sparsity patterns from the rotational symmetries of slotted geometries in the BVPs (3.23) – (3.25) and (3.20) – (3.22). We show how the sparsity patterns can be used to predict the non-zero space harmonics.

3.6.1 Symmetries and slotted geometries

Let Q_k be the number of slots in the subproblem k. By *rotational symmetry of the materials*, we mean that the predicate

$$\mu(r,\theta + 2\pi q/Q_k) = \mu(r,\theta) \quad \forall q\in\mathbb{Z} \quad \forall r,\theta \tag{3.113}$$

holds. Then, it follows that the solution to the Dirichlet problem (3.23) – (3.25) at each point of Ω_k satisfies the predicate

$$\widetilde{A}_{dk}^\nu(r,\theta + 2\pi q/Q_k) = \widetilde{A}_{dk}^\nu(r,\theta)e^{-j2\pi\nu q/Q_k} \quad \forall q\in\mathbb{Z}. \tag{3.114}$$

This can be shown as follows: Let $q \in \mathbb{Z}$ and $\widetilde{A}_{dk}^{\nu q}$ be the solution to the boundary value problem $(3.23) - (3.25)$ with the modified boundary condition

$$\widetilde{A}_{dk}^{\nu q}\Big|_{\Gamma_{sr}} \quad = \quad e^{-j\nu(\theta+2\pi q/Q_k)}. \tag{3.115}$$

The modified BVP (3.23), (3.25), (3.115) is equivalent to the original BVP $(3.23)-(3.25)$ rotated clockwise by q slots in the sense that

$$\widetilde{A}_{dk}^{\nu q}(r,\theta) \quad = \quad \widetilde{A}_{dk}^{\nu}(r,\theta + q2\pi/Q_k) \tag{3.116}$$

holds. On the other hand, $\widetilde{A}_{dk}^{\nu} e^{-j\nu 2\pi q/Q_k}$ is also solution to the modified BVP (3.23), (3.25), (3.115). Thus, by uniqueness of the solution of the Dirichlet problem $\widetilde{A}_{dk}^{\nu q} = \widetilde{A}_{dk}^{\nu} e^{-j\nu 2\pi q/Q_k}$ must hold. Combination of this with (3.116), yields for all points in Ω_k

$$\widetilde{A}_{dk}^{\nu}(r,\theta + q2\pi/Q_k) \quad = \quad \widetilde{A}_{dk}^{\nu q}(r,\theta) = \widetilde{A}_{dk}^{\nu}(r,\theta) e^{-j\nu q 2\pi/Q_k}. \tag{3.117}$$

□

Note that the field symmetry condition (3.114) doesn't generally hold for boundary value problems with currents or for problems including both stator and the rotor. However, elements of the matrix B^k can be computed by substitution of (3.114) back to (3.30)

$$\begin{aligned}
B_{\eta\nu}^k &= \frac{1}{2\pi}\int_0^{2\pi} \frac{\partial \widetilde{A}_{dk}^{\nu}}{\partial r}\bigg|_{\Gamma_{sr}} \exp j\eta\theta \, d\theta \qquad (3.118)\\
&= \frac{1}{2\pi}\sum_{q=1}^{Q_k}\int_0^{2\pi/Q_k} \frac{\partial \widetilde{A}_{dk}^{\nu}}{\partial r}\bigg|_{\Gamma_{sr}} (\theta + 2\pi q/Q_k) \exp j\eta\left(\theta + 2\pi\frac{q}{Q_k}\right) \, d\theta\\
&= \frac{1}{2\pi}\sum_{q=1}^{Q_k}\int_0^{2\pi/Q_k} \frac{\partial \widetilde{A}_{dk}^{\nu}}{\partial r}\bigg|_{\Gamma_{sr}} (\theta) \exp j\left(\eta\theta + 2\pi q\frac{\eta-\nu}{Q_k}\right) \, d\theta\\
&= \frac{1}{2\pi}\left[\sum_{q=1}^{Q_k} \exp j2\pi q\frac{\eta-\nu}{Q_k}\right]\int_0^{2\pi/Q_k} \frac{\partial \widetilde{A}_{dk}^{\nu}}{\partial r}\bigg|_{\Gamma_{sr}} (\theta) e^{j\eta\theta} \, d\theta.
\end{aligned}$$

The geometric sum in the brackets is zero unless

$$\eta \quad = \quad \nu + nQ_k \tag{3.119}$$

holds for some $n \in \mathbb{Z}$. This explains the sparsity patterns for the matrices as seen in Figure 2.2. The more slots there are in the geometry of a subproblem, the sparser the matrix B is. For continuously axisymmetric problems, the matrix B is diagonal.

In order to investigate the symmetry properties of the boundary value problems $(3.20)-(3.22)$, let us select the slot winding currents $I_q^k : q = 1, ..., Q_k$ as the independent currents. We expand the winding currents as a discrete Fourier series

$$I_q^k \quad = \quad \frac{1}{Q_k}\sum_{\gamma=-Q_k/2}^{Q_k/2-1} O_\gamma^k \exp\left(-j\frac{2\pi\gamma q}{Q_k}\right), \tag{3.120}$$

where O_γ^k is called the *space harmonic γ in the slot winding currents* of subproblem k and it satisfies

$$O_\gamma^k = \sum_{q=1}^{Q_k} I_q^k \exp\left(j\frac{2\pi\gamma q}{Q_k}\right). \tag{3.121}$$

Equation (3.120) can be written in the matrix form

$$\boldsymbol{I}^k = \left[\zeta^k\right]\boldsymbol{O}^k, \tag{3.122}$$

where $\zeta^k \in \mathbb{C}^{Q_k\times Q_k}$ holds and satisfies $\left[\zeta^k\right]^* = Q_k\left[\zeta^k\right]^{-1}$.

For example, if there are m_k phases in a single-layer integral-slot winding, the slots can be partitioned into subsets of $Q_k/(2pm_k)$ adjacent slots with equal currents [30]. Then, for balanced m_k-phase currents with amplitude $\hat{I}$, the space harmonic γ becomes

$$\begin{aligned} O_\gamma^k &= \sum_{\alpha=1}^{Q_k/(2pm_k)}\sum_{\beta=1}^{2pm_k}\frac{\hat{I}}{2}\left[\exp j\left(\frac{2\pi}{2pm_k}p\beta\right)+\exp -j\left(\frac{2\pi}{2pm_k}p\beta\right)\right] &(3.123)\\ &\cdot \quad \exp j\left[\frac{2\pi}{Q_k}\gamma\left(\alpha+\frac{Q_k}{2pm_k}\beta\right)\right] \\ &= \frac{\hat{I}}{2}\sum_{\alpha=1}^{Q_k/(2pm_k)}\exp j\left(\frac{2\pi}{Q_k}\gamma\alpha\right)\sum_{\beta=1}^{2pm_k}\left[\exp\frac{j\pi\beta}{pm_k}(\gamma-p)+\exp\frac{j\pi\beta}{pm_k}(\gamma+p)\right] &(3.124)\end{aligned}$$

The geometric series in square brackets is zero unless

$$\gamma = p(2m_kn\pm 1) \tag{3.125}$$

holds for some $n\in\mathbb{Z}$ Thus, expression (3.124) simplifies to

$$O_\gamma^k = \begin{cases} pm_k\hat{I}\sum_{\alpha=1}^{Q_k/(2pm_k)}\exp j\frac{2\pi p}{Q_k}\gamma\alpha, & \gamma = p(2m_kn\pm 1)\\ 0, & \text{otherwise}\end{cases}. \tag{3.126}$$

The solution of the BVP

$$-\nabla\cdot\mu^{-1}\nabla\widetilde{A}_{Ik}^\gamma = \sum_{q=1}^{Q_k}\exp\left(-j\frac{2\pi\gamma q}{Q_k}\right)J_q^k \tag{3.127}$$

$$\widetilde{A}_{Ik}^\gamma\Big|_{\Gamma_{sr}} = 0 \tag{3.128}$$

$$\widetilde{A}_{Ik}^\gamma\Big|_{\Gamma_{dk}} = 0 \tag{3.129}$$

for each $\gamma\in\mathbb{Z}$ satisfies the rotational symmetry

$$\widetilde{A}_{Ik}^\gamma(r,\theta+2\pi q/Q_k) = \widetilde{A}_{Ik}^\gamma(r,\theta)\exp\left(-j\frac{2\pi\gamma q}{Q_k}\right). \tag{3.130}$$

Open Question 3.5 *The solutions to BVPs* (3.23)−(3.25) *and* (3.127)−(3.129) *satisfy rotational symmetry with respect to rotations of a single slot. Does this imply that the matrices* B^k *and* F^k *for each subproblem could be constructed by solving BVPs in a geometry reduced to a single slot?*

The repetition of the symmetry argument leading to (3.119) for the BVP (3.127)−(3.129) shows that space harmonics γ in the slot currents influence the Neumann coefficients of orders

$$\eta \;=\; \gamma + nQ_k, \tag{3.131}$$

where $n \in \mathbb{Z}$ holds. Note that while there are at most Q_k space harmonics γ in the slot currents, there is potentially an infinite number of space harmonics in the Neumann data. Equation (3.131) determines the sparsity pattern for the matrix $F^k\zeta^k \in \mathbb{C}^{|\Lambda_\theta|\times Q_k}$. Even though the matrices F^k and ζ^k are both dense, their product $F^k\zeta^k$ for slotted geometries with large number of slots can be sparse.

For balanced m_k-phase currents, substitution of (3.125) for γ in (3.131) yields

$$\eta \;=\; p(2m_k n_1 \pm 1) + n_2 Q_k. \tag{3.132}$$

3.6.2 The air gap and space harmonics

Each column in the matrix B^k characterizes the response of the subproblem k driven with the boundary condition (3.24) in the absense of winding currents. Zero-valued column ν in B^k is equivalent to an infinite permeability in the whole region Ω_k in the solution of (3.23) − (3.25). In most subproblems arising from rotating electrical machines, the interface Γ_{sr} is surrounded by an air gap and slotted material with finite permeability. Therefore, the matrix B^k seldom contains zero columns.

If the space harmonic index ν becomes large enough, the radial flux corresponding to the boundary condition (3.24) crossing the air gap becomes negligible. Then the slotting doesn't significantly influence Neumann data and off-diagonal elements in the column ν of the matrix B^k can be safely ignored.

3.6.3 Sparsity patterns and space harmonics

In order to predict the non-zero space harmonics in the Dirichlet and Neumann data obtained from a solution of a problem involving both subproblems, suppose that a spectral Dirichlet-to-Neumann mapping has been constructed for both subproblems. That is, we have matrices $B^s, B^r \in \mathbb{C}^{|\Lambda_\theta|\times|\Lambda_\theta|}$ and $F^s \in \mathbb{C}^{|\Lambda_\theta|\times m_s}$, $F^r \in \mathbb{C}^{|\Lambda_\theta|\times m_r}$ such that

$$\boldsymbol{N}^s \;=\; \left[B^s\right]\boldsymbol{D}^s + \left[F^s\right]\boldsymbol{I}^s, \tag{3.133}$$

$$\boldsymbol{N}^r \;=\; \left[B^r\right]\boldsymbol{D}^r + \left[F^r\right]\boldsymbol{I}^r \tag{3.134}$$

hold. Application of (3.6), (3.9) – (3.10) and (3.122) then yields a system of linear equations

$$\left[B^r R_{\Delta\theta} - R_{\Delta\theta} B^s\right] \boldsymbol{D}^s \;=\; \left[R_{\Delta\theta} F^s \zeta^s\right] \boldsymbol{O}^s - \left[F^r \zeta^r\right] \boldsymbol{O}^r. \tag{3.135}$$

Open Question 3.6 *Is the system on left-hand side of* (3.135) *always invertible?*

To save space, let's denote $B^{r'} := R_{\Delta\theta} B^r$ and $B^{s'} := B^s R_{\Delta\theta}$. Coordinate system transformations (3.9) – (3.10) do not affect the sparsity patterns. Then, row η of (3.135) can be expanded with the use of (3.119)

$$\sum_{n\in\mathbb{Z}} \left(B^{r'}_{\eta(\eta+nQ_r)} D^s_{\eta+nQ_r} - B^{s'}_{\eta(\eta+nQ_s)} D^s_{\eta+nQ_s} \right) = \left(\left[R_{\Delta\theta} F^s \zeta^s\right] \boldsymbol{O}^s - \left[F^r \zeta^r\right] \boldsymbol{O}^r \right)_\eta . \tag{3.136}$$

To understand how space harmonics arise in the Dirichlet and Neumann data, first note that the solution $\boldsymbol{D}^s$ of (3.135) is linear with respect to the vectors $\boldsymbol{O}^s$ and $\boldsymbol{O}^r$.

Suppose initially that the slot winding currents contain only the space harmonic γ for the subproblem k whereas the remaining harmonics in slot winding currents for both subproblems are zero. Then, (3.131) implies that the right-hand side of (3.135) can attain non-zero values only on the rows $\eta \in \{\gamma + nQ_k : n \in \mathbb{Z}\}$. The left-hand side of (3.136) for each η introduces an interdependence between the space harmonics $\nu \in \{\eta + n_1 Q_r + n_2 Q_s : n_1, n_2 \in \mathbb{Z}\}$ in the Dirichlet data and the term on the right-hand side. Thus, space harmonic γ in the slot winding currents of either subproblem may only give rise to the space harmonics

$$\nu \in [\gamma] \;:=\; \{\gamma + n_1 Q_r + n_2 Q_s : n_1, n_2 \in \mathbb{Z}\} \tag{3.137}$$

in the Dirichlet data. The remaining space harmonics $\nu \notin [\gamma]$ in the Dirichlet data are independent of the space harmonics in $[\gamma]$. If γ was the only non-zero space harmonic in slot winding currents, the space harmonics $\nu \notin [\gamma]$ would disappear when (3.135) has a unique solution.

The set $[\gamma]$ is the equivalence class of γ with the equivalence relation

$$\mathcal{R} \;:=\; \left\{(\eta, \nu) \in \mathbb{Z}^2 : \exists n_1, n_2 \in \mathbb{Z} : \nu = \eta + n_1 Q_r + n_2 Q_s\right\}. \tag{3.138}$$

All space harmonics can then be partitioned into the quotient set of sets of interdependent harmonics denoted by $\mathbb{Z}/\mathcal{R}$. The space harmonics in each equivalence class are interdependent of each other and the space harmonic γ in the slot winding currents.

Let $\Lambda_r, \Lambda_s \subset \mathbb{Z}$ be the non-zero space harmonics in the slot winding currents of the rotor and stator subproblems, respectively. By the preceding argument, the set of non-zero space harmonics in the Dirichlet data can be then predicted to be

$$\boxed{\Lambda_\theta \;\subseteq \bigcup_{\gamma\in\Lambda_r\cup\Lambda_s} [\gamma].} \tag{3.139}$$

Chapter 4

Frequency-Domain Spectral Dirichlet-to-Neumann mappings

The application of the time-domain approach presented in chapter 3 is straightforward only to elliptic subproblems where the current density in conducting regions can be assumed to be uniform. This suggests that modeling of e.g. induction currents in massive conductors requires a different kind of approach.

In this chapter, we discuss spectral Dirichlet-to-Neumann mappings in frequency-domain BVPs arising from rotating electrical machines. In frequency-domain, Dirichlet-to-Neumann mappings for subproblems are expressed in terms of Fourier series expansions of two variables: time t and mechanical angle θ. Then, subproblems with eddy-currents in massive conductors can be reformulated. In particular, we will explain the method discussed in publication 2 involving analytical solutions for the rotor subproblem in a BVP for solid-rotor induction machine in this more general framework.

We will also discuss how the time-frequency content of the fields in both subproblems can be predicted by means of generalized slip transformations.

4.1 Formulation

As in chapter 3, magnetic stream functions A_s and A_r are used in the stator and rotor regions Ω_s and Ω_r, in their respective coordinate systems. The change of coordinates from the stator to the rotor system is

$$\boldsymbol{u} : \mathbb{R}^2 \to \mathbb{R}^2 \quad : \quad \begin{bmatrix} r_s \\ \theta_s \end{bmatrix} \mapsto \begin{bmatrix} r_r \\ \theta_r \end{bmatrix} := \begin{bmatrix} r_s \\ \theta_s - (1-s)\dfrac{\omega_s}{p} t \end{bmatrix}, \tag{4.1}$$

where s is the rotor slip and p is the number of pole pairs. If A is the magnetic stream function in the whole problem domain expressed in the stator coordinate system, the stream function in the rotor coordinate system is [1] $A_r := A|_{\Omega_r} \circ \boldsymbol{u}^{-1}$.

[1] Note that unlike in the publication 2, we denote the magnetic stream function in the rotor coordinate system by A_r instead of a.

For simplicity, assume that the rotor subproblem is passive and the stator subproblem is current-driven. Material relations in both subproblems are assumed linear. Then, the time-domain BVPs for the stator and rotor regions can be written: Find A_r defined in Ω_r and A_s defined in Ω_s such that

$$\begin{aligned} \nabla \cdot \mu^{-1} \nabla A_s &= -J^s && (4.2) \\ \nabla \cdot \mu^{-1} \nabla A_r &= \sigma \frac{\partial A_r}{\partial t}, && (4.3) \end{aligned}$$

hold in Ω_s and Ω_r and on the boundaries Γ_{ds} and Γ_{dr}, conditions

$$\begin{aligned} A_s|_{\Gamma_{ds}} &= 0 && (4.4) \\ A_r|_{\Gamma_{dr}} &= 0 && (4.5) \end{aligned}$$

hold, where σ is electric conductivity, μ the magnetic permeability and J^s is the prescribed scalar field describing the z-directional current density. The rotor and stator subproblems are coupled at Γ_{sr} by the interface conditions

$$\begin{aligned} A_s|_{\Gamma_{sr}} \left(\theta_s + (1-s)\frac{\omega_s}{p} t, t \right) &= A_r|_{\Gamma_{sr}} (\theta_s, t), && (4.6) \\ \left. \frac{\partial A_s}{\partial r} \right|_{\Gamma_{sr}} \left(\theta_s + (1-s)\frac{\omega_s}{p} t, t \right) &= \left. \frac{\partial A_r}{\partial r} \right|_{\Gamma_{sr}} (\theta_s, t). && (4.7) \end{aligned}$$

4.2 Dirichlet and Neumann coefficients

To a first approximation, the stator fields can be assumed to contain the same time-frequencies as the stator winding currents. Thus, a time-harmonic approximation at the synchronous frequency ω_s only is often used for modeling stator fields in AC machines [36]. More generally, the influence of time harmonics in the stator winding currents can be taken into account by a Fourier expansion of the stator fields with the synchronous frequency as the fundamental frequency [37]. However, we will show that the rotation of a slotted rotor at a non-integer slip can lead to time-frequencies that are not integer multiples of the synchronous frequency. Therefore, the selection of the fundamental frequency ω_f for the Fourier series expansion requires care. Only when the rotor slip s is an integer or the rotor continuously axisymmetric, the synchronous frequency can be used as the fundamental frequency.

Let us expand the magnetic stream function A and its radial derivative on the interface Γ_{sr} in the stator polar coordinate system as a Fourier series of two variables: time t and mechanical angle θ_s. To facilitate numerical computation, the series is truncated to a finite set of harmonics

$$\begin{aligned} \Lambda &= \{(\nu', \nu) \in \Lambda_t \times \Lambda_\theta\} && (4.8) \\ &= \left\{\nu'_1, \nu'_2, \ \dots, \nu'_{|\Lambda_t|}\right\} \times \left\{\nu_1, \nu_2, \ \dots, \nu_{|\Lambda_\theta|}\right\} \subset \mathbb{Z}^2, \end{aligned}$$

where $\nu'_m = \eta'_m$ for each $m = 1, 2, \ldots, |\Lambda_t|$ and $\nu_n = \eta_n$ for each $n = 1, 2, \ldots, |\Lambda_\theta|$ are the time and space harmonic numbers, respectively. Thereafter, we expand

$$A_s|_{\Gamma_{sr}} = \sum_{(\nu',\nu)\in\Lambda} \mathcal{D}_{\nu'\nu} e^{j(\nu'\omega_f t - \nu\theta_s)}, \tag{4.9}$$

$$\left.\frac{\partial A_s}{\partial r}\right|_{\Gamma_{sr}} = \sum_{(\eta',\eta)\in\Lambda} \mathcal{N}_{\eta'\eta} e^{j(\eta'\omega_f t - \eta\theta_s)}, \tag{4.10}$$

where A_s is the restriction of A to Ω_s. The Fourier series coefficients are stored in the Dirichlet and Neumann coefficient vectors $\boldsymbol{\mathcal{D}}, \boldsymbol{\mathcal{N}} \in \mathbb{C}^{|\Lambda|}$, where $|\Lambda| = |\Lambda_t||\Lambda_\theta|$ holds. Time harmonic indices are denoted with primes. Since A_s is real-valued, conjugate symmetries $\mathcal{D}_{-\nu'-\nu} = \mathcal{D}^*_{\nu'\nu}$ and $\mathcal{N}_{-\eta'-\eta} = \mathcal{N}^*_{\eta'\eta}$ must hold for all $(\nu',\nu),(\eta',\eta) \in \Lambda$. Unlike in the time-domain, in frequency-domain we use Fourier series expansions for the Dirichlet and Neumann data $(4.9) - (4.10)$ only in the stator coordinate system. The coordinate system transformations $(4.6) - (4.7)$ are then only needed for the construction of the spectral Dirichlet-to-Neumann mapping for the rotor.

The vectors $\boldsymbol{\mathcal{D}}$ and $\boldsymbol{\mathcal{N}}$ are ordered so that they can be partitioned into vectors according to the time harmonic index

$$\boldsymbol{\mathcal{D}} = \left[\boldsymbol{\mathcal{D}}^T_{\nu'_1},\ \boldsymbol{\mathcal{D}}^T_{\nu'_2},\ \ldots\ ,\boldsymbol{\mathcal{D}}^T_{\nu'_{|\Lambda_t|}}\right]^T, \tag{4.11}$$

$$\boldsymbol{\mathcal{N}} = \left[\boldsymbol{\mathcal{N}}^T_{\eta'_1},\ \boldsymbol{\mathcal{N}}^T_{\eta'_2},\ \ldots\ ,\boldsymbol{\mathcal{N}}^T_{\eta'_{|\Lambda_t|}}\right]^T, \tag{4.12}$$

where for each $m = 1, \ldots, |\Lambda_t|$

$$\boldsymbol{\mathcal{D}}_{\nu'_m} = \left[\mathcal{D}_{\nu'_m\nu_1},\ \mathcal{D}_{\nu'_m\nu_2},\ \ldots\ ,\mathcal{D}_{\nu'_m\nu_{|\Lambda_\theta|}}\right]^T, \tag{4.13}$$

$$\boldsymbol{\mathcal{N}}_{\eta'_m} = \left[\mathcal{N}_{\eta'_m\eta_1},\ \mathcal{N}_{\eta'_m\eta_2},\ \ldots\ ,\mathcal{N}_{\eta'_m\eta_{|\Lambda_\theta|}}\right]^T \tag{4.14}$$

hold. The stator winding currents are expanded in time as a truncated Fourier series

$$I^s_l = \sum_{\eta'\in\Lambda_t} I^s_{l\eta'} e^{j\eta'\omega_f t}, \tag{4.15}$$

where $I_{l\eta'} \in \mathbb{C}$ holds for each $l = 1, ..., m_s$ and $\eta' \in \Lambda_t$. Then, substitution of (4.15) back to (3.15) yields

$$J^s(\boldsymbol{r},t) = \sum_{\eta'\in\Lambda_t} e^{j\eta'\omega_f t} \sum_{l=1}^{m_k} I^s_{\eta' l} J^s_l(\boldsymbol{r}). \tag{4.16}$$

The coefficients $I_{\eta' l}$ are assembled into a vector $\boldsymbol{\mathcal{I}} \in \mathbb{C}^{m_s|\Lambda_t|}$, that can be partitioned into vectors according to time harmonics index

$$\boldsymbol{\mathcal{I}} = \left[\boldsymbol{\mathcal{I}}^T_{\eta'_1},\ \boldsymbol{\mathcal{I}}^T_{\eta'_2},\ \ldots,\ \boldsymbol{\mathcal{I}}^T_{\eta'_{|\Lambda_t|}}\right]^T, \tag{4.17}$$

where for each $n = 1, ..., |\Lambda_t|$

$$\boldsymbol{\mathcal{I}}_{\eta'_n} = \left[I_{\eta_n 1},\ I_{\eta_n 2},\ \ldots,\ I_{\eta_n m_s}\right]^T \tag{4.18}$$

holds.

4.3 Spectral Dirichlet-to-Neumann mappings for subproblems

We aim to reformulate both subproblems with spectral Dirichlet-to-Neumann mappings. That is, we seek matrices $\mathcal{B}^r, \mathcal{B}^s \in \mathbb{C}^{|\Lambda|\times|\Lambda|}$ and $\mathcal{F}^s \in \mathbb{C}^{|\Lambda|\times m_s}$ so that

$$\begin{aligned} \boldsymbol{\mathcal{N}} &= \left[\mathcal{B}^s\right]\boldsymbol{\mathcal{D}} + \left[\mathcal{F}^s\right]\boldsymbol{\mathcal{I}}^s, \\ \boldsymbol{\mathcal{N}} &= \left[\mathcal{B}^r\right]\boldsymbol{\mathcal{D}} \end{aligned} \tag{4.19}$$

hold. If the stator winding currents $\boldsymbol{\mathcal{I}}^s$ are known, the Dirichlet coefficients can be then solved from the system of linear equations

$$\boxed{\left(\left[\mathcal{B}^r\right] - \left[\mathcal{B}^s\right]\right)\boldsymbol{\mathcal{D}} \quad = \quad \left[\mathcal{F}^s\right]\boldsymbol{\mathcal{I}}^s.} \tag{4.20}$$

The partition used for the Dirichlet and Neumann coefficients $(4.11) - (4.12)$ and stator currents (4.17) induces the following partition of the matrices $\mathcal{B}^s, \mathcal{B}^r$ and $\mathcal{F}^s$ into blocks according to the time harmonic index as follows:

$$\left[\mathcal{B}^k\right] = \begin{bmatrix} \mathcal{B}^k_{\eta'_1\nu'_1} & \mathcal{B}^k_{\eta'_1\nu'_2} & \dots & \mathcal{B}^k_{\eta'_1\nu'_{|\Lambda_t|}} \\ \mathcal{B}^k_{\eta'_2\nu'_1} & \mathcal{B}^k_{\eta'_2\nu'_2} & \dots & \mathcal{B}^k_{\eta'_2\nu'_{|\Lambda_t|}} \\ \vdots & \vdots & \ddots & \vdots \\ \mathcal{B}^k_{\eta'_{|\Lambda_t|}\nu'_1} & \mathcal{B}^k_{\eta'_{|\Lambda_t|}\nu'_2} & \dots & \mathcal{B}^k_{\eta'_{|\Lambda_t|}\nu'_{|\Lambda_t|}} \end{bmatrix}, \tag{4.21}$$

$$\left[\mathcal{F}^k\right] = \begin{bmatrix} \mathcal{F}^k_{\eta'_1\nu'_1} & \mathcal{F}^k_{\eta'_1\nu'_2} & \dots & \mathcal{F}^k_{\eta'_1\nu'_{|\Lambda_t|}} \\ \mathcal{F}^k_{\eta'_2\nu'_1} & \mathcal{F}^k_{\eta'_2\nu'_2} & \dots & \mathcal{F}^k_{\eta'_2\nu'_{|\Lambda_t|}} \\ \vdots & \vdots & \ddots & \vdots \\ \mathcal{F}^k_{\eta'_{|\Lambda_t|}\nu'_1} & \mathcal{F}^k_{\eta'_{|\Lambda_t|}\nu'_2} & \dots & \mathcal{F}^k_{\eta'_{|\Lambda_t|}\nu'_{|\Lambda_t|}} \end{bmatrix}. \tag{4.22}$$

Then, the blocks on the diagonal of the matrix $\mathcal{B}^r - \mathcal{B}^s$ couple equal time-frequencies in the Dirichlet and Neumann data whereas off-diagonal blocks couple different time-frequencies. Section 4.4 explains how the sparsity graph of matrix $\mathcal{B}^r - \mathcal{B}^s$ in terms of blocks can be then used to understand how time harmonics arise.

4.3.1 Stator subproblem

The stator subproblem for each time harmonic ν' can be modeled with the method discussed in chapter 3. Thus, in the stator coordinate system, each time-frequency in the winding currents or Dirichlet data is coupled to the equal time-frequency in the Neumann data and the matrices $(4.21) - (4.22)$ for the stator subproblem can be expressed in the block diagonal form.

Combination of (4.9) and (4.16) with (4.2) and (4.4) yields a BVP for the stator region: Find A_s defined in Ω_s that satisfies

$$\nabla \cdot \mu^{-1} \nabla A_s = -\sum_{\nu' \in \Lambda_t} \sum_{l=1}^{m_s} \mathcal{I}^s_{\nu' l} e^{j\nu'\omega_f t} J^s_l, \tag{4.23}$$

$$A_s|_{\Gamma_{sr}} = \sum_{\nu' \in \Lambda_t} \sum_{\nu \in \Lambda_\theta} \mathcal{D}_{\nu'\nu} e^{j(\nu'\omega_f t - \nu\theta_s)}, \tag{4.24}$$

$$A_s|_{\Gamma_{ds}} = 0. \tag{4.25}$$

By linearity, the solution to $(4.23) - (4.25)$ can be expanded as the sum

$$A_s(\boldsymbol{r}, t) = \sum_{\nu' \in \Lambda_t} \sum_{l=1}^{m_s} \mathcal{I}^s_{\nu' l} e^{j\nu'\omega_f t} A^l_{is}(\boldsymbol{r}) + \sum_{\nu' \in \Lambda_t} \sum_{\nu \in \Lambda_\theta} \mathcal{D}_{\nu'\nu} e^{j\nu'\omega_f t} \widetilde{A}^\nu_{ds}(\boldsymbol{r}), \tag{4.26}$$

where A^l_{is} for each independent current $l = 1, 2, ..., m_s$ is the solution to the BVP $(3.20) - (3.22)$ and $\widetilde{A}^\nu_{ds}$ for each $\nu \in \Lambda_\theta$ is the solution to the BVP $(3.23) - (3.25)$. Once the solutions to the boundary value problems $(3.20) - (3.22)$ and $(3.23) - (3.25)$ have been found, the radial derivative of the magnetic stream function Γ_{sr} can be expanded as follows:

$$\left.\frac{\partial A_s}{\partial r}\right|_{\Gamma_{sr}} (\theta_s, t) = \sum_{\nu' \in \Lambda_t} e^{j\nu'\omega_f t} \left(\sum_{l=1}^{m_s} \mathcal{I}^s_{\nu' l} \left.\frac{\partial A^l_{is}}{\partial r}\right|_{\Gamma_{sr}} (\theta_s) + \sum_{\nu \in \Lambda_\theta} \mathcal{D}_{\nu'\nu} \left.\frac{\partial \widetilde{A}^\nu_{ds}}{\partial r}\right|_{\Gamma_{sr}} (\theta_s) \right). \tag{4.27}$$

In order to solve the Neumann coefficients from (4.27), let us define an inner product on $t \in [0, 2\pi/\omega_f]$

$$\langle f, g \rangle_t := \frac{\omega_f}{2\pi} \int_0^{2\pi/\omega_f} \widetilde{f}(t) \widetilde{g}(t)^* \, dt. \tag{4.28}$$

Thereafter application of (3.27) with $e^{-j\eta\theta_s}$ and (4.28) with $e^{j\eta'\omega_f t}$ to (4.27) for each $\eta \in \Lambda_\theta$ and $\eta' \in \Lambda_t$, yields

$$\mathcal{N}_{\eta'\eta} = \sum_{\nu' \in \Lambda_t} \sum_{l=1}^{m_s} \mathcal{I}^s_{\eta' l} \left\langle \left\langle e^{j\nu'\omega_f t} \left.\frac{\partial A^l_{is}}{\partial r}\right|_{\Gamma_{sr}}, e^{j\eta'\omega_f t} \right\rangle_t, e^{-j\eta\theta_s} \right\rangle_\theta \tag{4.29}$$

$$+ \sum_{\nu' \in \Lambda_t} \sum_{\nu \in \Lambda_\theta} \mathcal{D}_{\nu'\nu} \left\langle \left\langle e^{j\nu'\omega_f t} \left.\frac{\partial \widetilde{A}^\nu_{ds}}{\partial r}\right|_{\Gamma_{sr}}, e^{j\eta'\omega_f t} \right\rangle_t, e^{-j\eta\theta_s} \right\rangle_\theta$$

$$= \sum_{l=1}^{m_s} F^s_{\eta l} \mathcal{I}^s_{\eta' l} + \sum_{\nu \in \Lambda_\theta} B^s_{\eta\nu} \mathcal{D}_{\eta'\nu}, \tag{4.30}$$

where matrices F^s and B^s are constructed according to (3.29) and (3.30), respectively. Thus, matrices for the frequency-domain spectral Dirichlet-to-Neumann mapping of the stator subproblem are block diagonal and can be written as

$$\left[\mathcal{B}^s\right] = \begin{bmatrix} \mathcal{B}^s_{\eta'_1\nu'_1} & 0 & \dots & 0 \\ 0 & \mathcal{B}^s_{\eta'_2\nu'_2} & \dots & 0 \\ \vdots & \vdots & \ddots & \vdots \\ 0 & 0 & \dots & \mathcal{B}^s_{\eta'_{|\Lambda_t|}\nu'_{|\Lambda_t|}} \end{bmatrix} = \begin{bmatrix} B^s & 0 & \dots & 0 \\ 0 & B^s & \dots & 0 \\ \vdots & \vdots & \ddots & \vdots \\ 0 & 0 & \dots & B^s \end{bmatrix}, \tag{4.31}$$

$$\left[\mathcal{F}^s\right] = \begin{bmatrix} \mathcal{F}^s_{\eta'_1\nu'_1} & 0 & \dots & 0 \\ 0 & \mathcal{F}^s_{\eta'_2\nu'_2} & \dots & 0 \\ \vdots & \vdots & \ddots & \vdots \\ 0 & 0 & \dots & \mathcal{F}^s_{\eta'_{|\Lambda_t|}\nu'_{|\Lambda_t|}} \end{bmatrix} = \begin{bmatrix} F^s & 0 & \dots & 0 \\ 0 & F^s & \dots & 0 \\ \vdots & \vdots & \ddots & \vdots \\ 0 & 0 & \dots & F^s \end{bmatrix}. \tag{4.32}$$

4.3.2 Slip transformations and the rotor subproblem

Construction of a spectral Dirichlet-to-Neumann mapping for the rotor subproblem requires taking into account the relative rotation between the rotor and the stator. If the rotor is locked and passive, the rotor subproblem does not cause additional time-frequencies into the Dirichlet and Neumann data. Then $\mathcal{B}^r$ is also diagonal and the problem (4.20) can be solved one time harmonic at a time.

When the rotor is not locked, the time-frequencies of space harmonics in the Dirichlet data expressed in the rotor and stator coordinate systems are not equal. For example, permeance variation caused by slotting of the stator leads to slot harmonics in the Dirichlet data, which rotate slowly with respect to the stator. However, from the viewpoint of the rotor, the time-frequencies of the stator slot harmonics are typically relatively high.

Just as the rotation of the rotor with respect to a slotted stator leads to new time-frequencies in the rotor fields, rotation of a slotted rotor can lead to new time-frequencies in the Neumann data. The influence of the rotor harmonics to the stator windings is often known as the *secondary armature reaction* [4]. The relationships between the time-frequencies of the fields of different subproblems, the rotor slip and the harmonic indices are governed by slip transformations, which we shall derive here. Equivalent transformations have been previously derived in [43].

First, the Dirichlet data in the rotor coordinate system can be obtained by substitution of (4.9) into (4.6)

$$A_r|_{\Gamma_{sr}}(\theta_r, t) = A_s|_{\Gamma_{sr}}\left(\theta_r + \frac{1-s}{p}\omega_f t, t\right) \tag{4.33}$$

$$= \sum_{(\nu',\nu)\in\Lambda} \mathcal{D}_{\nu'\nu} \exp j\left(s^p_{\nu'\nu}\omega_f t - \nu\theta_r\right), \tag{4.34}$$

where we have defined the *generalized slip*

$$\boxed{s^p_{\nu'\nu} := \nu' - \nu\frac{\omega_s}{\omega_f}\frac{1-s}{p}.} \tag{4.35}$$

The non-zero time-frequencies $s^p_{\nu'\nu}\omega_f$ in the rotor fields are generally integer multiples of the synchronous frequency ω_s only if the rotor slip s is an integer (see Fig. 4.1).

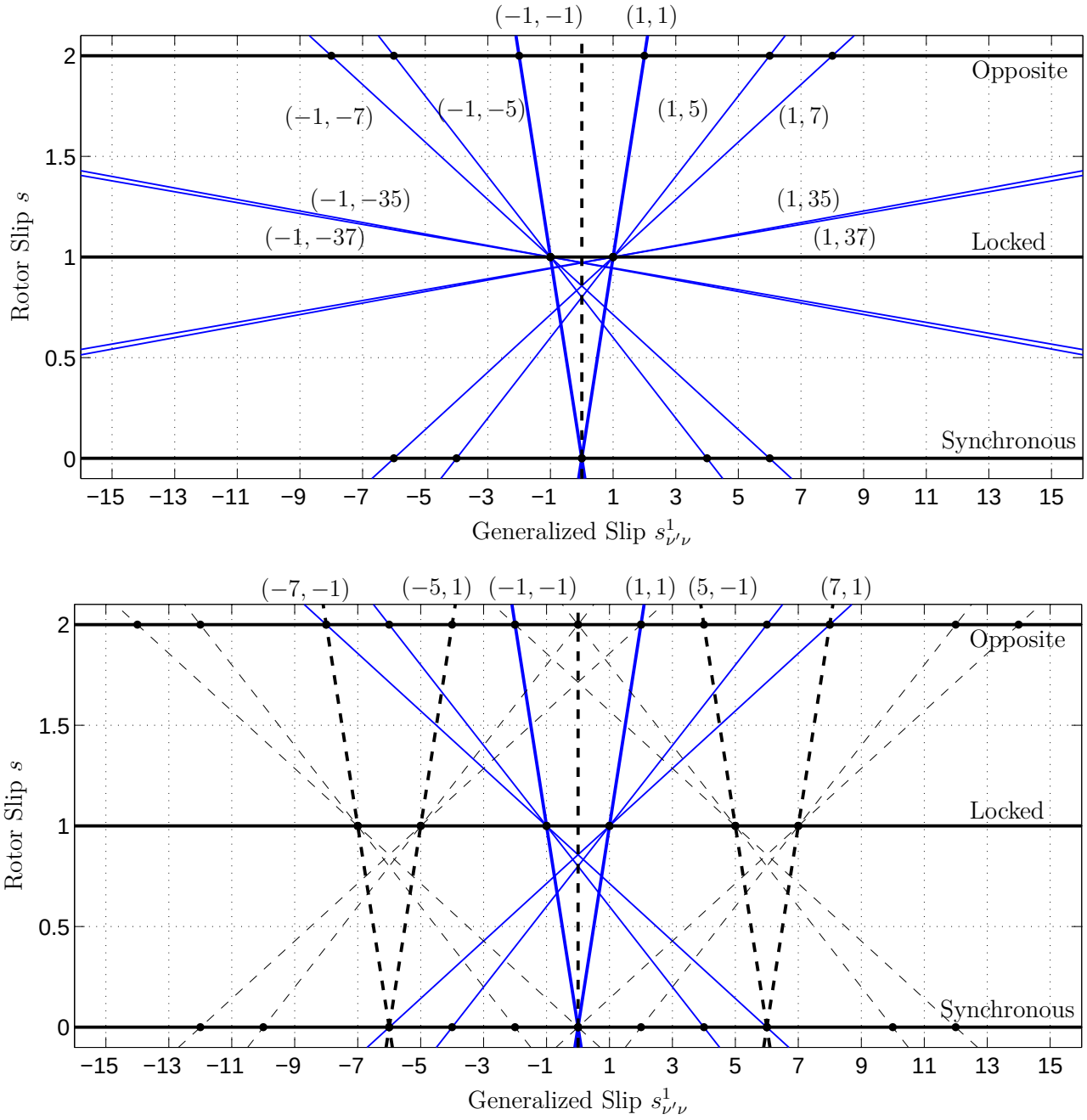

Figure 4.1: Slip transformations for the time-frequencies in the Dirichlet data for some harmonics (ν', ν) when $\omega_f = \omega_s$ and $p = 1$. Change in the time harmonic number ν' corresponds horizontal shift in the generalized slip $s^p_{\nu'\nu}$.

Combination of (4.34) with (4.3) and (4.5) yields a BVP for the rotor region : Find A_r defined in Ω_r such that

$$\begin{aligned} \nabla \cdot \mu^{-1} \nabla A_r &= \sigma \frac{\partial A_r}{\partial t}, && (4.36) \\ A_r|_{\Gamma_{sr}} &= \sum_{(\nu',\nu)\in\Lambda} \mathcal{D}_{\nu'\nu} \exp j\left(s^p_{\nu'\nu}\omega_f t - \nu\theta_r\right), && (4.37) \\ A_r|_{\Gamma_{dr}} &= 0 && (4.38) \end{aligned}$$

hold. Then, by linearity, the solution to (4.36) − (4.38) can be expanded as the sum

$$A_r(\boldsymbol{r},t) = \sum_{(\nu',\nu)\in\Lambda} \mathcal{D}_{\nu'\nu} \exp j\left(s^p_{\nu'\nu}\omega_f t\right) \widetilde{A}_r^{\nu'\nu}(\boldsymbol{r}), \quad (4.39)$$

where $\widetilde{A}_r^{\nu'\nu}$ for each harmonic $(\nu',\nu) \in \Lambda$ is the solution to the BVP

$$\begin{aligned} \nabla \cdot \mu^{-1} \nabla \widetilde{A}_r^{\nu'\nu} &= j s^p_{\nu'\nu} \omega_f \sigma \widetilde{A}_r^{\nu'\nu}, && (4.40) \\ \widetilde{A}_r^{\nu'\nu}\Big|_{\Gamma_{sr}} &= e^{-j\nu\theta_r}, && (4.41) \\ \widetilde{A}_r^{\nu'\nu}\Big|_{\Gamma_{dr}} &= 0. && (4.42) \end{aligned}$$

Thereafter, a truncated Fourier series expansion of the Neumann data with respect to the mechanical angle in the rotor coordinate system can be written as

$$\left.\frac{\partial A_r}{\partial r}\right|_{\Gamma_{sr}} \approx \sum_{(\nu',\nu)\in\Lambda} \mathcal{D}_{\nu'\nu} \sum_{\eta\in\Lambda_\theta} \left\langle \left.\frac{\partial \widetilde{A}_r^{\nu'\nu}}{\partial r}\right|_{\Gamma_{sr}}, e^{-j\eta\theta_r} \right\rangle_\theta \exp j\left(s^p_{\nu'\nu}\omega_f t - \eta\theta_r\right). \quad (4.43)$$

Transformation of (4.43) back to the stator coordinate system by application of (4.7), yield

$$\begin{aligned} \left.\frac{\partial A_s}{\partial r}\right|_{\Gamma_{sr}}(\theta_s,t) &= \left.\frac{\partial A_r}{\partial r}\right|_{\Gamma_{sr}}\left(\theta_s - \frac{1-s}{p}\omega_s t, t\right) && (4.44) \\ &\approx \sum_{(\nu',\nu)\in\Lambda} \mathcal{D}_{\nu'\nu} \sum_{\eta\in\Lambda_\theta} \left\langle \left.\frac{\partial \widetilde{A}_r^{\nu'\nu}}{\partial r}\right|_{\Gamma_{sr}}, e^{-j\eta\theta_r} \right\rangle_\theta \exp j\left(s^p_{\nu'(\nu-\eta)}\omega_f t - \eta\theta_s\right). \end{aligned}$$

Thus, harmonic $(\nu',\nu) \in \Lambda$ in the Dirichlet data (4.9) couples to the time harmonics

$$\boxed{\eta' = s^p_{\nu'(\nu-\eta)} = \nu' - (\nu-\eta)\frac{\omega_s}{\omega_f}\frac{1-s}{p}} \quad (4.45)$$

in the Neumann data (4.10). When $1-s$ is not divisible by the number of pole pairs, Dirichlet data (4.9) may be coupled to such time-frequencies in the Neumann data that are not integer multiples of the synchronous frequency (see Figure 4.2). For such problems, the Dirichlet and the Neumann data (4.9)-(4.10) cannot be expanded accurately with the synchronous frequency as the fundamental frequency. There are two important exceptions to this:

- When the rotor is continuously axisymmetric, the inner product in (4.44) disappears for all $\eta \neq \nu$. Then, the rotor doesn't introduce new time harmonics to the stator fields. Continuously axisymmetric rotors are commonplace in high-speed solid-rotor induction machines.
- When the rotor slip is an integer and the number of rotor slots is divisible by the number of pole pairs, the additional time-frequencies in the stator fields introduced by the rotation of the rotor are always integer multiples of the synchronous frequency. Example modeling scenarios could include modeling no-load or locked-rotor operation of induction machines and steady-state behaviour of synchronous machines.

Open Question 4.1 *In this chapter, the Dirichlet and Neumann data of both the rotor and the stator have been expanded in the stator coordinate system. This technique makes the spectral Dirichlet-to-Neumann mapping for the rotor couple different time-frequencies. If the Dirichlet and Neumann data were expanded in co-moving coordinate systems for the stator and the rotor, no time-frequency coupling would occur in the Dirichlet-to-Neumann mappings. Technically, the matrices $\mathcal{B}^k$ would be block diagonal with separate diagonal block for each time-frequency. Since time-frequencies of space harmonics are dependent on the coordinate system, the two subproblems would be coupled together by the slip transformations induced by* (4.6) − (4.7)*. The transformations can be expressed as matrices and used in a similar way to the rotation matrices in* (3.9) − (3.10)*. What benefits or challenges would such an approach bring?*

4.3.3 Axisymmetric rotor

Axisymmetric non-eccentric rotors with linear material parameters do not produce new time harmonics into the stator Neumann data. The non-zero time harmonics in the Neumann data are exactly those present in the stator winding currents.

The analytical solution[2] $\widetilde{A}_r^{\nu'\nu}$ for multi-layer continuously axisymmetric solid rotors has been presented in the publication 2. For these solutions, the inner product

$$\left\langle \left.\frac{\partial \widetilde{A}_r^{\nu'\nu}}{\partial r}\right|_{\Gamma_{sr}}, \, e^{-j\eta\theta_r} \right\rangle_\theta \tag{4.46}$$

is zero for all $\eta \neq \nu$ and $s^p_{\nu'(\nu-\eta)} = \nu'$ holds. Therefore, (4.44) can be simplified to

$$\left.\frac{\partial A_s}{\partial r}\right|_{\Gamma_{sr}}(\theta_s, t) = \sum_{(\nu',\nu)\in\Lambda} \mathcal{D}_{\nu'\nu} \left\langle \left.\frac{\partial \widetilde{A}_r^{\nu'\nu}}{\partial r}\right|_{\Gamma_{sr}}, \, e^{-j\eta\theta_r} \right\rangle_\theta e^{j(\nu'\omega_s t - \nu\theta_s)}. \tag{4.47}$$

Thus, a spectral Dirichlet-to-Neumann mapping for the rotor subproblem can be written

$$\mathcal{B}^r_{(\eta',\eta),(\nu',\nu)} = \begin{cases} \left\langle \left.\frac{\partial A_r^{\nu'\nu}}{\partial r}\right|_{\Gamma_{sr}}, \, e^{-j\nu\theta_s} \right\rangle_\theta, & (\eta',\eta) = (\nu',\nu) \\ 0 & (\eta',\eta) \neq (\nu',\nu) \end{cases}. \tag{4.48}$$

[2]Note that the notation used for the harmonic indices is different here from the publication 2.

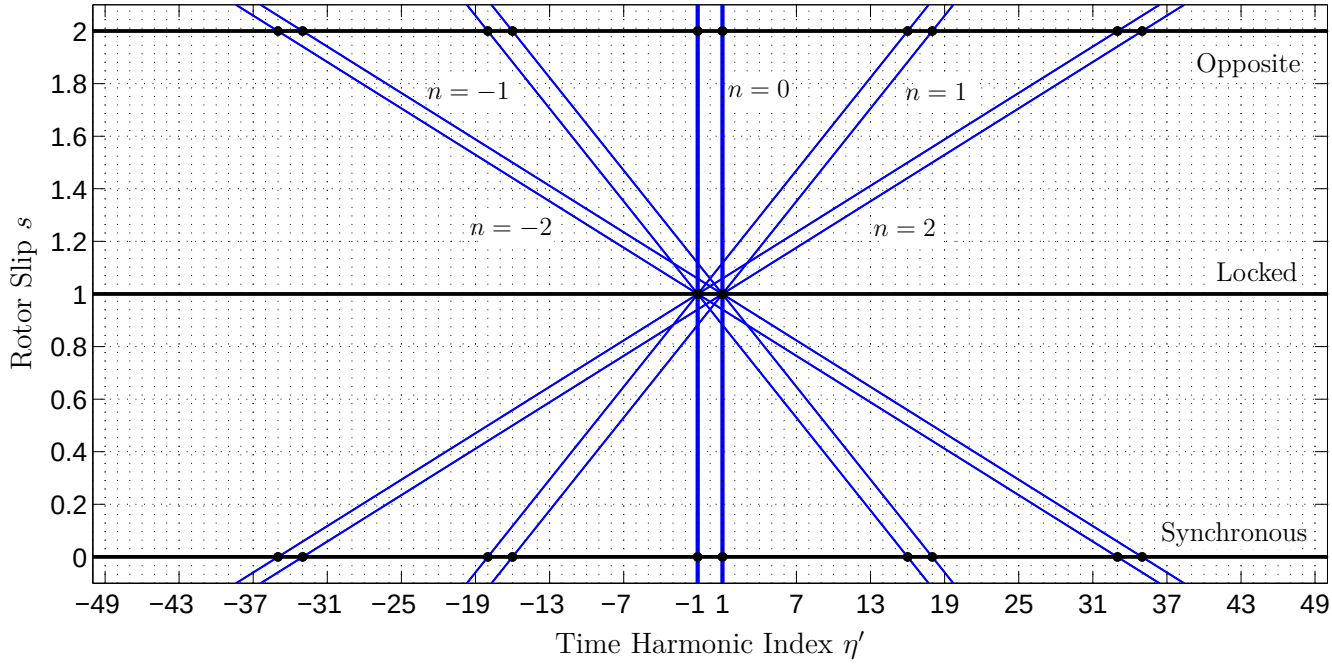

Figure 4.2: Slip transformations for the Neumann data with $\omega_f = \omega_s$, $Q_r = 34$ and $p = 2$.

4.3.4 Slotted rotor

In subsection 3.6.1, it was shown that for slotted geometry with Q_r slots, the inner product for $\widetilde{A}_r^{\nu'\nu}$ in (4.44) is zero unless $\eta = \nu + nQ_r$ holds for some $n \in \mathbb{Z}$. Therefore, (4.44) can be simplified to

$$\begin{aligned} \left.\frac{\partial A_s}{\partial r}\right|_{\Gamma_{sr}}(\theta_s, t) &= \sum_{(\nu',\nu)\in\Lambda} \mathcal{D}_{\nu'\nu} \sum_{n\in\mathbb{Z}} \left\langle \left.\frac{\partial \widetilde{A}_r^{\nu'\nu}}{\partial r}\right|_{\Gamma_{sr}}, e^{-j(\nu+nQ_r)\theta_r} \right\rangle_\theta \\ &\cdot \exp j\left(s^p_{\nu'(-nQ_r)}\omega_f t - (\nu + nQ_r)\theta_s\right). \end{aligned} \tag{4.49}$$

That is, harmonic $(\nu', \nu) \in \Lambda$ in the Dirichlet data (4.9) couples to the harmonics (η', η) in the Neumann data (4.10), for which

$$\begin{bmatrix} \eta' \\ \eta \end{bmatrix} = \begin{bmatrix} \nu' \\ \nu \end{bmatrix} + nQ_r \begin{bmatrix} \frac{\omega_s}{\omega_f}\frac{1-s}{p} \\ 1 \end{bmatrix} \tag{4.50}$$

holds for some $n \in \mathbb{Z}$. The fundamental time-frequency ω_f should be selected such that the time-harmonic index η' is always an integer. For example, if the rotor slip can be expressed as a rational number $s = a/b$ for some $a, b \in \mathbb{Z}$, the selection $\omega_f := \omega_s/(pb)$ yields

$$\eta' = \nu' + nQ_r pb\frac{b-a}{pb} = \nu' + nQ_r(b-a). \tag{4.51}$$

Thus, for arbitrary rational rotor slip $s \in \mathbb{Q}$, there exists a fundamental frequency ω_f so that the Dirichlet data (4.9) is coupled to Neumann data, which can be expressed with (4.10). Then, the rotor subproblem can be reformulated with a spectral Dirichlet-to-Neumann mapping.

Let $\delta : \mathbb{Z} \times \mathbb{Z} \to \{0, 1\}$ be the Kronecker delta. Then, application of inner products (3.27) and (4.28) to (4.44) with $e^{-j\eta\theta_r}$ and $e^{j\eta'\omega_f t}$, respectively, yields

$$\begin{aligned} \mathcal{N}_{\eta'\eta} &= \left\langle \left\langle \left. \frac{\partial A_s}{\partial r} \right|_{\Gamma_{sr}}, e^{-j\eta\theta_r} \right\rangle_\theta, e^{j\eta'\omega_f t} \right\rangle_t \\ &= \sum_{(\nu',\nu)\in\Lambda} \mathcal{D}_{\nu'\nu} \sum_{n\in\mathbb{Z}} \left\langle \left. \frac{\partial A_r^{\nu'\nu}}{\partial r} \right|_{\Gamma_{sr}}, e^{-j(\nu+nQ_r)\theta_r} \right\rangle_\theta \\ &\cdot \quad \delta\left(\eta', \nu' + nQ_r \frac{\omega_s}{\omega_f} \frac{1-s}{p}\right) \delta\left(\eta, \nu + nQ_r\right). \end{aligned} \tag{4.52}$$

Thereafter, the spectral Dirichlet-to-Neumann mapping for the rotor can be constructed:

$$\begin{aligned} \mathcal{B}^r_{(\eta',\eta)(\nu',\nu)} &= \sum_{n\in\mathbb{Z}} \left\langle \left. \frac{\partial A_r^{\nu'\nu}}{\partial r} \right|_{\Gamma_{sr}}, e^{-j(\nu+nQ_r)\theta_r} \right\rangle_\theta \\ &\cdot \quad \delta\left(\eta', \nu' + nQ_r \frac{\omega_s}{\omega_f} \frac{1-s}{p}\right) \delta\left(\eta, \nu + nQ_r\right). \end{aligned} \tag{4.53}$$

4.4 Sparsity patterns and harmonics

In this section, we expain how the sparsity pattern for the matrix $(\mathcal{B}^r - \mathcal{B}^s)$ predicts the non-zero harmonics in the Dirichlet and Neumann data. This information can be then used in the truncation of the harmonics.

In the following discussion, we assume that the fundamental frequency ω_f has been selected such that

$$\Delta' := Q_r \frac{\omega_s}{\omega_f} \frac{1-s}{p} \tag{4.54}$$

is an integer. Then, (4.50) transforms any integer ν' to an integer η'.

4.4.1 Time harmonics

Sparsity pattern of the matrix $(\mathcal{B}^r - \mathcal{B}^s)$ expressed in the block form according to the time harmonic indices can be used to predict the non-zero time-frequencies in the Dirichlet and the Neumann data. When (4.20) is expressed in the block form, the row η' can be written

$$\sum_{n\in\mathbb{Z}} \left[\mathcal{B}^r\right]_{\eta'(\eta'+n\Delta')} \boldsymbol{\mathcal{D}}^r_{\eta'+n\Delta'} - \left[B^s\right] \boldsymbol{\mathcal{D}}_{\eta'} = \left[F^s\right] \boldsymbol{\mathcal{I}}_{\eta'}. \tag{4.55}$$

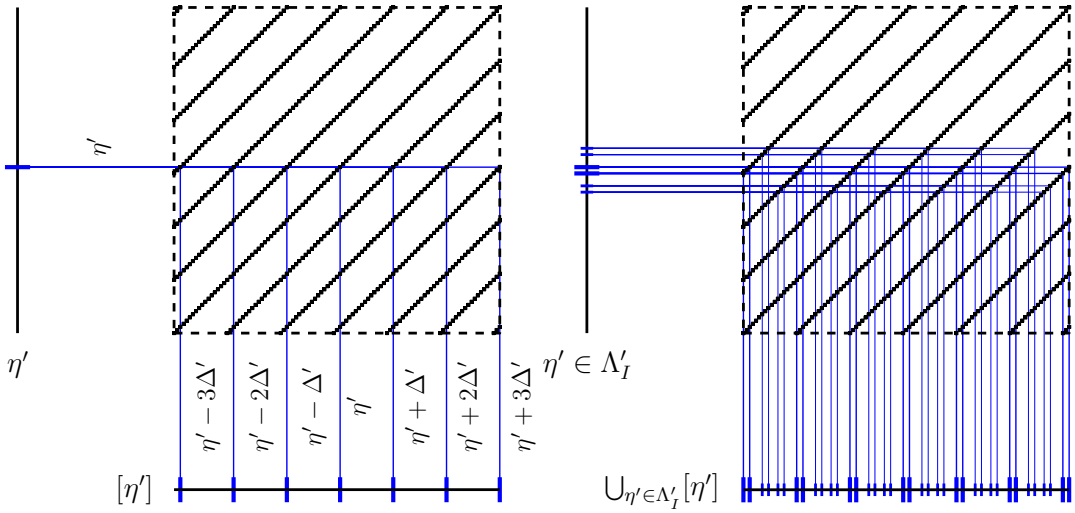

Figure 4.3: Equivalence classes of time harmonics η' in the stator winding currents. Inside the dashed line, sparsity pattern for the matrix $(\mathcal{B}^r - \mathcal{B}^s)$ is shown in terms of blocks.

Therefore, each non-zero time harmonic η' in the stator winding currents $\boldsymbol{\mathcal{I}}$ is coupled to time harmonics

$$[\eta'] \;:=\; \{\eta' + n\Delta' \;:\; n \in \mathbb{Z}\} \tag{4.56}$$

in the Dirichlet data. If Λ'_I is the set of the non-zero time harmonics in the stator winding currents, the non-zero time harmonics in the Dirichlet data can be predicted:

$$\Lambda_t \;\subseteq\; \bigcup_{\eta' \in \Lambda'_I} [\eta']. \tag{4.57}$$

The equivalence classes $[\eta']$ and the selection of the set Λ_t according to (4.57) are visualized in Figure 4.3.

4.4.2 Space harmonics

Expansion of the row (η', η) of (4.20), yields

$$\sum_{(\nu',\nu)\in\Lambda} \left[\mathcal{B}^r\right]_{(\eta',\eta)(\nu',\nu)} \mathcal{D}_{\nu'\nu} - \sum_{\nu\in\Lambda_\theta} \left[B^s\right]_{\eta\nu} \mathcal{D}_{\eta'\nu} = \sum_{l=1}^{m_s} \left[F^s\right]_{\eta l} \mathcal{I}^s_{\eta' l}. \tag{4.58}$$

We again expand the space harmonics in the slot winding currents as a Fourier series with respect to time

$$O^s_\gamma \;=\; \sum_{\eta'\in\Lambda_t} O^s_{\eta'\gamma} e^{j\eta'\omega_f t}, \tag{4.59}$$

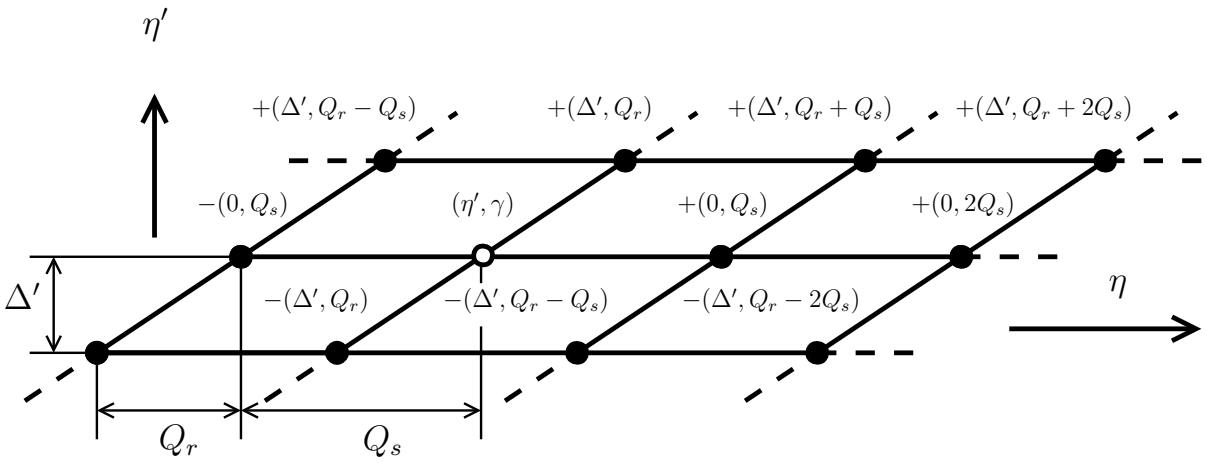

Figure 4.4: Equivalence class of the harmonic (η', γ) in the slot winding currents.

where $O_{\eta'\gamma} \in \mathbb{C}$ holds. Then, an expression for the current in the slot q can be obtained by substitution of (4.59) back to (3.120)

$$I_q^s = \frac{1}{Q_s} \sum_{\gamma=-Q_s/2}^{Q_s/2-1} \sum_{\eta' \in \Lambda_t} O_{\eta'\gamma} \exp j \left(\eta' \omega_s t - \frac{2\pi\gamma q}{Q_s} \right). \tag{4.60}$$

Different terms in the series expansion (4.60) are called *harmonics in the slot winding currents* and are indexed with pairs (η', γ).

Application of the sparsity pattern in (4.53) and the Fourier series expansion (4.59) of the slot winding currents to (4.58), yields

$$\begin{aligned} \sum_{n\in\mathbb{Z}} \left[\mathcal{B}^r\right]_{(\eta',\eta)(\eta'+n\Delta',\eta+nQ_r)} \mathcal{D}_{(\eta'+n\Delta',\eta+nQ_r)} &- \sum_{n\in\mathbb{Z}} \left[B^s\right]_{\eta(\eta+nQ_s)} \mathcal{D}_{\eta'(\eta+nQ_s)} \\ &= \sum_{\gamma} \left[F^s \zeta^s\right]_{\eta\gamma} O^s_{\eta'\gamma}. \end{aligned} \tag{4.61}$$

Thus, each non-zero harmonic (η', γ) in the stator slot winding currents is coupled to the harmonics

$$[(\eta', \gamma)] := \{(\eta' + n_1\Delta', \gamma + n_1 Q_r + n_2 Q_s) \,:\, n_1, n_2 \in \mathbb{Z}\} \tag{4.62}$$

in the Dirichlet data. Each equivalence class of interdependent harmonics forms a lattice of harmonics in $\mathbb{Z}^2$ (see Figure 4.4).

Let Λ_I be the set of non-zero harmonics (η', γ) in the stator slot winding currents. Then, the non-zero harmonics in the Dirichlet data can be limited to

$$\Lambda \subseteq \bigcup_{(\eta',\gamma)\in\Lambda_I} [(\eta', \gamma)]. \tag{4.63}$$

Open Question 4.2 *The symmetry arguments developed here and in section 3.6 do not hold when the rotor is eccentric. The variation introduced to the air gap permeance leads to additional harmonics in the Dirichlet and Neumann data. Can* (4.63) *be generalized to include harmonics due to eccentricity of the rotor?*

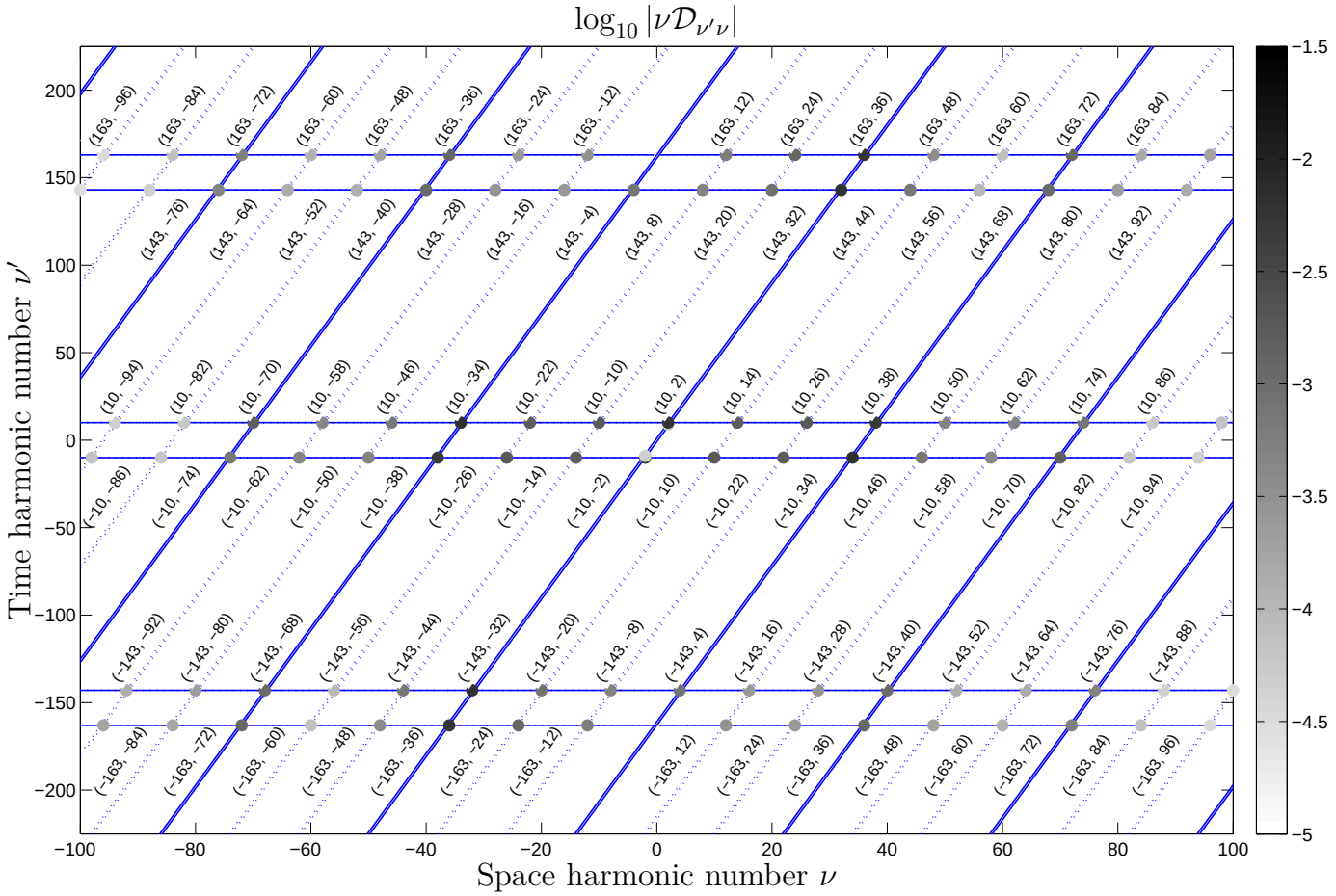

Figure 4.5: Dirichlet data computed from a time-domain solution and predicted by (4.63) for the induction motor of example 1. Colored circles are drawn only for values within the displayed range.

Open Question 4.3 *The prediction of non-zero harmonics by* (4.63) *assumes linear material relations. Can* (4.63) *be generalized to include harmonics due to saturation?*

Example 1 *Consider a 4-pole squirrel-cage induction machine with* $Q_s = 36$ *stator slots and* $Q_r = 34$ *rotor slots driven with balanced 3-phase* 50 *Hz currents in integral-slot windings at rotor slip* $s = 0.1$ *(For further details, see first test case in publication 4).*

Selection $\omega_f = \omega_s/10$*, yields*

$$\Delta' \quad = \quad Q_r \frac{\omega_s}{\omega_f} \frac{1-s}{p} = 34 \cdot 10 \frac{0.9}{2} = 153 \in \mathbb{Z}. \tag{4.64}$$

From (4.62)*, it follows that each non-zero harmonic* $(\eta', \gamma) \in \Lambda_I$ *in the stator slot winding currents is coupled to interdependent harmonics*

$$[(\eta', \gamma)] \quad = \quad \{(\eta' + 153n_1, \gamma + 34n_1 + 36n_2) \ : \ n_1, n_2 \in \mathbb{Z}\} \tag{4.65}$$

in the Dirichlet data. The set of non-zero time-frequencies present in the stator fields can be predicted from (4.57) *to be*

$$\left\{(n\Delta' \pm 10)\frac{\omega_f}{2\pi} : n \in \mathbb{Z}\right\} \quad = \quad \{(765n \pm 50)\ Hz : n \in \mathbb{Z}\} \tag{4.66}$$

From (3.125)*, it follows that we are to include the harmonics*

$$\Lambda_I \quad = \quad \{(10,2),\ (10,14),\ (10,-10),\ (-10,-2),\ (-10,-14),\ (-10,10)\} \tag{4.67}$$

in the stator slot winding currents. The harmonics predicted by (4.63) *and obtained by the code used in the publication 4 are shown in Figure 4.5.*

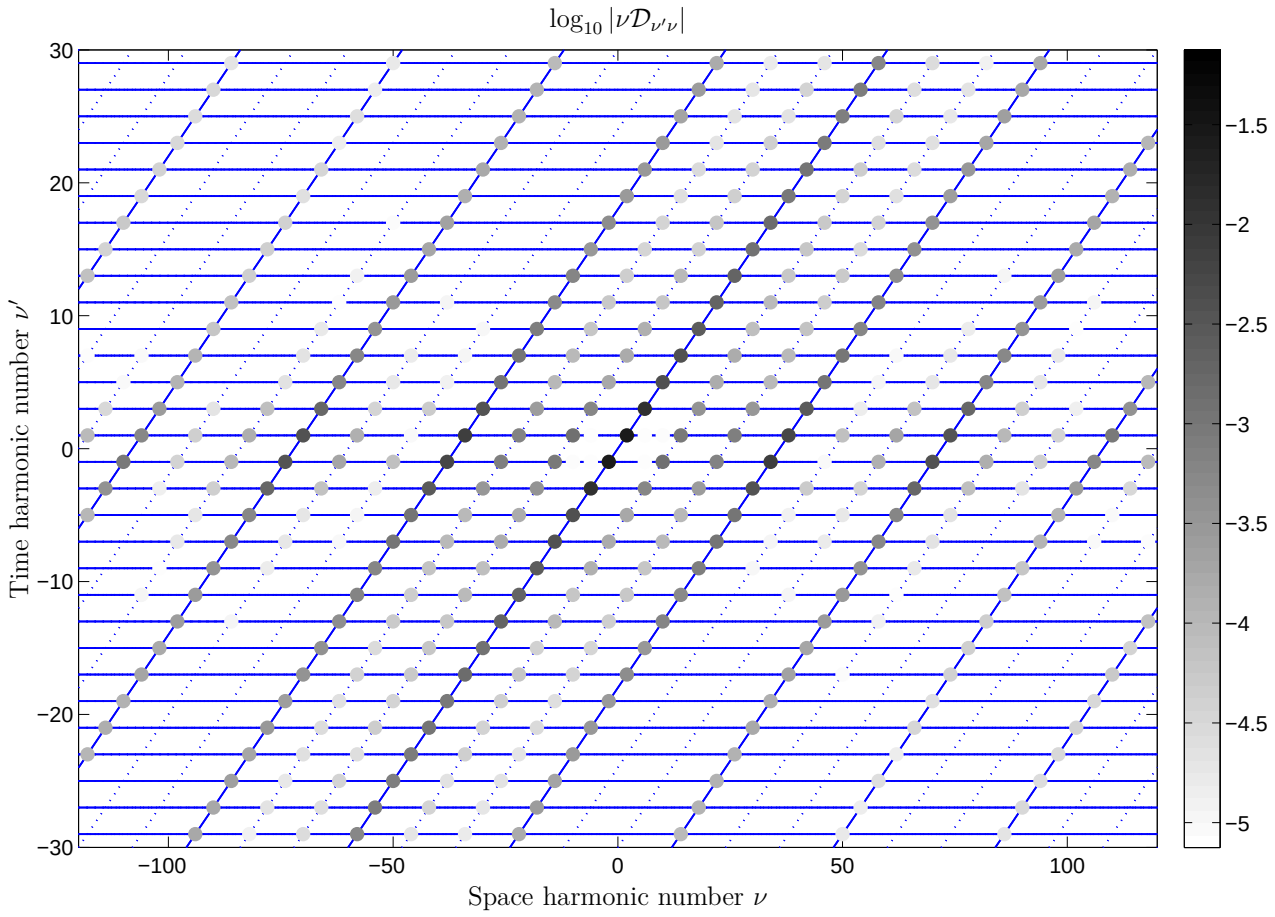

Figure 4.6: Dirichlet data computed from a time-domain solution and predicted by (4.63) for the synchronous reluctance machine of example 2. Colored circles are drawn only for values within the displayed range.

Example 2 *Consider a 4-pole synchronous reluctance machine with* $Q_s = 36$ *stator slots and* $Q_r = 4$ *salient rotor poles driven with balanced 3-phase* 50 *Hz currents in*

integral-slot windings (For further details, see second test case in publication 4). Selection of $\omega_f = \omega_s$*, yields*

$$\Delta' \quad = \quad \frac{Q_r}{p} = 2. \tag{4.68}$$

Thus, the set of non-zero time-frequencies present in the stator fields can be predicted from (4.57) *to be*

$$\left\{(n\Delta' \pm 1)\frac{\omega_s}{2\pi} : n \in \mathbb{Z}\right\} \quad = \quad \{(100n \pm 50)\ Hz : n \in \mathbb{Z}\} \tag{4.69}$$

From (3.125)*, it follows that we are to include the harmonics*

$$\Lambda_I \quad = \quad \{(1,2),\ (1,14),\ (1,-10),\ (-1,-2),\ (-1,-14),\ (-1,10)\} \tag{4.70}$$

in the stator slot winding currents. The harmonics predicted by (4.63) *and obtained by time-domain solution with the code used in the publication 4 are shown in Figure 4.6.*

Chapter 5

Metric and motion

In chapter 3, the rotor and stator subproblems were coupled at an interface at the center of the air gap by interface conditions $(3.9)-(3.10)$ for the Dirichlet and Neumann coefficients. More commonly in time-domain FE models for rotating electrical machines, the FE models for the rotor and the stator subproblems are coupled by a layer of elements in the air gap, which is deformed with time to conform to the movement of the rotor. Once the deformation exceeds the measure of a single element in the layer, the connections between the nodes of the layer are changed [26]. In this chapter, we present a related approach for modeling relative movement but without changes to the coordinates of the mesh nodes in the corresponding FE models. To achieve this, we use a time-parametrized family of coordinate systems such that the coordinates of the material points of the moving bodies are time-independent. Then, the relative movement can be taken into account by changing the material parameters in the air gap with time.

To express the derived BVP in an arbitrary coordinate system, we need a sufficient mathematical framework for modeling space. The framework of differential forms on Riemannian manifolds makes Maxwell's equations and material relations expressible without reference to any coordinate system. Riemannian geometry allows coordinate-independent formulation of electrodynamics and provides tools for transforming BVPs between arbitrary coordinate systems.

On the other hand, quantitative representations of geometries and fields require coordinate systems. Once a BVP has been formulated in one coordinate system with a known expression for the metric tensor, the BVP can be transformed into an arbitrary coordinate system for solution. In problems involving movement of objects, this allows the selection of a family of coordinate system transformations so that the coordinates of the material points do not change upon a time evolution of the modelled system.

5.1 Model of space and movement

In order to construct a BVP modeling any electromechanical device, some model of space is needed. Euclidean spaces provide a sufficient model in most BVPs arising from classical electrodynamics and as an example of a Riemannian manifold make possible

the application of the tools from Riemannian geometry.

Relative movement and deformation of objects is change of distances between material points with time. On a Riemannian manifold, changes in distances can be described by both change in the metric tensor and by changes in the identification between material points and the points of the manifold. The latter is a modeling decision that is visible in mathematics only through its consequences. However, two different decisions can be related by a map between manifolds. If points of the manifold are fixed to the material points of the moving bodies, the desription is known as a *Lagrangian description of movement*. In *Eulerian descriptions of movement* the points of the manifold are fixed to some ambient space.

Since we wish to give material points fixed coordinates, the choice of the description influences the choice of the coordinate systems. When a Lagrangian description of movement is used, a single coordinate system can be fixed to the material bodies and movement corresponds to a change in the metric of the manifold [44]. In Eulerian descriptions, a time-parametrized family of coordinate systems is selected so that the coordinates given to material points stay fixed with time. Movement then corresponds to a change with time in the coordinate representation of the fixed metric of the manifold.

We will apply a Eulerian description of movement on the Riemannian manifold formed by the Euclidean space. We use a time-parametrized family of coordinate charts fixed to the material points. In terms of coordinates, this yields a description equivalent to a Lagrangian description with a fixed coordinate chart.

5.1.1 Euclidean space

A *n-dimensional affine space* is a triplet (M^n, D^n, τ), where M^n is a set, D^n is n-dimensional real vector space and $\tau : M^n \times D^n \to M^n$ is a mapping such that the conditions

1. for all $x \in M^n$, $\tau(x, 0) = x$,
2. for all $v, w \in D^n$ and $x \in M^n$, $\tau(\tau(x, v), w) = \tau(x, v + w)$,
3. for all $x \in M$ $\tau(x, \cdot) : D^n \to M^n$ is a bijection

hold. We call D^n the *displacement space* and τ the *displacement mapping* of M^n. The point $\tau(x, v)$ is denoted by $x + v$ and the unique vector $v \in D^n$ for which $\tau(x, v) = y$ holds is denoted by $y - x$.

An *n-dimensional Euclidean space* (E^n, g_E) is an n-dimensional affine space E^n together with an *inner product* $g_E : D^n \times D^n \to \mathbb{R}$ for the displacement space D^n of E^n. Selection of an inner product for D^n corresponds to a selection of a basis for D^n: Let $e_1, e_2, ..., e_n$ be a basis for D^n. Then, a canonical Euclidean inner product can be chosen

$$g_E(e_i, e_j) \quad := \quad \delta_{ij}, \tag{5.1}$$

where δ_{ij} is the Kronecker delta function. Conversely, selection of an inner product for D^n induces a basis for D^n such that (5.1) holds.

Then (5.1) induces a *distance metric* for E^n

$$d_E : E^n \times E^n \to [0, \infty) \quad : \quad d_E(x, y) := \sqrt{g_E(x - y,\ x - y)} \tag{5.2}$$

such that for all $x, y \in E^n$ and $v \in D^n$

$$d_E(x, y) = d_E(x + v, y + v) \tag{5.3}$$

holds. We will use the unique *norm topology* induced by the distance metric (5.2) on E^n [38].

Coordinate chart on E^n with the norm topology is pair $(U_\alpha, \varphi_\alpha)$, where $\varphi_\alpha : U_\alpha \to \mathbb{R}^n$ is a homeomorphism of the open subset U_α of E^n to an open subset $\varphi_\alpha(U_\alpha)$ of $\mathbb{R}^n$. Since E^n is an affine space and for every $x_0 \in E^n$, $\tau(x_0, \cdot) : D^n \to E^n$ is a bijection, selection of an origin point $x_0 \in E^n$ and a basis for D^n corresponds to a global coordinate chart for E^n.

In order to carry out analysis in different coordinate systems, the coordinate charts need to cover E^n and the transitions between coordinate systems need to be smooth enough. These notions are formalized in manifold theory into concepts of atlases and differentiable structures.

An *atlas for* E^n is a collection of charts $\{(U_\alpha, \varphi_\alpha)\}_\alpha$ such that the union of the domains $\bigcup_\alpha U_\alpha$ cover E^n. For E^n and arbitrary $x_0 \in E^n$, $\{\tau(x_0, \cdot)\}$ constitutes a single-chart atlas. An atlas on E^n is a *C^k-differentiable structure* for E^n such that

1. for any two charts (U_i, φ_i) and (U_j, φ_j) of the atlas the *transition map*

$$(\varphi_j \circ \varphi_i^{-1}) : \varphi_i(U_i \cap U_j) \to \varphi_j(U_i \cap U_j) \tag{5.4}$$

   is k times continuously differentiable. Such charts are called *C^k-compatible.*

2. the atlas is *maximal* in the sense that if there is a chart (U, φ) C^k compatible with every chart in the atlas, (U, φ) must be in the atlas.

E^n together with an C^k-differentiable structure is an example of a *differentiable manifold* of class C^k.

5.1.2 Tangent and cotangent spaces

Let $T_p(E^n)$ and $T_p^*(E^n)$ be the tangent and cotangent spaces of the point $p \in E^n$, respectively [14, 15]. Each chart $(U_\alpha, \varphi_\alpha)$ induces bases for the tangent and cotangent spaces T_pE^n and $T_p^*E^n$, respectively at each point $p \in U_\alpha$: Let $(\boldsymbol{e}_1, \ldots, \boldsymbol{e}_n)$ be the standard basis for $\mathbb{R}^n$. Then, the basis $(\partial_1^\alpha, \ldots, \partial_n^\alpha)$ corresponding to the chart $(U_\alpha, \varphi_\alpha)$ for the tangent space T_pE^n consists of the equivalence classes of the curves [14, 15, 45]

$$\gamma_k : \mathbb{R} \to E^n \quad : \quad t \mapsto \varphi_\alpha^{-1}(\varphi_\alpha(p) + t\boldsymbol{e}_k) \tag{5.5}$$

for each $k = 1, ..., n$. The corresponding basis $(dx_\alpha^1, \ldots, dx_\alpha^n)$ for the cotangent space $T_p^*E^n$ is determined by the relation

$$dx_\alpha^i(\partial_j^\alpha) \quad = \quad \delta_{ij}. \tag{5.6}$$

Let $(U_\alpha, \varphi_\alpha)$ and (U_β, φ_β) be two charts, $p \in U_\alpha \cap U_\beta$ and J be the Jacobian for the transition map $\varphi_\beta \circ \varphi_\alpha^{-1}$ and $v \in T_pE^n, \omega \in T_p^*E^n$. Then, v and ω can always be expanded as

$$v = \sum_{k=1}^{n} v_\alpha^k \partial_k^\alpha = \sum_{k=1}^{n} v_\beta^k \partial_k^\beta, \tag{5.7}$$

$$\omega = \sum_{k=1}^{n} \omega_k^\alpha dx_\alpha^k = \sum_{k=1}^{n} \omega_k^\beta dx_\beta^k, \tag{5.8}$$

where the coefficients are related by

$$v_\beta^i = \sum_{j=1}^{n} J_{ij} v_\alpha^j \quad \Leftrightarrow \quad \boldsymbol{v}_\beta = \Big[J\Big] \boldsymbol{v}_\alpha, \tag{5.9}$$

$$\omega_i^\beta = \sum_{j=1}^{n} J_{ji}^{-1} \omega_j^\alpha \quad \Leftrightarrow \quad \boldsymbol{\omega}^\beta = \Big[J^{-T}\Big] \boldsymbol{\omega}^\alpha. \tag{5.10}$$

The equations $(5.9) - (5.10)$ are known as *contravariant and covariant transformation*, respectively [15].

5.1.3 Riemannian metric and distance

The Euclidean space E^n together with an inner product

$$g_p : T_pE^n \times T_pE^n \to \mathbb{R} \tag{5.11}$$

for all tangent spaces $T_pE^n : p \in E^n$ that varies smoothly from point to point is an example of a Riemannian manifold [14, 15, 45].

The Euclidean metric $g_E : D^n \times D^n \to \mathbb{R}$ induces a metric tensor g_p for E_n: Let $(u_1, \ldots, u_n)$ be a basis for the displacement space D^n of E^n. Then, the curves through $p \in E^n$

$$\gamma_k : \mathbb{R} \to E^n \quad : \quad t \mapsto \tau(p, tu_k) \tag{5.12}$$

for $k = 1, ..., n$ determine a basis $(\partial_1^\alpha, \ldots, \partial_n^\alpha)$ for T_pE^n. A metric compatible with the inner product g_E of E^n can be selected by requiring at each point $p \in E^n$ that

$$g_p(\partial_i^\alpha, \partial_j^\alpha) = g_E(u_i, u_j) \tag{5.13}$$

holds for all $i, j = 1, .., n$. For any $p \in E^n$, the curves (5.12) also induce a global coordinate chart, which in turn induces the metric (5.13).

The metric g_p at each point $p \in E^n$ and an arbitrary chart $(U_\alpha, \varphi_\alpha)$ is represented by the matrix $G^\alpha(p) \in \mathbb{R}^{n \times n}$, whose elements are defined so that

$$G_{ij}^\alpha(p) := g_p(\partial_i^\alpha, \partial_j^\alpha) \tag{5.14}$$

holds for all $i, j = 1, .., n$.

The expansions of the metric g_p of E^n in cobases induced by different charts must be equal: Let $(U_\alpha, \varphi_\alpha)$ and (U_β, φ_β) be two charts, $p \in U_\alpha \cap U_\beta$ hold and J the Jacobian for the transition map $\varphi_\beta \circ \varphi_\alpha^{-1}$. Then,

$$g_p(v,w) \;=\; \sum_{i=1}^{n}\sum_{j=1}^{n} G^\alpha_{ij}(p)dx^i_\alpha(v)dx^j_\alpha(w) = \sum_{i=1}^{n}\sum_{j=1}^{n} G^\beta_{ij}(p)dx^i_\beta(v)dx^j_\beta(w) \qquad (5.15)$$

must hold for all $v, w \in T_pE^n$. Substitution of the basis vectors for the tangent space T_pE^n and application of coordinate transformations (5.9) for the tangent vectors yield

$$\left[G^\beta(p)\right] \;=\; \left[J^{-T}G^\alpha(p)J^{-1}\right]. \qquad (5.16)$$

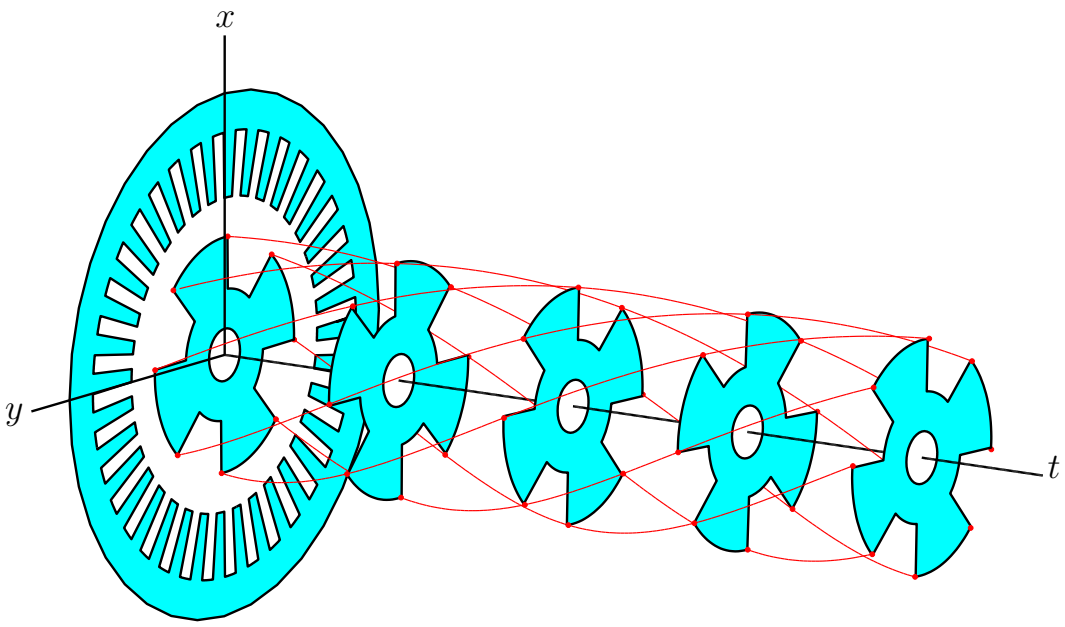

Figure 5.1: Curves $X_t(p)$ for the corner points p of a rotating rotor.

5.1.4 Eulerian description of movement

Let $X_t : E^n \times \mathbb{R} \to E^n$ be a time-parameterized family of diffeomorphisms describing the movement and deformation of objects in E^n with time. That is, each material point is mapped from their initial position at some moment in time t_0 to their location at the moment in time t (see Figure 5.1). Within air regions, the mapping can be chosen arbitrarily. We call such a mapping a *placement map* [44].

If a placement map exists, we will select a global chart (E^n, φ_g) and use the family of charts $\{(E^n, \psi_t)\}_{t\in\mathbb{R}}$ defined by

$$\psi_t \;:=\; \varphi_g \circ X_t^{-1} \qquad (5.17)$$

that associate to each material point fixed coordinates. Relative movement then corresponds to change with time in the representation (5.16) of the metric tensor g.

5.2 Formulations

To formulate BVPs in E_n arising from electromechanical devices, we need a model for the relevant electromagnetic phenomena. An appropriate model in E_3 for most electromechanical devices is provided by the magnetoquasistatic approximation of electrodynamics [22, 46, 47]. We will use a coordinate-independent formulation of magnetoquasistatics expressed in terms of differential forms [44]. The model of magnetoquasistatics is reduced to two dimensions by exploitation of the approximate translational invariance of fields present in many electromechanical devices. Then, we will explain how two-dimensional BVPs can be derived with the magnetic stream function.

5.2.1 Eulerian formulation of magnetoquasistatics

Let $\mathcal{F}^k(E^n)$ be the space of k-forms in E^n, $d : \mathcal{F}^k(E^n) \to \mathcal{F}^{k+1}(E^n)$ the *exterior derivative operator* and $\star : \mathcal{F}^k(E^n) \to \mathcal{F}^{n-k}(E^n)$ the *Hodge star operator* corresponding to the metric tensor of E^n, [14, 15].

With differential forms, magnetoquasistatic Maxwell's equations in E^3 can be written as: [44]

$$dH = J, \tag{5.18}$$

$$dE = -\frac{\partial}{\partial t}B, \tag{5.19}$$

where $H \in \mathcal{F}^1(E^3)$ is the magnetic field strength 1-form, $B \in \mathcal{F}^2(E^3)$ the magnetic flux 2-form, $J \in \mathcal{F}^2(E^3)$ the current density 2-form and $E \in \mathcal{F}^1(E^3)$ the electric field 1-form.

Since the points of the manifold are not fixed to the material bodies, the more common form of the Ohm's law is replaced by the *Ohm's law for moving bodies* [47, 48]. In terms of differential forms, this corresponds to an additional term, which is the contraction of the magnetic flux 2-form B with the velocity vector field V corresponding to the placement map X_t. The *contraction* of a k-form $\omega \in \mathcal{F}^k(\Omega)$ with the vector field V is the $k-1$-form $i_V\omega$ such that

$$(i_V\omega)(p)(v_1, ..., v_{k-1}) = \omega(p)(V, v_1, ..., v_{k-1}) \tag{5.20}$$

holds for all $p \in \Omega$ and $v_1, ..., v_{k-1} \in T_p(\Omega)$ [14].

Then, material relations can be expressed [44]

$$B = \mu \star H, \tag{5.21}$$

$$J = \sigma \star (E - i_V B) + J^s, \tag{5.22}$$

where $J^s \in \mathcal{F}^2(E^3)$ is the source current density 2-form.

In coordinate descriptions co-moving with the material bodies, the convective term in (5.22) disappears. We will demonstrate this in section 5.3 for a two-dimensional FE formulation. However, for completeness, the term is included in the subsequent derivations.

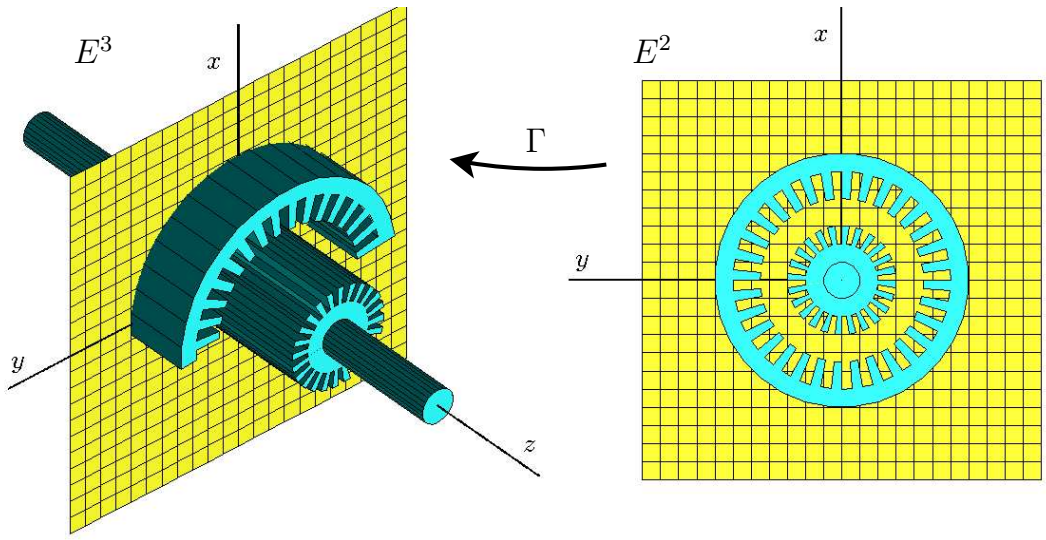

Figure 5.2: Inclusion map Γ. The air gap width is exaggerated.

5.2.2 Translational symmetry

In order to reduce the problem to two dimensions, we approximate that the fields are invariant with respect to some geometric transformation. Once the reduced-dimension problem has been solved, the invariance can be used to construct an approximate solution to the original problem. In the case of rotating electrical machines, continuous translational symmetry in the axial direction is typically assumed within the active area. However, due to finite length of the machine, translational symmetry holds only approximately and is often an especially poor approximation for the fields near the end of the active area [49].

In addition to translational invariance, we assume that the magnetic flux has no component in the axial direction and that the current density is purely axial. Let (E^2, ψ_2) and (E^3, ψ_3) be global charts in terms of Cartesian coordinates with the z-axis fixed along the axis of the machine (see Figure 5.2). Let us define an inclusion mapping

$$\Gamma : E^2 \to E^3 : \psi_3 \circ \Gamma \circ \psi_2^{-1} \quad = \quad (x, y) \mapsto (x, y, 0). \tag{5.23}$$

Define forms in E^2

$$\begin{aligned} b &:= -\Gamma^* i_{\partial_z^3} B, && (5.24)\\ e &:= -\Gamma^* i_{\partial_z^3} E, && (5.25)\\ h &:= \Gamma^* H, && (5.26)\\ j &:= \Gamma^* J. && (5.27) \end{aligned}$$

The magnetic flux 2-form B in E^3 and the magnetic flux 1-form b in E^2 can be expanded

with respect to the charts (E^3, ψ_3) and (E^2, ψ_2), respectively

$$B = B_x dy_3 \wedge dz_3 + B_y dz_3 \wedge dx_3, \tag{5.28}$$
$$b = b_x dx_2 + b_y dy_2. \tag{5.29}$$

Then, combination of (5.24) with (5.28) – (5.29), yields

$$b_x = -(\Gamma^* i_{\partial_z^3} B)(\partial_x^2) = -B(\partial_z^3, \Gamma_* \partial_x^2) = -B(\partial_z^3, \partial_x^3) = -B_y, \tag{5.30}$$
$$b_y = -(\Gamma^* i_{\partial_z^3} B)(\partial_y^2) = -B(\partial_z^3, \Gamma_* \partial_y^2) = -B(\partial_z^3, \partial_y^3) = B_x. \tag{5.31}$$

On E^2, Maxwell's equations can be written

$$dh = j, \tag{5.32}$$
$$de = -\frac{\partial}{\partial t} b \tag{5.33}$$

with material relations

$$b = \mu \star h, \tag{5.34}$$
$$j = \sigma \star (e - i_V b) + j^s. \tag{5.35}$$

5.2.3 A formulation

Let us denote by Ω the cross section of the device together with some surroundings, depending on the problem. Let $\partial\Omega$ be the boundary of Ω, $\Omega_c \subset \Omega$ the subregion with conductive materials and $\Omega_s \subset \Omega$ the subregion with source currents.

Let us define a magnetic stream function $a \in \mathcal{F}^0(\Omega)$ such that

$$b = da \tag{5.36}$$

holds with the initial condition $a(0) = 0$. Then, substitution of $e = -(\partial/\partial t)a$, (5.36) and (5.33) – (5.35) to (5.32) yield

$$d(\mu^{-1} \star da) - \sigma \star \left(\frac{\partial}{\partial t} a + i_V da \right) + j^s = 0. \tag{5.37}$$

On $\partial\Omega$, the Dirichlet boundary condition

$$a|_{\partial\Omega} = 0 \tag{5.38}$$

is used. Coupling to external circuits is discussed in publications 1 and 3.

5.3 Finite Element models

The BVP (5.37) – (5.38) is solved in a time-parametrized family of coordinate charts with the Finite Element Method. In this section, we will first derive a weak formulation

for the BVP (5.37) – (5.38). To compute numerical values for the integrals of the weak formulation, we explain how the integrals can be expressed in an arbitrary coordinate chart. Then, time-evolution of the computational chart influences the representation of the material derivative of the magnetic stream function. We will show that when the computational chart is fixed to the material points, the material derivative simplifies to the time derivative.

5.3.1 Weak formulation

Let $\mathcal{F}_0^0(\Omega)$ be the space of test 0-forms with zero trace on the boundary $\partial\Omega$ of Ω. Then, wedge product of (5.37) with an arbitrary $a' \in \mathcal{F}_0^0(\Omega)$, yields

$$\int_\Omega d(\mu^{-1} \star da) \wedge a' - \int_{\Omega_c} \sigma \star \left(\frac{\partial}{\partial t} a + i_V da \right) \wedge a' + \int_{\Omega_s} j^s \wedge a' \;=\; 0 \qquad (5.39)$$

Application of the product rule for the exterior derivative and the Stokes formula yields

$$\begin{aligned} \int_\Omega d(\mu^{-1} \star da) \wedge a' &= \int_\Omega \left(d(\mu^{-1}(\star da) \wedge a') + \mu^{-1} \star da \wedge da' \right) \qquad (5.40) \\ &= \int_\Omega \mu^{-1} \star da \wedge da' + \oint_{\partial\Omega} \mu^{-1} \star da \wedge \underbrace{a'}_{=0 \text{ at } \partial\Omega} \\ &= \int_\Omega \mu^{-1} \star da \wedge da'. \end{aligned}$$

Combination of (5.39) with (5.40) leads to a weak formulation: Find $a \in \mathcal{F}_0^0(\Omega)$ so that

$$\int_\Omega \mu^{-1} \star da \wedge da' \;-\; \int_{\Omega_c} \sigma \star \left(\frac{\partial}{\partial t} a + i_V da \right) \wedge a' + \int_{\Omega_s} j^s \wedge a' = 0 \qquad (5.41)$$

holds for all $a' \in \mathcal{F}_0^0(\Omega)$.

5.3.2 Coordinate charts and integration

To compute numerical values for the integrals in (5.41) for any $a, a' \in \mathcal{F}^0(\Omega)$, the integrals are expressed in some coordinate chart (U_β, φ_β) with the pull-back operator induced by the chart. We call (U_β, φ_β) the *computation chart* and assume for simplicity that the problem domain Ω is contained in the domain U_β of the chart.

Let us denote $\star_\beta := \varphi_\beta^{-1*} \star \varphi_\beta^*$, $a_\beta := \varphi_\beta^{-1*} a = a \circ \varphi_\beta^{-1}$. Then, application of the properties of the pull-back mapping to the first integral in (5.41), yields

$$\begin{aligned} \int_\Omega \mu^{-1} \star da \wedge da' &= \int_{\varphi_\beta(\Omega)} \varphi_\beta^{-1*}(\mu^{-1} \star da \wedge da') \qquad (5.42) \\ &= \int_{\varphi_\beta(\Omega)} \mu_\beta^{-1} (\varphi_\beta^{-1*} \star \varphi_\beta^*) d\varphi_\beta^{-1*} a \wedge d\varphi_\beta^{-1*} a' \\ &= \int_{\varphi_\beta(\Omega)} \mu_\beta^{-1} \star_\beta da_\beta \wedge da'_\beta(\partial_1^\beta, \partial_2^\beta). \end{aligned}$$

The integrand of (5.42) can be expanded[1]

$$\begin{aligned}\mu_\beta^{-1} \star_\beta da_\beta \wedge da'_\beta(\partial_1^\beta, \partial_2^\beta) &= \mu_\beta^{-1} \begin{vmatrix} \star_\beta da_\beta(\partial_1^\beta) & da'_\beta(\partial_1^\beta) \\ \star_\beta da_\beta(\partial_2^\beta) & da'_\beta(\partial_2^\beta) \end{vmatrix} \\ &= \mu_\beta^{-1} \begin{bmatrix} \star_\beta da_\beta(\partial_1^\beta) & \star_\beta da_\beta(\partial_2^\beta) \end{bmatrix} \begin{bmatrix} 0 & 1 \\ -1 & 0 \end{bmatrix} \begin{bmatrix} da'_\beta(\partial_1^\beta) \\ da'_\beta(\partial_2^\beta) \end{bmatrix}\end{aligned} \tag{5.43}$$

The material relations and source currents are often known only in some reference chart $(U_\alpha, \varphi_\alpha)$, which is not always the computation chart. Thus, the material relations and source currents need to be transformed to the computation chart. Whenever $\eta = \star\omega$ holds for all $\omega \in \mathcal{F}^1(\Omega)$, the *matrix representation of the Hodge operator* for 1-forms in the chart β is the matrix $\star^\beta(p) \in \mathbb{R}^{2\times 2}$ that satisfies

$$\boldsymbol{\eta}^\beta = \left[\star^\beta\right] \boldsymbol{\omega}^\beta. \tag{5.44}$$

For E^2, there always exists a global chart (E^2, φ_e) such that the matrix representation (5.14) of the metric tensor of E^2 is the identity matrix. Then, if J is the Jacobian of the transition map to the chart (U_β, φ_β) at $p \in U_\beta$, the matrix representation of the Hodge operator in the chart β can be obtained

$$\left[\star^\beta\right] = \left[J^{-T}\right] \begin{bmatrix} 0 & -1 \\ 1 & 0 \end{bmatrix} \left[J^T\right]. \tag{5.45}$$

Let us denote the *gradient of a 0-form* with respect to the coordinates of the chart (U_β, φ_β) by

$$\nabla a_\beta := \begin{bmatrix} da_\beta(\partial_1^\beta) \\ da_\beta(\partial_2^\beta) \end{bmatrix} = \begin{bmatrix} \frac{\partial a}{\partial x_1^\beta} \\ \frac{\partial a}{\partial x_2^\beta} \end{bmatrix}. \tag{5.46}$$

Then, substitution of (5.45) to (5.43), yields[2]

$$\begin{aligned}\mu_\beta^{-1} \star_\beta da_\beta \wedge da'_\beta(\partial_1^\beta, \partial_2^\beta) &= \mu_\beta^{-1} \nabla a_\beta^T \left[\star^\beta\right]^T \begin{bmatrix} 0 & -1 \\ 1 & 0 \end{bmatrix} \nabla a'_\beta \\ &= -\mu_\beta^{-1} \nabla a_\beta^T \left[J\right] \begin{bmatrix} 0 & -1 \\ 1 & 0 \end{bmatrix} \left[J^{-1}\right] \begin{bmatrix} 0 & -1 \\ 1 & 0 \end{bmatrix} \nabla a'_\beta \\ &= -\mu_\beta^{-1} \frac{1}{\det J} \nabla a_\beta^T J J^T \nabla a'_\beta.\end{aligned} \tag{5.47}$$

[1] For two arbitrary vectors $\boldsymbol{a}, \boldsymbol{b} \in \mathbb{R}^2$,

$$\det \begin{bmatrix} \boldsymbol{a} & \boldsymbol{b} \end{bmatrix} = \boldsymbol{a}^T \begin{bmatrix} 0 & 1 \\ -1 & 0 \end{bmatrix} \boldsymbol{b}$$

holds.

[2] The last step of the developement hinges on the relationship for 2×2 matrices:

$$J^{-1} = \frac{1}{\det J} \begin{bmatrix} J_{22} & -J_{12} \\ -J_{21} & J_{11} \end{bmatrix}.$$

Substitution of (5.47) back to (5.42) yields

$$\int_{\Omega} \mu_{\beta}^{-1} \star da \wedge da' \;=\; -\int_{\varphi_\beta(\Omega)} \frac{1}{\det J} \mu_{\beta}^{-1} \nabla a_{\beta}^{T} J J^{T} \nabla a'_{\beta}. \tag{5.48}$$

In order to compute the second integral of (5.41) in the computation chart, we need to represent the Hodge operator for 0-forms. For an arbitrary 0-form $\omega \in \mathcal{F}^0(\Omega)$, the Hodge operator satisfies [14]

$$\star\omega = \omega \, \mathrm{vol}_n \;=\; \omega \sqrt{|\det G^{\beta}|}\, dx_{\beta}^{1} \wedge ... \wedge dx_{\beta}^{n}, \tag{5.49}$$

where vol_n is called the *volume n-form*. Then, substitution of (5.16) to (5.49), yields

$$\star\omega \;=\; \omega \frac{1}{|\det J|}\, dx_{\beta}^{1} \wedge ... \wedge dx_{\beta}^{n}. \tag{5.50}$$

The contraction in (5.41) can be expanded in the chart (U_β, φ_β) as

$$i_V da \;=\; da(v) = \sum_{k=1}^{2} \frac{\partial a}{\partial x_k^{\beta}} dx_{\beta}^{k} \left(\sum_{i=1}^{2} v_{\beta}^{i} \partial_i^{\beta} \right) = \sum_{k=1}^{2} \frac{\partial a}{\partial x_k^{\beta}} v_{\beta}^{k} = \boldsymbol{v}_{\beta}^{T} \nabla a_{\beta}. \tag{5.51}$$

Thus, application of (5.49) and (5.51) to the second integral of (5.41), yields

$$\begin{aligned} \int_{\Omega_c} \sigma_\beta \star \left(\frac{\partial}{\partial t} a + i_V da \right) \wedge a' \;&=\; \int_{\varphi_\beta(\Omega_c)} \sigma_\beta \left(\frac{\partial a_\beta}{\partial t} + \boldsymbol{v}_{\beta}^{T} \nabla a_{\beta} \right) a'_{\beta} \mathrm{vol}(\partial_1^{\beta}, \partial_2^{\beta}) \\ &=\; \int_{\varphi_\beta(\Omega_c)} \frac{1}{|\det J|} \sigma_\beta \left(\frac{\partial a_\beta}{\partial t} + \boldsymbol{v}_{\beta}^{T} \nabla a_{\beta} \right) a'_{\beta}. \end{aligned} \tag{5.52}$$

In order to compute the third integral of (5.41), let us express the source current 2-form in two charts

$$j^s \;=\; \mathcal{J}_{\beta}^{s} dx_{\beta}^{1} \wedge dx_{\beta}^{2} = \mathcal{J}_{e}^{s} dx_{e}^{1} \wedge dx_{e}^{2} \tag{5.53}$$

Substitution of the basis vectors $(\partial_1^{\beta}, \partial_2^{\beta})$ of the tangent space for the chart (U_β, φ_β) and application of the coordinate transformation (5.9), yield

$$\mathcal{J}_{\beta}^{s} \;=\; \frac{1}{|\det J|} \mathcal{J}_{e}^{s}. \tag{5.54}$$

Let us define $j_{\beta}^{s} := \varphi_{\beta}^{-1*} j_s$. Then, the third integral of (5.41) can be expanded

$$\begin{aligned} \int_{\Omega_s} j^s \wedge a' \;&=\; \int_{\varphi_\beta(\Omega_s)} j_{\beta}^{s} (\partial_1^{\beta}, \partial_2^{\beta}) a'_{\beta} \\ &=\; \int_{\varphi_\beta(\Omega_s)} \mathcal{J}_{\beta}^{s} a'_{\beta} \\ &=\; \int_{\varphi_\beta(\Omega_s)} \frac{1}{|\det J|} \mathcal{J}_{e}^{s} a'_{\beta}. \end{aligned} \tag{5.55}$$

Combination of (5.48), (5.52), (5.55) and (5.41), yields the weak formulation in coordinates: Find $a \in \mathcal{F}_0^0(\varphi_\beta(\Omega))$ so that

$$-\int_{\varphi_\beta(\Omega)} \frac{1}{|\det J|}\mu_\beta^{-1}\nabla a_\beta^T J J^T \nabla a'_\beta \;+\; \int_{\varphi_\beta(\Omega_c)} \frac{1}{|\det J|}\sigma_\beta \left(\frac{\partial a_\beta}{\partial t} + \boldsymbol{v}_\beta^T \nabla a_\beta\right) a'_\beta \tag{5.56}$$
$$+\; \int_{\varphi_\beta(\Omega_s)} \frac{1}{|\det J|}\mathcal{J}_e^s a'_\beta = 0$$

holds for all $a' \in \mathcal{F}_0^0(\varphi_\beta(\Omega))$.

5.3.3 Movement and charts

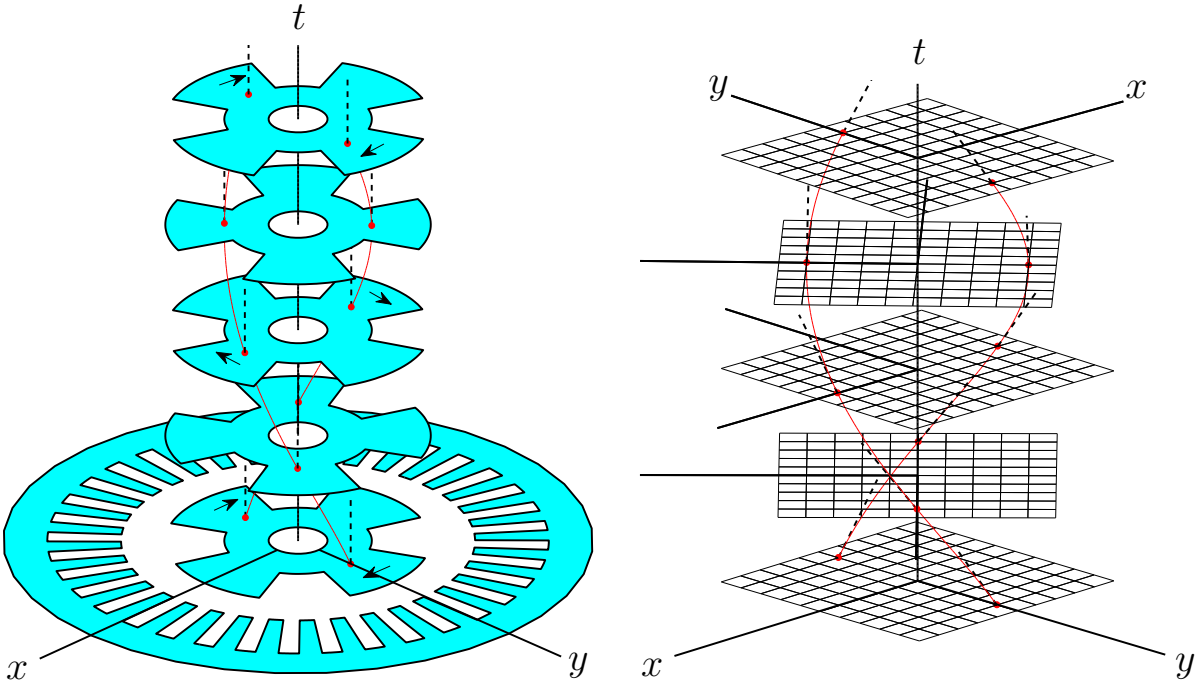

(a) Fixed chart **(b)** Co-rotating chart

Figure 5.3: Material derivative of a scalar field is the time-derivative along the curves determined by the placement mapping X_t (red curves). Time derivative at the intersection points in a given chart is equal to the time-derivative along the fixed-coordinate lines (approximated by dashed black lines).

The weak formulation in coordinates (5.56) is written in a fixed chart. Then, time-derivative of the magnetic stream function at given coordinates is equal to the time-derivate at the corresponding point of E^2 (see Figure 5.3a). However, when the coordinate chart is time-dependent, the time-derivatives at specific coordinates are also influenced by the time-evolution of the chart with respect to E^2 and are not equal to the corresponding points of E^2.

Let us define the representation of the one-parameter family of transformations X_t in terms of the chart (U_β, φ_β)

$$\boldsymbol{x}_t^\beta \;:=\; (\varphi_\beta \circ X_t \circ \varphi_\beta^{-1}) : \varphi_\beta(U_\beta) \times \mathbb{R} \to \mathbb{R}^2. \tag{5.57}$$

Then, by application of the chain rule,

$$\begin{aligned} \frac{\partial}{\partial t}(a_\beta \circ \boldsymbol{x}_t^\beta) &= \frac{\partial a_\beta}{\partial t} \circ \boldsymbol{x}_t^\beta + \nabla a_\beta^T \frac{\partial \boldsymbol{x}_t^\beta}{\partial t} \\ &= \frac{\partial a_\beta}{\partial t} \circ \boldsymbol{x}_t^\beta + \boldsymbol{v}_\beta^T \nabla a_\beta \end{aligned} \tag{5.58}$$

holds. Thus, when the computation chart is chosen to co-move with the conductive material, the convective term $\boldsymbol{v}_\beta^T \nabla a_\beta$ in (5.56) is zero (see Figure 5.3b). The time-derivative of the composite function in (5.58) is known in continuum mechanics as the *material derivative* of a_β.

5.3.4 Discretization

The problem is discretized with Finite Elements in the computational chart $(U_\beta, \varphi_\beta^t)$, which is chosen fixed to conductive materials. Let us denote by Ψ_n the standard nodal basis functions corresponding to the finite element discretization of the region $\varphi_\beta^t(\Omega)$. Then a_β can be approximated by the expansion

$$a_\beta^t := \sum_{n=1}^{N} a_n \Psi_n, \tag{5.59}$$

where N is the number of nodes in the mesh for Ω. Application of the Galerkin procedure to (5.56) yields the system of equations

$$\left[M\right] \frac{\partial \boldsymbol{a}}{\partial t} + \left[S\right] \boldsymbol{a} = \boldsymbol{f}, \tag{5.60}$$

where $S \in \mathbb{R}^{N \times N}$ is the full stiffness matrix, $M \in \mathbb{R}^{N \times N}$ is the full mass matrix and $\boldsymbol{f} \in \mathbb{R}^N$ the full excitation vector.

That is, we define

$$S_{mn} := \int_{\varphi_\beta^t(\Omega)} \frac{1}{|\det J|} \mu_\beta^{-1} \nabla \Psi_m^T J J^T \nabla \Psi_n, \tag{5.61}$$

$$M_{mn} := -\int_{\varphi_\beta^t(\Omega_c)} \frac{1}{|\det J|} \sigma_\beta \Psi_m \Psi_n, \tag{5.62}$$

$$f_m := \int_{\varphi_\beta^t(\Omega_s)} \frac{1}{|\det J|} \mathcal{J}_e^s \Psi_m. \tag{5.63}$$

Movement can be incorporated into a FE model by introduction of modified material relations such that the stiffness and mass matrices are equal to (5.61) – (5.63). Thus, support for movement can be implemented into any FE software that supports time-dependent anisotropic material parameters.

In such implementations, movement introduces time-dependence into the material parameters. The parts of the matrices corresponding to the nodes in the regions with

updated material parameters need to be reconstructed between time steps. However, no changes to the mesh in the computation chart are required.

Fixed coordinate transformations can be easily incorporated into the approach by appropriate selection of the computational chart φ_β. As discussed in the introduction, such transformations might feasible, for example when dealing with open boundaries or different length scales. The transformations only affect the Jacobians used in the evaluation of (5.61) – (5.63) and can be incorporated into the material parameters and source currents.

5.4 Examples

In this section, we derive the placement mappings and the corresponding Jacobians for the test cases of publications 1 and 3:

- In publication 1, the presented approach is used to implement movement of the armature in a FE model for a simple valve by introduction of anisotropic time-dependent reluctivity to the air gap.

- In publication 3, the presented approach is coupled to a lock step method [26] to implement rotation in a FE model for an induction machine. Small rotations between lock steps are implemented by introduction of anisotropic time-dependent reluctivity in the air gap. Since rotation angles are not limited to multiples of the element size in the air gap, the allowed time step size is decoupled from the meshing of the air gap.

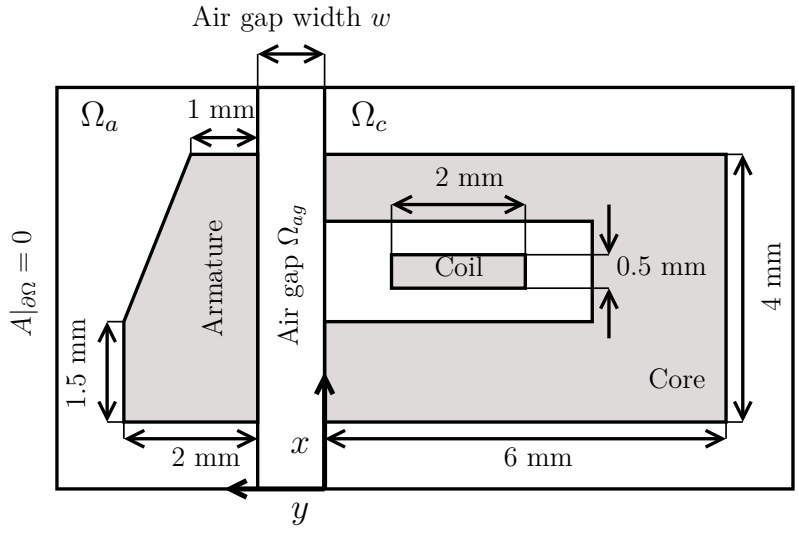

Figure 5.4: Geometry of a valve.

5.4.1 Linear movement (Publication 1)

Consider the cross-sectional geometry of the valve shown in Figure 5.4. The problem domain Ω is partitioned into armature, air gap and core regions denoted by Ω_a, Ω_{ag} and Ω_c, respectively. For simplicity, translational symmetry with respect to the z-axis and mirror symmetry with respect to the y-axis are assumed whereas in publication 1, the geometry is assumed to be axisymmetric.

Let (Ω, φ_e) be the global coordinate chart in terms of Cartesian coordinates suggested in Figure 5.4. We denote the actual width of the air gap and the air gap width in the chart (Ω, φ_e) by w and w_0, respectively. Then, the representation $\boldsymbol{x}_t^e$ of the placement map X_t can be written

$$\boldsymbol{x}_t^e : \varphi_e(\Omega) \times \mathbb{R} \to E^2 : \begin{bmatrix} x_1 \\ y_1 \end{bmatrix} \mapsto \begin{bmatrix} x_2 \\ y_2 \end{bmatrix} = \begin{cases} (x_1, y_1), & y_1 < 0 \\ (x_1, y_1 w(t)/w_0), & w_0 \geq y_1 \geq 0 \\ (x_1, y_1 + w(t)), & y_1 > w_0 \end{cases} . \quad (5.64)$$

The Jacobian of the placement map (5.64) can be expanded in the air gap Ω_{ag} as

$$J_t = \begin{bmatrix} 1 & 0 \\ 0 & w(t)/w_0 \end{bmatrix} \quad (5.65)$$

with the determinant $\det J_t = w(t)/w_0$. Outside the air gap, the Jacobian J_t is equal to the identity matrix.

Thus, the relative movement of the armature with respect to the core influences only the stiffness matrix (5.61) in the air gap whereas outside the air gap the Jacobian J_t is equal to the identity matrix and (5.61) – (5.63) simplify to their usual form.

5.4.2 Rotational movement (Publication 3)

Let us partition the problem domain into the rotor, stator and air gap regions Ω_r, Ω_s and Ω_{ag}, respectively, so that the interfaces between the regions are concentric circles. The radii of the airgap interfaces for the rotor and stator are denoted by R_r and R_s, respectively. Let (Ω, φ_e) be a global coordinate chart in terms of Cartesian coordinates.

In order to construct the representation $\boldsymbol{x}_t^e$ of the placement mapping X_t in the Cartesian chart, we first use the polar coordinates to define rotation angles for each subregion. Then, the placement mapping in terms of polar coordinates is transformed into the Cartesian chart (Ω, φ_e).

Let $\Delta\theta$ be the mechanical rotation of the rotor with respect to the stator. Within the air gap region Ω_{ag}, the rotation is selected as in Publication 3. That is, we define

$$\begin{aligned} \boldsymbol{\Theta}_t &: (\mathbb{R} \times [0, 2\pi)) \times \mathbb{R} \to \mathbb{R}^2 \quad (5.66) \\ &: \begin{bmatrix} r_1 \\ \theta_1 \end{bmatrix} \mapsto \begin{bmatrix} r_2 \\ \theta_2 \end{bmatrix} = \begin{cases} (r, \theta), & r > R_s \\ (r, \theta + \Delta\theta(t)), & r < R_r \\ \left(r, \theta + \Delta\theta(t) \dfrac{\ln R_s - \ln r}{\ln R_s - \ln R_r}\right), & R_r < r < R_s \end{cases} . \end{aligned}$$

The change of coordinates map from polar to Cartesian coordinates is defined

$$\boldsymbol{\psi}_{cp} : \mathbb{R} \times [0, 2\pi) \to \mathbb{R}^2 \quad : \quad \begin{bmatrix} r_2 \\ \theta_2 \end{bmatrix} \mapsto \begin{bmatrix} x_2 \\ y_2 \end{bmatrix} = \begin{bmatrix} r_2 \cos\theta_2 \\ r_2 \sin\theta_2 \end{bmatrix} \tag{5.67}$$

with the inverse mapping

$$\boldsymbol{\psi}_{cp}^{-1} : \mathbb{R}^2 \to \mathbb{R} \times [0, 2\pi) \quad : \quad \begin{bmatrix} x_1 \\ y_1 \end{bmatrix} \mapsto \begin{bmatrix} r_1 \\ \theta_1 \end{bmatrix} = \begin{bmatrix} \sqrt{x_1^2 + y_1^2} \\ \operatorname{atan2}(x_1, y_1) \end{bmatrix}. \tag{5.68}$$

Then, the placement map in terms of the Cartesian chart (Ω, φ_e) can be written as (see Figure 5.5)

$$\boldsymbol{x}_t^e : \varphi_e(\Omega) \times \mathbb{R} \to \varphi_e(\Omega) \quad : \quad \boldsymbol{x}_t^e := \boldsymbol{\psi}_{cp} \circ \boldsymbol{\Theta}_t \circ \boldsymbol{\psi}_{cp}^{-1}. \tag{5.69}$$

Within the air gap region Ω_{ag}, the Jacobian of the placement map can be computed with the chain rule

$$\begin{aligned} J_t &= \begin{bmatrix} \dfrac{\partial x_2}{\partial r_2} & \dfrac{\partial x_2}{\partial \theta_2} \\ \dfrac{\partial y_2}{\partial r_2} & \dfrac{\partial y_2}{\partial \theta_2} \end{bmatrix} \begin{bmatrix} \dfrac{\partial r_2}{\partial r_1} & \dfrac{\partial r_2}{\partial \theta_1} \\ \dfrac{\partial \theta_2}{\partial r_1} & \dfrac{\partial \theta_2}{\partial \theta_1} \end{bmatrix} \begin{bmatrix} \dfrac{\partial r_1}{\partial x_1} & \dfrac{\partial r_1}{\partial y_1} \\ \dfrac{\partial \theta_1}{\partial x_1} & \dfrac{\partial \theta_1}{\partial y_1} \end{bmatrix} \\ &= \begin{bmatrix} \cos\theta_2 & -r_2 \sin\theta_2 \\ \sin\theta_2 & r_2 \cos\theta_2 \end{bmatrix} \begin{bmatrix} 1 & 0 \\ -\dfrac{\Delta\theta(t)}{r_1(\ln R_s - \ln R_r)} & 1 \end{bmatrix} \begin{bmatrix} x_1/r_1 & y_1/r_1 \\ -y_1/r_1^2 & x_1/r_1^2 \end{bmatrix}. \end{aligned} \tag{5.70}$$

Since $r_2 = r_1$ holds, the Jacobian in the air gap region satisfies

$$\det J_t = r_2(\cos^2\theta_2 + \cos^2\theta_1) \cdot 1 \cdot \frac{r_1^2}{r_1^3} = \frac{r_2}{r_1} = 1. \tag{5.71}$$

Within the rotor and stator regions J_t is equal to the identity matrix.

Thus, the relative movement of the rotor with respect to the stator influences only the stiffness matrix (5.61) in the air gap.

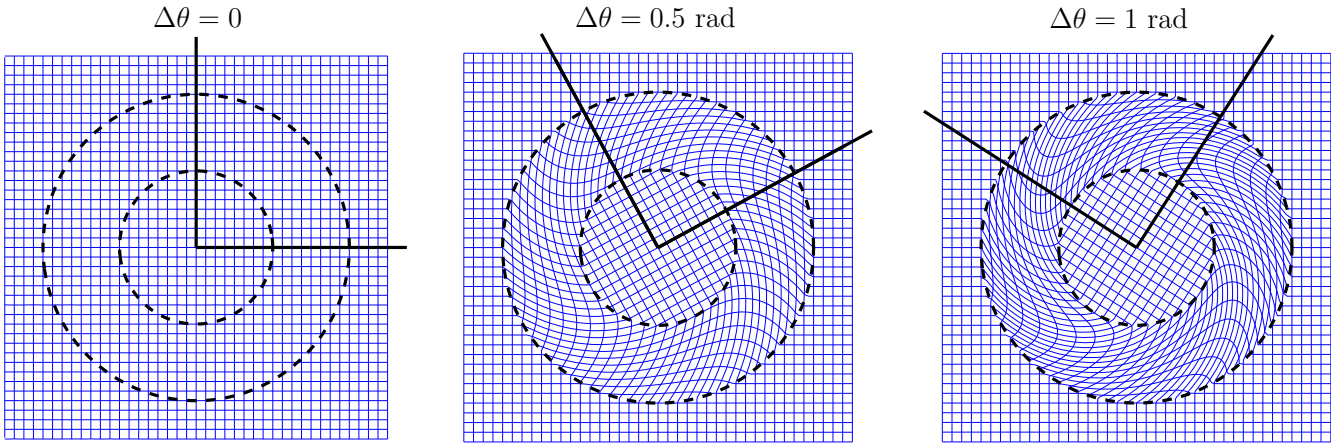

Figure 5.5: Placement map (5.69) for three different rotation angles $\Delta\theta$.

Chapter 6

Conclusion

> For a successful technology, reality must take precedence over public relations, for nature cannot be fooled.
>
> — R. Feynman, Report of the Presidential Commission on the Space Shuttle Challenger Accident, 1986

The main objective of this study was to develop efficient and accurate methods for electromagnetic analysis of rotating electrical machines. Several efficient solution methods based on the numerical or analytical solution of spectral Dirichlet-to-Neumann mappings were discussed in chapters 2-4 and publications 2 and 4. In the publications, the developed methods were applied to realistic test cases and the solutions were confirmed with full time-domain FE solution. The mappings were also applied to study and predict the non-zero air gap field harmonics.

The second approach discussed in this study was to model movement in electromechanical devices by change in the coordinate representation of the metric tensor in the air gap. This allowed modeling of movement in a time-parametrized family of coordinate systems fixed to the moving materials. In FE implementations, coordinates of the mesh nodes are fixed and movement can be incorporated into the material parameters in the air gap.

6.1 Air gap field harmonics

Fourier series expansion of the Dirichlet and Neumann data provides an excellent window into various electromagnetic phenomena in rotating electrical machines. Electromagnetics of each subproblem is completely charaterized for the remaining subproblem by the relation between Dirichlet data, Neumann data and the winding currents within the subproblem (Section 3.3). Moreover, power flow between subproblems can be efficiently accounted for in terms of Dirichlet and Neumann coefficients (Section 3.4).

To facilitate numerical computation, the series expansions of the Dirichlet and Neumann data were truncated to a finite set of harmonics. The truncation leads to error also in the solved Dirichlet and Neumann coefficients. A method for obtaining upper

limits for this error would be useful in the selection of the harmonics included in the model (O.Q. 3.1 at p. 19).

In time-domain, spectral Dirichlet-to-Neumann maps can be easily constructed only for subproblems with linear material parameters and eddy-currents limited to the windings (Section 3.3). The current density on each cross-sectional winding region was assumed to be uniform. Generalization of the time-domain approach to induction currents with significant skin effect would make the approach applicable to massive conductors such as the rotor bars in squirrel-cage rotors (O.Q. 3.2 at p. 19). In frequency-domain, eddy-currents not limited to the windings can be taken into account (Section 4.3). However, circuit coupling and windings in the rotor subproblem were not discussed in the chapter 4. In frequency-domain, coupling of massive conductors, such as rotor bars in squirrel-cage rotors to external circuits could be achieved with $A - \phi$ formulation of the rotor subproblem [6].

The assumption of linear material parameters in the reformulated subproblems is the main limitation of the discussed method. However, as discussed in the introduction, our aim has been to develop more efficient methods by making a trade-off between efficiency and generality. Moreover, if saturation can be neglected in only one subproblem, a non-linear FE model for the remaining subproblem can be coupled with the reformulated subproblem.For example, in the first test case of publication 4, a non-linear FE model of the rotor was coupled with a reformulated stator subproblem. However, such a model is not accurate when significant saturation exists in the stator. Saturation in the stator can become significant especially under transient conditions such as during starting of an induction motor.

Generalization to subproblems with significant saturation by linearization might be feasible when the permeability distribution can be approximated to be independent of time. In more general situations, reconstruction of the linearized spectral Dirichlet-to-Neumann map between time steps as the saturation state changes with time would make the approach unfeasible in terms of solution time compared to standard FE solution (O.Q. 3.3 at p. 20)

In publication 4, application of spectral Dirichlet-to-Neumann mappings were demonstrated to lead to a significant decrease in the solution time of time-domain BVPs with linear material relations in at least one of the subproblems. However, construction of the matrices for the spectral Dirichlet-to-Neumann mappings can require a significant amount of time and memory, especially when both subproblems are to be reformulated. Reduction of the problem geometry by symmetry conditions could be used to reduce the required solution time: In the section 3.6, the solution to BVPs (3.23) – (3.25) and (3.127) – (3.129) with linear material relations were shown to satisfy rotational symmetry with respect to rotations of a single slot. This suggests that it might be possible to reduce the problem region used in the construction of the matrices to a single slot (O.Q. 3.5 at p. 34).

In chapter 4, spectral Dirichlet-to-Neumann mappings were discussed in the context of frequency-domain problems. To model problems in steady-state, the Dirichlet and Neumann data was expanded in the stator coordinate system as a Fourier series of two

variables: time t and mechanical angle θ_s. In section 4.3, the spectral Dirichlet-to-Neumann mappings were derived for both subproblems in the stator coordinate system. In order to construct the mapping for the rotor subproblem in the stator coordinate system, we derived the generalized slip transformations, which describe how the time-frequencies in the Dirichlet and Neumann data transform between the rotor and stator coordinate systems. It was also shown that a slotted rotor rotating at a non-integer slip can lead to time-frequencies in the Neumann data, which are not integer-multiples of the synchronous frequency. However, for arbitrary rational-valued rotor slip, a fundamental frequency ω_f can be selected so that all time-frequencies in the Dirichlet and Neumann data are always integer-multiples of the selected fundamental frequency ω_f.

The approach discussed in the chapter 4 could be also formulated using spectral Dirichlet-to-Neumann mapping for both subproblems in their own coordinate systems. Such an approach would lead to simpler matrices for the Dirichlet-to-Neumann mappings and the slip transformations induced by interface conditions $(4.6) - (4.7)$ would play a similar role to the rotation matrices in time-domain (O.Q. 4.1 at p. 45).

As in time-domain, rotational symmetries were shown to yield sparsity patterns for the matrices of the spectral Dirichlet-to-Neumann mappings. In section 4.4, we discussed how the sparsity patterns could be used to predict the non-zero time and space harmonics in the Dirichlet and Neumann data without any assumptions about the shape or material parameters of the slots. However, when the rotor is eccentric, the variation introduced to the air gap permeance leads to additional harmonics in the Dirichlet and Neumann data. Then, the symmetry arguments developed in sections 4.4 and 3.6 do not hold and the matrices for the spectral Dirichlet-to-Neumann maps become more dense (O.Q. 4.2 at p. 49). Even though problems with saturation cannot be easily reformulated with spectral Dirichlet-to-Neumann mappings, it might be possible to predict the additional harmonics introduced by saturation to the air gap (O.Q. 4.3 at p. 50).

Spectral Dirichlet-to-Neumann mappings can be used as a basis for efficient numerical methods also in frequency-domain. An example of such a method was indirectly discussed in the publication 2, where Dirichlet-to-Neumann mapping for the rotor subproblem was solved analytically and coupled to a finite element model of the stator.

6.2 Metric and motion

Differential forms on Riemannian manifolds allow coordinate-independent formulation of BVPs arising from electromagnetics of electromechanical devices. In section 5.1, we discussed how any Euclidean space can be viewed as a Riemannian manifold. In Euclidian space, a time-parametrized family of coordinate charts can be selected so that the coordinates associated to material points remain fixed. Then, the movement corresponds to change in the coordinate representation of the metric tensor of the manifold.

In section 5.2, we briefly discussed the formulation of magnetoquasistatics in two and three-dimensional Euclidean spaces with differential forms. Since an Eulerian model of space and movement was used, the common form of Ohm's law was replaced with the generalized Ohm's law for moving bodies. A two-dimensional BVP in terms of the mag-

netic stream function was derived by application of an approximation of translational symmetry. In the derived BVP and the corresponding weak formulation discussed in section 5.3, the Ohm's law for moving bodies corresponds to a material derivative of the magnetic stream function.

In any time-parametrized family of coordinate charts co-moving with the material bodies, the material derivatives of the weak formulation simplify to time-derivatives and the corresponding FE formulation simplifies to its usual form within the moving bodies. The influence of movement to the metric tensor in the air gap can be incorporated into the material relations. This yields a simple approach for dealing with movement in FE models for electromechanical devices without any changes in the mesh between time steps.

The approach was successfully applied to realistic test cases involving linear and rotating motion in publications 1 and 3, respectively. The corresponding coordinate transformations and Jacobians for the test cases were discussed in the section 5.4.

In publication 1, we discussed how the presented FE formulation with fixed mesh is equivalent to FE formulations in Cartesian charts with deforming mesh. Thus, the difficulties of standard methods with deforming mesh apply also to the presented method. The fixed mesh of the computational chart should be built so that its representation stays acceptable in Cartesian charts. For the mappings derived in section 5.5 for rotating motion, large rotations correspond to a highly deformed mesh in the air gap. As the rotation grows large enough, the basis functions corresponding to the deformed elements become unable to represent the fields in the air gap. In publication 3, we presented a method, which combines metric-based rotations with the lock-step approach. Small rotations between lock steps are taken into account by change in the coordinate representation of the metric. The deformation was quantified with the condition number of the equivalent permeability in the air gap. When the deformation grows large enough, the air gap needs to be remeshed. Since the rotation angle is not limited by the meshing of the air gap, time step size can be chosen freely.

Bibliography

[1] H. Pihala, S. Hänninen, Sähkönsäästöpotentiaali energiatehokkailla sähkömoottorikäytöillä Suomen energiavaltaisessa teollisuudessa, VTT, Research Report, 2008.

[2] J. Kirtley, Electric Power Principles: Source, Conversion, Distribution and Use, Wiley, 2010.

[3] A. Fitzgerald, C. Kingsley, S. Umans, Electric Machinery, McGraw-Hill, 2002.

[4] B. Heller, V. Hamata, Harmonic Field Effects in Induction Machines, Elsevier, 1977.

[5] K. Oberretl, "Losses, torques and magnetic noise in induction motors with static converter supply, taking multiple armature reaction and slot openings into account.", *Electric Power Applications*, IET 1.4 (2007), pp. 517-531.

[6] A. Arkkio. Analysis of Induction Motors Based on the Numerical Solution of the Magnetic Field and Circuit Equations. ACTA POLYTECHNICA SCANDINAVICA, PhD thesis, 1987.

[7] K. Hameyer, R. Belmans, Numerical Modelling and Design of Electrical Machines and Devices, WITpress, Southampton: WIT Press, 1998.

[8] A. Nicolet, J.-F. Remacle, B. Meys, A. Genon, W. Legros, "Transformation methods in computational electromagnetism", *Journal of Applied Physics*, vol. 75, pp. 6036-6038, 1994.

[9] J.-F. Remacle, A. Nicolet, A. Genon, W. Legros, "Comparison of boundary elements and transformed finite elements for open magnetic problems", Boundary Elements XVI, Computational Mechanics Publications, July 1994, pp. 109-116.

[10] A. Ward, J. Pendry, "Refraction and geometry in Maxwell's equations", Journal of Modern Optics, vol. 43, pp. 773-793, 1996.

[11] "On cloaking for elasticity and physical equations with a transformation invariant form", New Journal of Physics, vol. 8, 2006.

[12] A. Nicolet, F. Zolla, S. Guenneau, "Modelling of twisted optical waveguides with edge elements", European Physical Journal, vol. 28, pp. 153-157, 2004.

[13] A. Stenvall, T. Tarhasaari, F. Grilli, P. Raumonen, M. Vojenciak, M. Pellikka, "Manifolds in electromagnetism and superconductor modelling: using their properties to model critical current of twisted conductors in self-field with 2-D model", Cryogenics, vol. 53, pp. 135-141, 2013.

[14] P. Raumonen, Mathematical Structures for Dimensional Reduction and Equivalence Classification of Electromagnetic Boundary Value Problems, PhD thesis, Tampere University of Technology, 2009.

[15] T. Frankel, The Geometry of Physics, 2nd ed., Cambridge University Press, 2001.

[16] M. Shah and S. Lee, "Rapid Analytical Optimization of Eddy Current Shield Thickness for Associated Loss Minimization in Electrical Machines", *IEEE Transactions on Industry Applications*, vol. 42, no. 3, pp. 642-649, 2006.

[17] E. Freeman, "Travelling waves in induction machines: input impedance and equivalent circuits", *Proceedings of the IEEE*, vol. 115, no. 12, 1968.

[18] J. Gieras, "Analysis of multilayer rotor induction motor with higher space harmonics taken into account", *IEE Proceedings B: Electric Power Applications*, vol. 138, no. 2, pp. 59-67, 1991.

[19] H. De Gersem , T. Weiland, "A computationally efficient air-gap element for 2D FE machine models", *IEEE Transactions on Magnetics*, vol. 41, no. 5, pp. 1844-1847, 2005.

[20] P. Raumonen, S. Suuriniemi, T. Tarhasaari, L. Kettunen, "Manifold and Metric in Numerical Solution of the Quasistatic Electromagnetic Boundary Value Problem", arXiv:0710.1747v1, 2007.

[21] N. Mohan, Advanced Electric Drives, Minneapolis, MN:MNPERE, 2001.

[22] S. Kurz, S. Suuriniemi, "A space-time view on low-frequency electrodynamics", ACE'10 - Advanced Computational Electromagnetics, July 5-7 2010, Zürich, Switzerland.

[23] J. Van Bladel, Relativity and Engineering, Springer, 1984.

[24] L. Qaseer, S. Purushothaman, F. Leon, "Closed-Form Analysis of Squirrel-Cage Induction Motors With Anisotropic Modeling of Stator and Rotor", *IEEE Transactions on Magnetics*, vol. 27, no. 3, pp. 553-560, 2012.

[25] J. Flaherty, Finite Element Analysis, Course Notes, Rensselaer Polytechnic Institute, 2000.

[26] B. Davat, Z. Ren, M. Lajoie-Mazenc, "The Movement in Field Modeling", *IEEE Transactions on Magnetics*, vol. 21, no. 6, pp. 2296-2298, 1985.

[27] I. Tsukerman, "Accurate Computation of 'Ripple Solutions' on Moving Finite Element Meshes", *IEEE Transactions on Magnetics*, vol. 31, no. 3, pp. 1472-1475, May. 1995.

[28] H. De Gersem, M. Ion., M. Wilke, T. Weiland, A. Demenko, "Trigonometric interpolation at sliding surfaces and in moving bands of electrical machine models", *COMPEL*, vol. 25, no. 1, pp. 31-42, 2006.

[29] H. De Gersem, "Combined Spectral-Element, Finite-Element Discretization for Magnetic-Brake Simulation", *IEEE Transactions on Magnetics*, vol. 46, no. 8, Aug. 2010.

[30] J. Pyrhönen, T. Jokinen, V.Hrabovcova. Design of Rotating Electrical Machines. Wiley, 2008.

[31] W. Gibbs, Conformal Transformations in Electrical Engineering, Chapman & Hall, London, 1958.

[32] D. Givoli, "Recent advances in the DtN FE Method", *Archives of Computational Methods Engineering* vol. 6, no. 2, pp. 71-116, 1999.

[33] A. Quarteroni, A. Valli, Domain Decomposition Methods for Partial Differential Equations, Oxford University Press, 1999.

[34] A. Abdel-Razek, J. Coulomb, M. Feliachi, J. Sabonnadiere, "Conception of an Air-Gap Element for the Dynamic Analysis of the Electromagnetic Field in Electric Machines", *IEEE Transactions on Magnetics*, vol. 18, no. 2, Mar. 1982.

[35] K. Lee, M. DeBortoli, M. Lee, S. Salon, "Coupling Finite Elements and Analytical Solution in the Airgap of Electrical Machines", *IEEE Transactions on Magnetics*, vol.27, no. 5, Sep. 1991.

[36] E. Vassent, G. Meunier and A. Foggia, "Simulation of Induction Machines Using Complex Magnetodynamic Finite Element Method Coupled With the Circuit Equations", *IEEE Transactions on Magnetics*, vol. 27, no. 5, pp. 4246-4248, 1991.

[37] J. Gyselinck, L. Vandevelde, P. Dular, C. Geuzaine, W. Legros, "A General Method for the Frequency Domain FE Modeling of Rotating Electromagnetic Devices", *IEEE Transaction on Magnetics*, vol. 39, no. 3, pp. 1147-1150, 2003.

[38] A. Naylor, G. Sell, Linear Operator Theory in Engineering and Science, Springer, 2nd ed., 1982.

[39] J. Jackson, Classical Electrodynamics, Wiley, 1975.

[40] R. Mertens, U. Pahner, K. Hameyer, R. Belmans, "Force Calculation Based on a Local Solution of Laplace's Equation". *IEEE Transactions on Magnetics*, vol. 33, no. 2, pp. 1216-1218, Mar. 1997

[41] D. Dorrell, W. Thomson, S. Roach, "Analysis of Airgap Flux, Current, and Vibration Signals as a Function of the Combination of Static and Dynamic Airgap Eccentricity in 3-Phase Induction Motors", *IEEE Transactions on Industry Applications*, vol. 33, no. 1, pp. 24-34, 1997.

[42] P. Clayton, S. Nasar, Introduction to Electromagnetic Fields, 2nd ed., McGraw-Hill, 1987.

[43] K. Oberretl, "Field-harmonic theory of slip-ring motor taking multiple armature reaction into account", *Proceedings of the IEEE*, vol. 117, no. 8, pp. 1667-1674, 1970.

[44] A. Bossavit, "Differential forms and the computation of fields and forces in Electromagnetism", *European Journal of Mechanics, B/Fluids*, vol. 10, no. 5, pp. 474-88, 1991.

[45] K. Jänich, Vector Analysis, Springer, 2001.

[46] M. Le Bellac, J.-M. Lévy-Leblond, "Galilean Electromagnetism", *Il Nuovo Cimento*, vol. 14b, no. 2, 1973.

[47] H. Woodson, J. Melcher, Electromechanical Dynamics, pt.1, Wiley, 1968.

[48] S. Kurz "A novel formulation for 3D eddy current problems with moving bodies using a Lagrangian description and BEM-FEM coupling", *IEEE Transactions on Magnetics*, vol. 34, no.5, pp. 3068-3073, Sep. 1998.

[49] M. Jagiela and T. Garbiec. "Evaluation of Rotor-End Factors in Solid-Rotor Induction Motors", *IEEE Transactions on Magnetics*, vol. 48, no. 1, pp. 137-142, 2012.

Tampereen teknillinen yliopisto
PL 527
33101 Tampere

Tampere University of Technology
P.O.B. 527
FI-33101 Tampere, Finland

ISBN 978-952-15-3455-3
ISSN 1459-2045